Searching For Neutral Kaon Rare Decay
$K_L \to \pi^0 \nu \bar{\nu}$

by

Jia Xu

A dissertation submitted in partial fulfillment
of the requirements for the degree of
Doctor of Philosophy
(Physics)
in The University of Michigan
2015

Doctoral Committee:

Professor Myron K. Campbell, Chair
Assistant Professor Brian K. Arbic
Associate Professor Henriette Elvang
Assistant Professor Thomas A. Schwarz
Professor Bing Zhou

ACKNOWLEDGEMENTS

TABLE OF CONTENTS

LIST OF FIGURES

LIST OF TABLES

LIST OF APPENDICES

Appendix

ABSTRACT

Searching For Neutral Kaon Rare Decay $K_L \to \pi^0 \nu \bar{\nu}$

by

Jia Xu

Chair: Myron Campbell

The KOTO E14 experiment is dedicated to searching for CP violating K_L^0 rare decay $K_L^0 \to \pi^0 \nu \bar{\nu}$. Events having 2 photons from π^0 decay with large transverse momentum and no other veto signals are selected. A signal box in the P_t - z plane is determined as signal region. Physics data taking of 100 hours during 2013 May accumulated 1.43×10^{18} protons on target . Single event sensitivity is $(1.29 \pm 0.06_{stat} \pm 0.19_{sys}) \times 10^{-8}$. Blind analysis is used to minimize cut bias. Expected number of background event is 0.36 ± 0.16 and after opening the box, 1 event is observed. The corresponding upper limit branching ratio is 5.03×10^{-8} at 90% confidence level.

CHAPTER I

The Theoretical Aspects of $K_L \to \pi^0 \nu \bar{\nu}$

1.1 Introduction

The long-lived neutral kaon K_L^0 has a CP violating decay channel $K_L^0 \to \pi^0 \nu \bar{\nu}$. In the Standard Model (SM) its branching ratio (the ratio of the decay rate through $K_L^0 \to \pi^0 \nu \bar{\nu}$ channel over the K_L^0 total decay rate) is calculated to be $(2.49 \pm 0.39 \pm 0.06) \times 10^{-11}$(*Brod et al.* (2011)). The theoretical uncertainties are very small, and therefore it is a clean channel in terms of branching ratio measurement. It has attracted particle physicists' interests in its ability to test the SM by giving accurate measurement of Cabibbo-Kobayashi-Maskawa (CKM) matrix element parameters. Also, as a flavor changing neutral current (FCNC) process, the mechanism behind this process is forbidden at tree level in the SM, and can only proceed through higher order Feynman diagrams. The rate is therefore very sensitive to short distance effects, i.e. high energy physics, which may be at the energy scale the current accelerator cannot reach. As a result, it is an excellent tool for probing the Beyond Standard Model (BSM) extensions which are at energy scale at TeV.

In this chapter, we will start with the brief description of kaon phenomenology by giving the basic terminology, focusing on its CP violating properties. Following that will be a discussion on how the branching ratio measurement of $K_L^0 \to \pi^0 \nu \bar{\nu}$ will be a good tool to test the SM. It will be followed by the prediction of the branching

ratio from different BSM extensions. This chapter concludes with a brief overview of previous experimental efforts.

1.2   Kaon Phenomenology

The most interesting phenomenon in K meson system is CP violation. There are three important discrete symmetries in quantum field theory: charge conjugation (C), i.e. convert the particle to its anti-particle; parity (P), by inverting the spatial coordinates and time reversal (T). The $SU(2)_L \times$ U(1) electroweak force is CP variant, meaning Lagrangian is not invariant under the combined action of charge conjugation and parity.

For example, let's consider K^0_L decays into π^0s. A neutral pion π^0 is a CP odd state, since it's a pseudoscalar with parity eigenvalue -1. A state of two π^0s, if the total angular momentum L is 0, has paritiy equals $(-1)^{2+L} = 1$. Let's also assume that the long-lived kaon K^0_L is a CP odd state, i.e. $CP|K^0_L\rangle = -|K^0_L\rangle$. If CP is conserved, the K^0_L cannot decay into $\pi^0\pi^0$ state via weak interaction. But in 1964, Brookhaven experiment observed $K^0_L \to 2\pi$ decay but at very low rate (*Christenson et al.* (1964)). Field theory assumes CPT to be a good symmetry. So for CP violation processes, the T reversal will not hold any more.

The K mesons, $\begin{pmatrix} K^- \\ K^0 \end{pmatrix}$ and its charge conjugation $\begin{pmatrix} K^+ \\ \bar{K}^0 \end{pmatrix}$ form strong isospin 1/2 doublets. For the neutral kaon system, the two strong eigenstates K^0 and $\bar{K}^0$ have quark constituents $(d\bar{s})$ and $(\bar{d}s)$ respectively. But neither K^0 nor $\bar{K}^0$ are weak eigenstates. Instead, they follow the relations

$$CP\left|K^0\right\rangle = -\left|\bar{K}^0\right\rangle \tag{1.1a}$$

$$CP\left|\bar{K}^0\right\rangle = -\left|K^0\right\rangle \tag{1.1b}$$

As a result, the CP eigenstates noted as K_1 and K_2 can be constructed via

$$|K_1\rangle = \left(|K^0\rangle + |\bar{K}^0\rangle\right)/\sqrt{2} \tag{1.2a}$$

$$|K_2\rangle = \left(|K^0\rangle - |\bar{K}^0\rangle\right)/\sqrt{2} \tag{1.2b}$$

Consequently, K_1 and K_2 will have CP eigenvalues -1 and $+1$, respectively. Life would be boring if the real life stable particles K_L^0 and K_S^0 (meaning long-lived kaon and short-lived kaon), which are mass eigenstates such that they don't oscillate, are the K_1 and K_2 with specific CP. In contrast, the mass eigenstates K_L^0 and K_S^0 are not exactly the CP eigenstates, but with a small mixing coefficient ϵ:

$$\left|K_S^0\right\rangle = \frac{\epsilon\left|K_1\right\rangle + \left|K_2\right\rangle}{\sqrt{1+\epsilon^2}} \tag{1.3a}$$

$$\left|K_L^0\right\rangle = \frac{\left|K_1\right\rangle + \epsilon\left|K_2\right\rangle}{\sqrt{1+\epsilon^2}} \tag{1.3b}$$

The absolute value of ϵ is 2.3×10^{-3}. This mechanism is called indirect CP violation. There is the other mechanism called direct CP coming from the weak interaction itself, and this effect is even smaller (denoted as ϵ'). Experimentally, the real part of $\epsilon'/\epsilon \approx 1.67 \times 10^{-3}$.

1.3 $K_L^0 \to \pi^0 \nu\bar{\nu}$ in the Standard Model

1.3.1 The "Golden" Flavor Changing Neutral Current Process

The flavor structure in the SM implies that in weak interactions, quarks with different flavors, i.e. from different families, cannot convert to each other without a change of charge. Such kind of process is called Flavor Changing Neutral Current (FCNC) process, where the neutral current is specific to Z^0 boson. A good example of FCNC vertex is $s \to dZ^0$, and this vertex describes processes like $K^0 \to l^+l^-$, where l can be e, μ, or τ; $K^+ \to \pi^+\nu\bar{\nu}$, and most of all, $K^0 \to \pi^0\nu\bar{\nu}$.

Because such FCNC processes are forbidden at tree level in the SM, they can only proceed through higher order loop diagrams with two $W^{\pm}$ interchanges which allows both the change of flavor and a conservation of charge. It's known that loop diagrams are suppressed by the small weak coupling constant, and thus such FCNC processes are generally rare processes happening at very low rate. If there is a new theory, which provides new diagrams to the rare process and the rate is altered, then such deviation will be sensitively detected.

The energy scale these rare processes correspond to can be 100 TeV or higher, which provides a method to measure high energy physics beyond the energy of existing accelerator. On the down side, FCNC processes are rare, therefore they usually require a high luminosity beam and a good handle of the vast background.

To conclude, for the study of FCNC process physics, usually referred as precision measurements, rates or other quantities of SM highly suppressed processes are measured. If any deviation from the SM is observed, it will be a tool to guide new physics models or exclude some parameter space of some new theories.

1.3.2 SM Prediction of the Branching Ratio

In the SM, there are two types of diagrams contributing to the branching ratio shown in Figure 1.1: the Z^0 penguin diagrams and the box diagram. It is helpful to note that for the Z^0 penguin diagrams, the internal top quark dominates due to its large mass, and the charm quark dominates the box diagrams because it has similar mass to the leptons in the loop.

The effective Hamiltonian describing $K^+ \to \pi^+ \nu\bar{\nu}$ and $K_L^0 \to \pi^0 \nu\bar{\nu}$ has the form (*Buras et al.* (2008)):

$$H_{eff}^{SM} = \frac{G_F}{\sqrt{2}} \frac{\alpha}{2\pi sin^2\theta_w} \sum_{l=e,\mu,\tau} (V_{cs}^* V_{cd} X_{NL}^l + V_{ts}^* V_{td} X(x_t))(\bar{s}d)_{V-A}(\bar{\nu}_l \nu_l)_{V-A} \qquad (1.4)$$

where V_{ij} are CKM matrix elements which we will discuss in section 1.3.3.

Different terms will be explained below: the first X_{NL} term describes the contribution from charm quark mediated box diagram, and the second term is from the penguin diagram contribution with $x_t = m_t^2/M_W^2$, and $X(x_t)$ is a monotonically increasing function with respect to x_t. The above Hamiltonian includes the next-leading-order and next-next-leading-order QCD corrections.
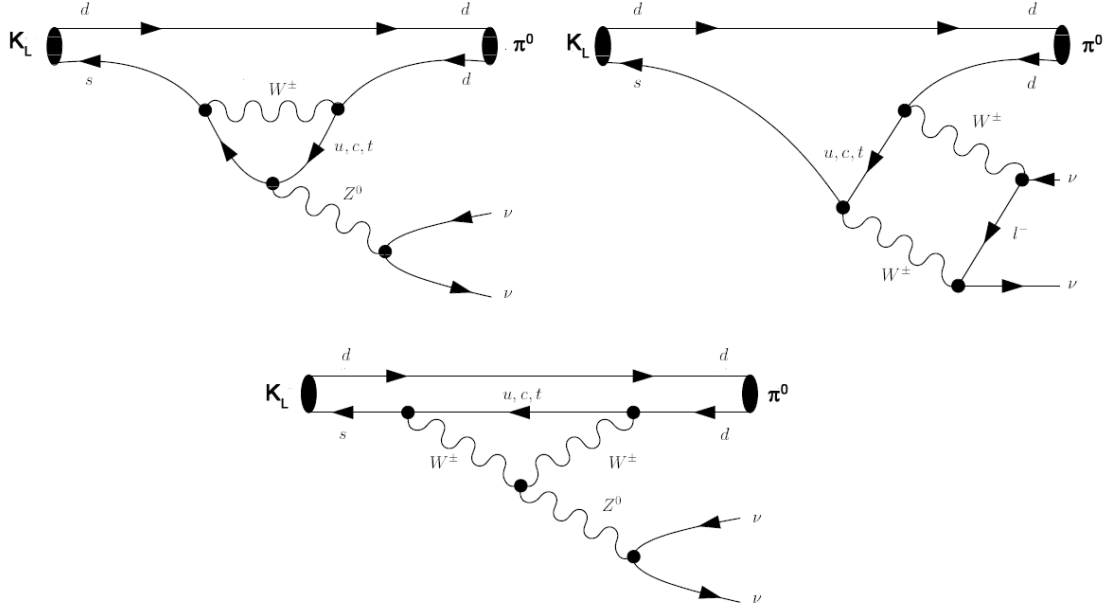
Figure 1.1: Standard Model Feynman diagrams contributing to $K_L^0 \to \pi^0 \nu \bar{\nu}$

The decay $K_L^0 \to \pi^0 \nu \bar{\nu}$ can be compared to $K^+ \to \pi^+ \nu \bar{\nu}$. The neutral kaon decay, because the neutrino pair is in a CP even eigenstate, is pure CP violating. As a result, the charm quark contribution is only approximately 1% , and can be neglected. So the branching ratio can be expressed as

$$Br(K_L^0 \to \pi^0 \nu \bar{\nu}) = \kappa_L \left(\frac{Im \lambda_t}{\lambda^5} X(x_t) \right)^2 \qquad (1.5)$$

where $\kappa_L = (2.231 \pm 0.013) \times 10^{-10} \left[\frac{\lambda}{0.225} \right]^8$.

Here, the λ is $|V_{cb}|$ and the $\lambda_t = V_{ts}^* V_{td}$. $K_L^0 \to \pi^0 \nu \bar{\nu}$ has very small theoretical

uncertainties. The K_L^0 form factor does not depend on lattice QCD calculations, which has big uncertainties. Instead, it can be extracted from K_L^0 semi-leptonic decay rates. The parametric uncertainties in the expression resides in three parts: m_t, $\text{Im}\lambda_t$ and κ_L.

This section will be concluded by citing the numerical results for equation 1.5. the SM calculation on the $K_L^0 \to \pi^0 \nu \bar{\nu}$ branching ratio including 2-loop QCD and electroweak contribution is $(2.43 \pm 0.39 \pm 0.06) \times 10^{-11}$, and total theoretical uncertainties is 2.5%. The first error is parametric uncertainties from CKM matrix elements and the second error is from remaining theoretical uncertainties from higher order diagrams(*Brod et al.* (2011)).

1.3.3 Accurate Measurement of the CKM Unitarity Triangle

The CKM matrix represents the transformation between the flavor eigenstates and mass eigenstates of three generations of quarks.

$$V_{CKM} = \begin{pmatrix} V_{ud} & V_{us} & V_{ub} \\ V_{cd} & V_{cs} & V_{cb} \\ V_{td} & V_{ts} & V_{tb} \end{pmatrix}$$

One property of the CKM matrix is that it's "mostly diagonal". Numerically, the off-diagonal entries are $|V_{us}| = 0.23$, and $|V_{ub}| = 4.2 \times 10^{-3}$. To better show the mostly diagonal structure of the CKM matrix, the Wolfenstein parameterization

(*Wolfenstein* (1983)) defined below, is often used.

$$\lambda = \frac{|V_{us}|}{\sqrt{|V_{ud}|^2 + |V_{us}|^2}}, \tag{1.6a}$$

$$A = \frac{1}{\lambda}\left|\frac{V_{cb}}{V_{us}}\right|, \tag{1.6b}$$

$$V_{ub}^* = A\lambda^3(\rho + i\eta) = \frac{A\lambda^3(\bar\rho + i\bar\eta)\sqrt{1 - A^2\lambda^4}}{\sqrt{1 - \lambda^2}[1 - A^2\lambda^4(\bar\rho + i\bar\eta)]}. \tag{1.6c}$$

$$V_{CKM} = \begin{pmatrix} 1 - \lambda^2/2 & \lambda & A\lambda^3(\rho - i\eta) \\ -\lambda & 1 - \lambda^2/2 & A\lambda^2 \\ A\lambda^3(1 - \rho - i\eta) & -A\lambda^2 & 1 \end{pmatrix} \tag{1.6d}$$

The equation 1.6c looks very cumbersome and unnatural, but it turns out that with this definition, the parameters $\bar\rho$ and $\bar\eta$ will be the apex of the Unitarity Triangle (UT), which will be discussed further.

CKM matrix is a unitarity matrix, i.e.

$$V_{ud}V_{ub}^* + V_{cd}V_{cb}^* + V_{td}V_{tb}^* = 0 \tag{1.7}$$

This equation, if drawn in the complex plane, will form a triangle for which the vertices are $(0,0),(1,0)$ and $(\bar\rho, \bar\eta)$. The equation 1.5, if represented in the Wolfenstein parameters, will become

$$Br(K_L^0 \to \pi^0 \nu\bar\nu) = \bar\kappa_L \eta^2 |V_{cb}|^4 X^2(x_t) \tag{1.8}$$

So the branching ratio of $K_L^0 \to \pi^0\nu\bar\nu$ is proportional to the height of the unitarity triangle. Accurate measurement of $K_L^0 \to \pi^0\nu\bar\nu$ branching ratio therefore can give accurate measurement of CKM parameter $\bar\eta$ in lack of hadronic uncertainties.

We will not dig into the similar discussion for K^+ decay but will simply cite the result: the branching ratio of K^+ decay is proportional to one side of the UT as
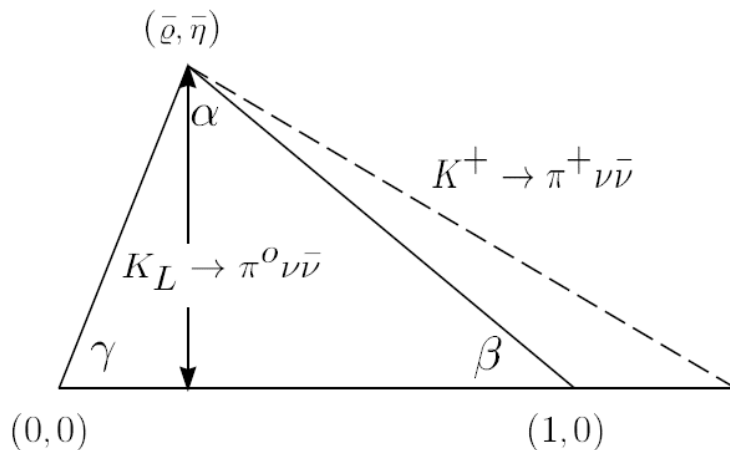
Figure 1.2: The Unitarity Triangle with the $K \to \pi\nu\nu$ branching ratio labeled. The dotted line demonstrates potential new physics contributions

shown in Figure 1.2. There exists a "golden" relation from which the measurement of the two branching ratios can determine the UT completely. Specifically, the angle β can be measured with high accuracy free from any hadronic uncertainties. At the same time, the angle β can also be derived from another path of the CP asymmetry of $B \to \psi K_S$ decay. When considering the BSM extensions, however, the golden relation will be broken in different ways and can be experimentally identified.

1.3.4 Grossman-Nir Bound

We've seen that it is hard to talk about $K_L^0 \to \pi^0\nu\bar{\nu}$ without constantly referring to its charged counterpart $K^+ \to \pi^+\nu\bar{\nu}$, since they both go under the same Feynman diagrams at quark level. There's a bound called Grossman-Nir bound which gives an upper limit on the branching ratio of the neutral decay with respect to the charged decay by giving(*Grossman and Nir* (1997))

$$Br(K_L^0 \to \pi^0\nu\bar{\nu}) < 4.4 \times Br(K^+ \to \pi^+\nu\bar{\nu}) \tag{1.9}$$

The bound is derived using only the isospin symmetry and is model independent.

The angle θ is defined to be the relative phase between the $K - \bar{K}$ mixing and $s \to d\nu\bar{\nu}$ decay amplitude. And the following identity is straightforward to be derived:

$$\frac{\Gamma(K_L^0 \to \pi^0 \nu\bar{\nu})}{\Gamma(K_S \to \pi^0 \nu\bar{\nu})} = tan^2\theta \qquad (1.10)$$

At the same time, isospin symmetry gives $A(K^0 \to \pi^0 \nu\bar{\nu})/A(K^+ \to \pi^+ \nu\bar{\nu}) = 1/\sqrt{2}$. Considering the isospin breaking factor to be 0.954 (*Marciano and Parsa* (1996)), and the lifetime of the two kaons $\tau_{K_L^0}/\tau_{K^+} = 4.17$, the equation 1.9 can be obtained.

1.4 Probing the Beyond Standard Models

We've known that the complex phases in the off-diagonal elements of the CKM matrix will contribute to CP violation. Then the question to ask is whether such contribution is enough. The Hamiltonian describing the kaon decays in equation 1.4 is generic and model independent. For various beyond standard Models (BSMs), the difference entirely resides in the funtion $X(x_t)$ and an additional complex phase is brought in.

$$X = |X|e^{i\theta_X} \qquad (1.11)$$

In the next few sections, the impact of different BSMs on the amplitude or the complex phase of the X function will be reviewed.

1.4.1 BSMs with Minimum Flavor Violation (MFV)

MFV is a catagory of simplest SM extensions. Under MFV assumption, the contribution of new operators not present in SM is neglegible, so only the (V-A) $\otimes$(V-A) operators identical to equation 1.4 are kept. And the phase in the CKM matrix is still the only contribution to the CP violation. All the SM extensions with MFV have the complex phase $\theta_x = 0$ or π. However, they affect the amplitude by introducing diagrams with new particles in the internal loop.

To be explicit, the function $X(x_t)$ should be replaced by a real-valued function $X(\nu)$ and ν represents a set of parameters of a given MFV model. Moreover, the $X(\nu)$ function can be either positive or negative according to different θ_x (Later analysis shows that the negative solution is neglegible). The model independent result which is related to $K_L^0 \to \pi^0 \nu \bar{\nu}$ is that it gives a tighter bound of its branching ratio with respect to $K^+ \to \pi^+ \nu \bar{\nu}$ shown below:

$$B_1 = B_2 + \left[\frac{cot\beta\sqrt{B_2} + sgn(X)\sqrt{\sigma}P_c(X)}{\sigma} \right]^2 \qquad (1.12)$$

where B_1 and B_2 are the reduced branching ratios: $Br(K^+ \to \pi^+ \nu \bar{\nu})/\kappa^+$ and $Br(K_L^0 \to \pi^0 \nu \bar{\nu})/\kappa_0$ respectively, and the angle β is unfixed but can be calculated from $a_{\psi K_s}$, and σ is a constant equals $\left(\frac{1}{1-\frac{\lambda^2}{2}} \right)^2$. Recall the latest experimental result of $K^+ \to \pi^+ \nu \bar{\nu}$ branching ratio measurement: (*Adler et al.* (2008))

$$Br(K^+ \to \pi^+ \nu \bar{\nu}) = (1.73^{+1.15}_{-1.05}) \times 10^{-10} \qquad (1.13)$$

and $a_{\psi K_S} \le 0.719$, we can get in MFV models, the upper limit of $K_L^0 \to \pi^0 \nu \bar{\nu}$ branching ratio is 2.0×10^{-10}.

To conclude, with the improved measurements of $a_{\psi K_s}$ from B meson decays, the MFV extensions will not allow too much deviation from the SM. This indicates that if large deviation of the branching ratio is observed (a factor of 2 larger, for example), new CP violating phases must exist.

1.4.2   SM Extensions with Large θ_X

We start with a model independent discussion. In this case, the $X(x_t)$ function will be complex as expressed in equation 1.11. The K_L^0 branching ratio is changed to

$$Br(K_L^0 \to \pi^0 \nu \bar{\nu}) = \bar{\kappa}_L \eta^2 |V_{cb}|^4 |X|^2 sin^2\beta_X \qquad (1.14)$$

where $\beta_X = \beta - \beta_s - \theta_X$, and β and β_s are phases of V_{td} and V_{ts}. Figure 1.3 shows the branching ratios of K^+ and K_L^0 decays with scanning different values of β_X and $|X|$.

1.4.2.1 Littlest Higgs Model with T-parity

The Littlest Higgs Model is that the global SU(5) symmetry is spontaneously broken into SO(5) at 1 TeV energy scale, and new particles are introduced including the heavy gauge bosons $W_H^\pm$, Z_H and A_H, the heavy top T and scalar triplet Φ. One of the merits of the Littlest Higgs model is that it resolves the quadratic divergence of the Higgs mass by introducing new diagrams from these new particles. One of the series of Littlest Higgs Model that is very sensitive to $K_L^0 \to \pi^0 \nu \bar\nu$ branching ratio is the Littlest Higgs model with T symmetry(LHT). With this extra symmetry requirement, new quarks and leptons are introduced. Their interactions with the SM quarks involves new unitarity matrices, and new flavor violating phases are introduced therein. Here, we simply cite the relevant results without digging deeper into theoretical discussions. First of all, a large range of $|X|$ and θ_X can be predicted:

$$0.7 \leq |X| \leq 4.7, and - 130° \leq \theta_X \leq 55° \tag{1.15}$$

As a consequence, an enhancement of the $K_L^0 \to \pi^0 \nu \bar\nu$ branching ratio is possible. Figure 1.4 shows the predictions of the two kaon branching ratios under different senarios of LHT, as shown by different colors. We can observe two branches, one of which shows no significant deviation from the SM, where the other shows large enhancement of the neutral mode, assuming that the K^+ branching ratio is less than 2×10^{-10}.
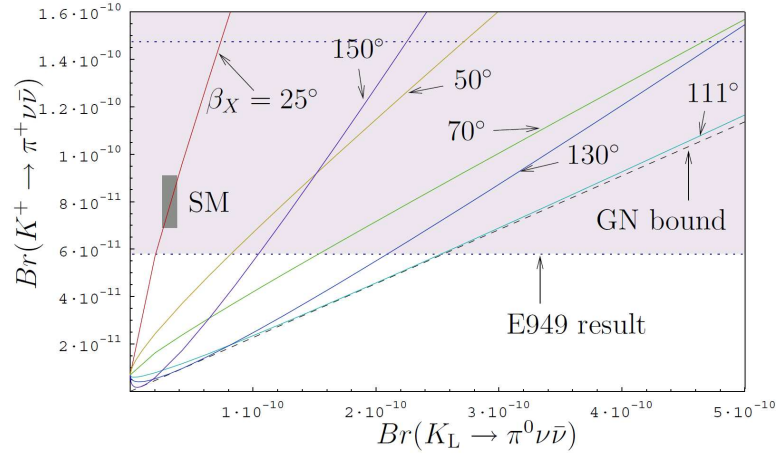
(a)
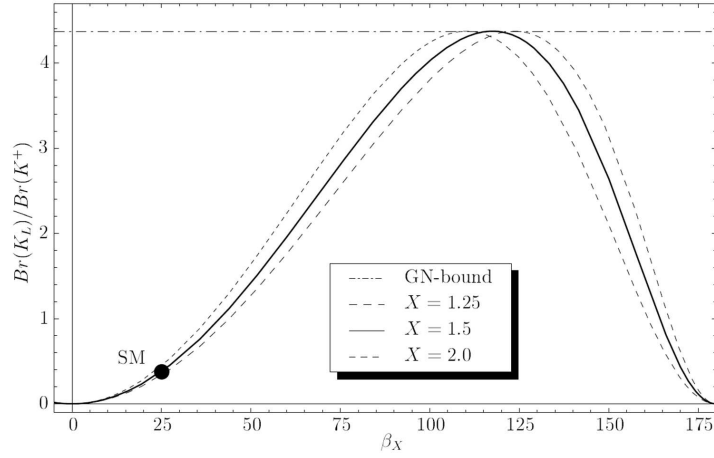
(b)

Figure 1.3: A model independent result of BSM models with large θ_X. (a) β_X is scanned. This plot in independent of $|X|$. (b) $|X|$ is scanned and the Br($K^+ \to \pi^+\nu\bar\nu$)/Br($K_L^0 \to \pi^0\nu\bar\nu$) with respect to different β_X is plotted. The horizontal dotted line is the Grossman-Nir bound.
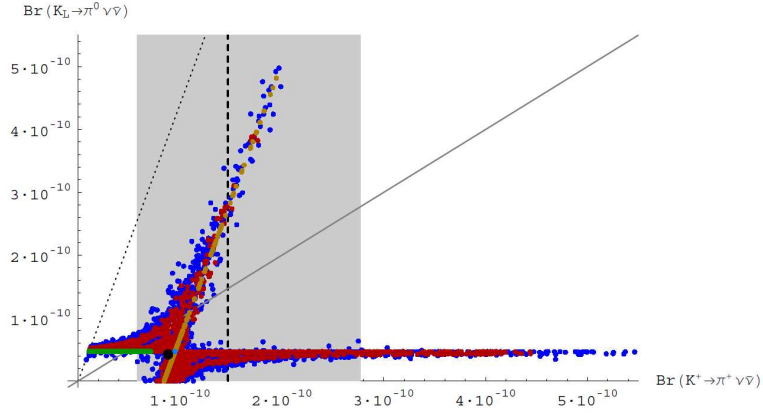
Figure 1.4: The $\text{Br}(K^+ \to \pi^+\nu\bar{\nu})$ vs $\text{Br}(K^0_L \to \pi^0\nu\bar{\nu})$ plot inside LHT models. The shaded area represents the experimental 1 σ range of $\text{Br}(K^+ \to \pi^+\nu\bar{\nu})$. The dotted line is Grossman-Nir bound, and the solid has slope 1. Different colors of dots means different senarios.

1.4.2.2 Minimal Supersymmetric Model

Minimal Supersymmetric Standard Model (MSSM) is another way to resolve the Higgs quadratic divergence by doubling the number of fields. Flavor violation is natural from the Yukawa superpotential. In the superpotential, relavant terms are expressed

$$W_{Yukawa} = \lambda_u^{ij} Q_i U_j H_u + \lambda_d^{ij} Q_i D_j H_d \tag{1.16}$$

(*Murayama* (2000)) where λ_u^{ij} and λ_d^{ij} are the coupling constants between family i and j, which is similar to the CKM matrix. Q, U and D are chiral multiplets, and H_u and H_d are two Higgs fields. In general, the two coupling matrices cannot be diagonalized simultaneously, so terms violating flavor number exist. One of the mechanisms is to introducing diagrams from chargino loops and neutralino loops shown in Figure 1.5(*Buras et al.* (1998)). The other of the mechanisms for enhancement is from charged Higgs mediated penguine diagrams in the region of large $tan\beta$ whose diagrams are shown in Figure 1.6(*Isidori and Paradisi* (2006)). In both cases, sizable deviation from SM is possible within some parameter range.
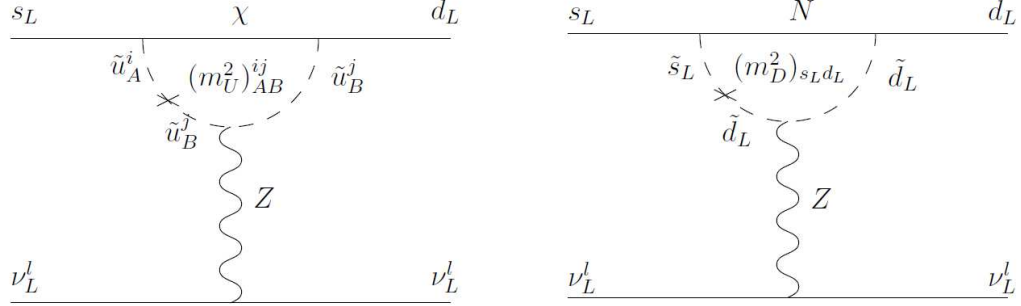
Figure 1.5: Feynman diagrams contributing to $K_L^0 \to \pi^0 \nu \bar{\nu}$ in the general SUSY. (a) chargino loop. (b) neutralino loop.
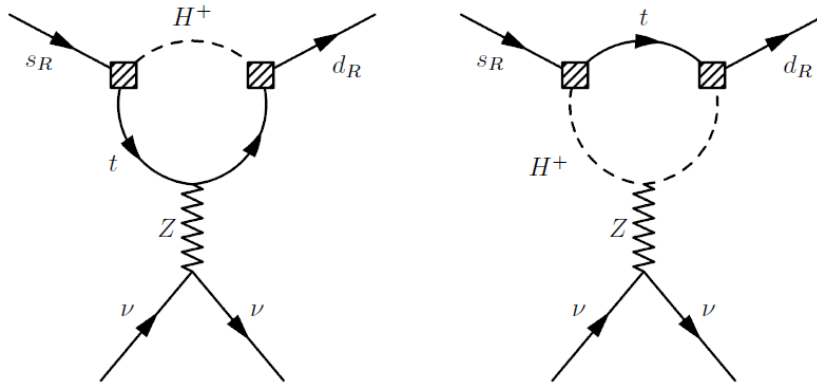
Figure 1.6: Charged Higgs mediated diagrams contributing to $K_L^0 \to \pi^0 \nu \bar{\nu}$ decay in general SUSY.
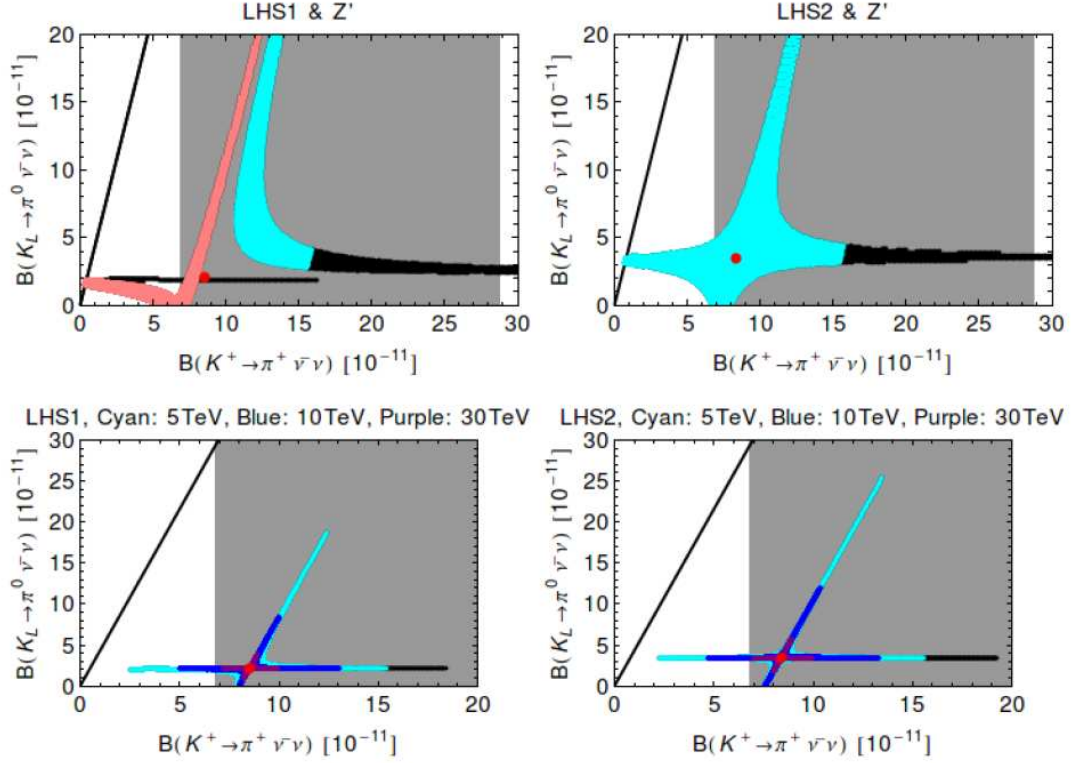
Figure 1.7: $\mathrm{Br}(K_L^0 \to \pi^0 \nu \bar{\nu})$ vs $\mathrm{Br}(K^+ \to \pi^+ \nu \bar{\nu})$ in different senarios of Z' models. Pink, cyan blue and purple regions correspond to Z' mass of 1 TeV, 5 TeV, 10 TeV and 30 TeV. Grey region is the experimental range.

1.4.2.3 Z' Models

Z' is proposed in different BSMs and is able to mediate FCNC at tree level. (*Buras* (2013)) From a general point, the mass of the Z' and the coupling constant (for example, how the left-handed current and right-hand current couple), will determine the branching ratios. As shown in Figure 1.7, in different charge coupling senarios and different masses, sizable deviation can be expected, but with increasing Z' mass, the abundance is reduced.

1.5   History of Experimental Searches

The best upper bound comes from the branching ratio measurement of $K^+ \to \pi^+ \nu \bar{\nu}$ by E949 collaboration in Brookhaven National Lab and the Grossman-Nir

bound. As stated before, the upper limit of K^+ decay ratio is $(1.73^{+1.15}_{-1.05}) \times 10^{-10}$. And Grossman-Nir bound relation (equation 1.9) infers the K^0_L decay rate to be 7.6×10^{-10}.

E391a was a dedicated experiment for $K^0_L \to \pi^0 \nu \bar{\nu}$ search in KEK from 1999 to 2007 using the 12 GeV proton synchrotron. No signal event was observed in E391a, and an upper limit of 2.6×10^{-8} was set (*Ahn et al.* (2010)). The largest background comes from halo neutrons in the beam line interacting with detectors. The KOTO experiment is based on similar experimental method with a new beam line, upgraded detectors and DAQ system.

1.6   Conclusion

$K^0_L \to \pi^0 \nu \bar{\nu}$ is of great physics importance. Its theoretical uncertainties are small. It is a great approach for accurate measurement of CKM matrix elements ($\bar{\eta}$). And an accurate measurement will help exclude parameter ranges for various BSM extensions. The best measurement is from E391a experiment, and its sensitivity is one order of magnitude larger than Grossman-Nir bound and the K^+ branching ratio measurement.

CHAPTER II

Experimental Method

2.1   Overview

The goal of the experiment is to measure the branching ratio of $K_L^0 \rightarrow \pi^0 \nu \bar{\nu}$: $Br(K_L^0 \rightarrow \pi^0 \nu \bar{\nu}) = \Gamma(K_L^0 \rightarrow \pi^0 \nu \bar{\nu})/\Gamma_{total}$, where Γ denotes the K_L^0 total decay rate. In the experiment, the branching ratio is calculated from

$$Br(K_L^0 \rightarrow \pi^0 \nu \bar{\nu}) = \frac{N_{signal}}{N_{K_L^0} \times A_{signal}} \tag{2.1}$$

In the above equation, N_{signal} is the number of reconstructed $K_L^0 \rightarrow \pi^0 \nu \bar{\nu}$ events, $N_{K_L^0}$ is the number of K_L^0 generated at target, and A_{signal} is the acceptance of the signal mode. The focus of the experiment is to identify the three variables in Equation 2.1.

To calculate N_{signal}, a set of cuts which could select the signal events while rejecting the backgrounds should be defined. The signal has neutrinos in the decay product, so a missing transverse momentum (P_T) is expected. Besides, the π^0 has 98.8% chance to decay into two photons, which can be a uniquely reconstructed vertex. So the signal events should have only two photons plus missing P_T in their final states. In the final analysis, a signal box is defined in the Z_{vertex} vs P_T plane as shown in Figure. 2.1(*Sumida* (2008)).

N_{decay} is the number of K_L^0 generated at the target (K_L^0 flux) . This number is
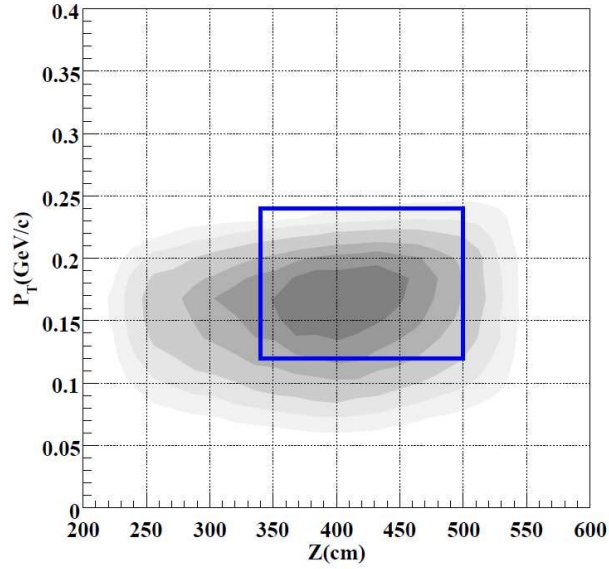
Figure 2.1: The Z_{vertex} and P_T distribution of Monte Carlo $K_L^0 \to \pi^0 \nu \bar{\nu}$ events. The signal box defined by the blue box.

measured from the decay modes with large branching ratios and therefore large statistics like neutral modes $K_L^0 \to \pi^0 \pi^0 \pi^0$, $K_L^0 \to \pi^0 \pi^0$ and $K_L^0 \to \gamma\gamma$. The three modes above are called the normalization modes, and K_L^0 flux is measured independently for each mode with the result shown in Chapter VI. Equation 2.2 shows the method of calculation K_L^0 flux.

$$N_{K_L^0} = \frac{N_{sig,data}}{A_i \times Br_i} \tag{2.2}$$

where

$$A_i = \frac{number\ of\ events\ after\ all\ cuts\ in\ MC}{number\ of\ generated\ K_L^0} \tag{2.3}$$

The A_{signal} includes the geometric acceptance and the cut acceptance. The geometric acceptance is the probability of the events where all the decayed products can be detected by the detector. And the cut efficiency is the probability of events which passed the set of selection cuts.

To better illustrate the combinational effects of $N_{K_L^0} \times A_{signal}$, a variable called

18

Single Event Sensitivity (SES) is defined as

$$SES = \frac{1}{N_{K_L^0} \times A_{signal}}.$$ (2.4)

As a result, the average number of observed events (N_{signal}) is expressed as $Br(K_L^0 \to \pi^0 \nu \bar{\nu})/SES$. We want to observe more events in the experiment. That means both $N_{K_L^0}$ and A_{signal} need to be as large as possible, and the experiment was designed with this guide. Important factors that affect the SES are beam energy and power, the beam line, production target design, the detector geometry and efficiency, and mostly importantly, the run time. These factors will be described in the following sections of this chapter.

In reality, there are sources of event loss due to over-vetoing of events (for example, veto detectors have energy leaked from the other detectors), accidental loss (an accidental hit of the veto detectors generates a fake veto). To take these factors into consideration, the Equation 2.1 should have a loss term:

$$Br(K_L^0 \to \pi^0 \nu \bar{\nu}) = \frac{N_{signal}}{N_{K_L^0} \times A_{signal} \times (1 - \Delta)}$$ (2.5)

where the $(1 - \Delta)$ term includes all the loss sources

$$1 - \Delta = \prod_i (1 - \Delta_i)$$ (2.6)

and i are the sources of loss. Similarly, the equation 2.4 should be redefined as

$$SES = \frac{1}{N_{K_L^0} \times A_{signal} \times (1 - \Delta)}.$$ (2.7)

To conclude, if one or more signal events are observed, the estimation of $Br(K_L^0 \to \pi^0 \nu \bar{\nu})$ can be extracted from equation 2.5. Otherwise, an upper limit of the branching

ratio is calculated.

2.2 Experimental Strategy

2.2.1 Signal Reconstruction

From the arguments in Section 2.1, we know that in order to calculate N_{signal} and N_{decay}, we need to first reconstruct the $\pi^0 \to \gamma\gamma$ vertex. In our experiment, we want to use the electromagnetic calorimeter made of arrays of pure CsI at the endcap to detect the energy and position of the two γs. But the CsI calorimeter doesn't have such good angle resolution that the incident angles of the photons can be known. In order to do the kinematic reconstruction, some extra constraints of the decay vertex are needed. In the experiment, we require that the K_L^0 beam to be narrow such that the transverse decay position can be treated as being at origin.

Events with only two photons hitting CsI calorimeter and no veto signals are selected. Using the π^0 mass as a constraint, the decay Z vertex (Z_{vertex}) and transverse momentum (P_T) can be determined.

2.2.2 Background Veto

A success of detection requires a high efficiency of background vetoing. There are two categories of background: other K_L^0 decays and beam halo neutrons.

Table 2.1 shows the main K_L^0 decay modes. Among all, 80% of the decay modes have charged particles, so making a charged veto covering the 4π radius angle will effectively remove these modes. The remaining 20% are neutral modes, so a hermetic photon veto system is also required.

The beam background mainly comes from the halo neutrons. When they interact with the detector material close to the beam line, or with the residual gas in the detector region, a π^0 or η may be produced which will fake a real event. This back-

Table 2.1: K_L^0 main decay modes

Decay modes		Branching ratio
	$\pi^\pm e^\mp \nu_e$	40.55 ± 0.11 %
Charged Modes	$\pi^\pm \mu^\mp \nu_\mu$	27.04 ± 0.07 %
	$\pi^\pm \pi^\mp \pi^0$	12.54 ± 0.05 %
	$3\pi^0$	19.52 ± 0.12 %
Neutral Modes	$\pi^0 \pi^0$	$(8.64 \pm 0.06) \times 10^{-4}$
	$\gamma\gamma$	$(5.47 \pm 0.04) \times 10^{-4}$

ground source is the main source in the E391a experiment. To reduce it, material close to the beam hole should be avoided. High vacuum system is also required.

Accidental activities from the beam line will not only contribute to the online accidental loss, but will also be a source of background. For example, a $K_L^0 \to \pi^0\pi^0$ event might have two small energy photons hitting the photon veto detector, but a big off-timing accidental hit on the photon veto will mask the true veto hit. To remove this effect, our data acquisition system should be able to have both good timing resolution and pulse information to remove accidental hits.

2.3 Experimental Apparatus

2.3.1 Beam Line

The beam energy, power, extraction, shape and K_L^0 yield and neutron yield are the main attributes for the experiment. The E14 experiment uses the 30 GeV proton beam line in the Japan Proton Accelerator Research Complex (J-PARC). The proton beam is accelerated at three stages. The linear accelerator (LINAC) provides a primary acceleration to 180 MeV. A 3 GeV rapid cycling synchrotron (RCS) gives the second level boost and the 30 GeV main ring (MR) gives the final acceleration and extract the proton beam into the hadron experimental hall. The primary proton beamline has an average beam power of 24 kW. The timing structure is 6 second cycle with 2 seconds of extraction with a duty factor (defined in equation 2.8) of 42.8%.

$$duty = \left(\int\limits_{T_1}^{T_2} I(t)\, \mathrm{d}t \right)^2 \bigg/ \int\limits_{T_1}^{T_2} \mathrm{d}t \int\limits_{T_1}^{T_2} I(t)^2\, \mathrm{d}t \tag{2.8}$$

The primary proton beam is guided onto a T1 target (gold target), and the secondary beam with an extraction angle of 16 degrees passes through a series of absorbers, magnets and collimators (Figure 2.2), and a pencil beam including particles of K_L^0, neutrons, proton and gammas enters the detector system. There was a dedicated measurement of the K_L^0 yield measurements using the $K_L^0 \to \pi^+\pi^-\pi^0$ mode (*Shiomi et al.* (2012)), and the measurement result is $1.94 \times 10^7 K_L^0/2 \times 10^{14}$ Protons on Target(POT) for 5.4-cm-long Ni target and $4.19 \times 10^7 K_L^0/2 \times 10^{14}$ POT for 6-cm-long Pt target.
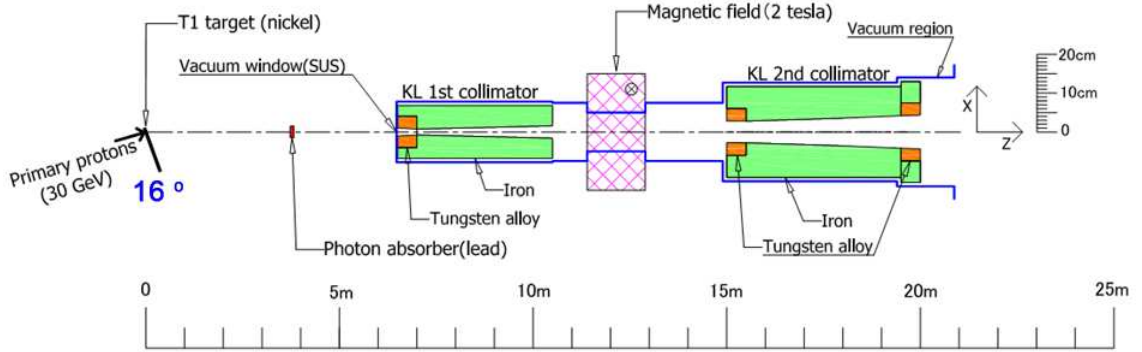
Figure 2.2: Schematic view of the K_L^0 beamline. The beam extraction angle is 16 degrees. A sequence of photon absorbers, two stages of collimators and a sweeping magnet in between two the two collimators is used to remove the the beam photons, charged particles and neutrons.

2.3.2 Detector System

The detector system includes an endcap electromagnetic calorimeter plus hermetic photon and charged veto, as shown in Figure 2.3.
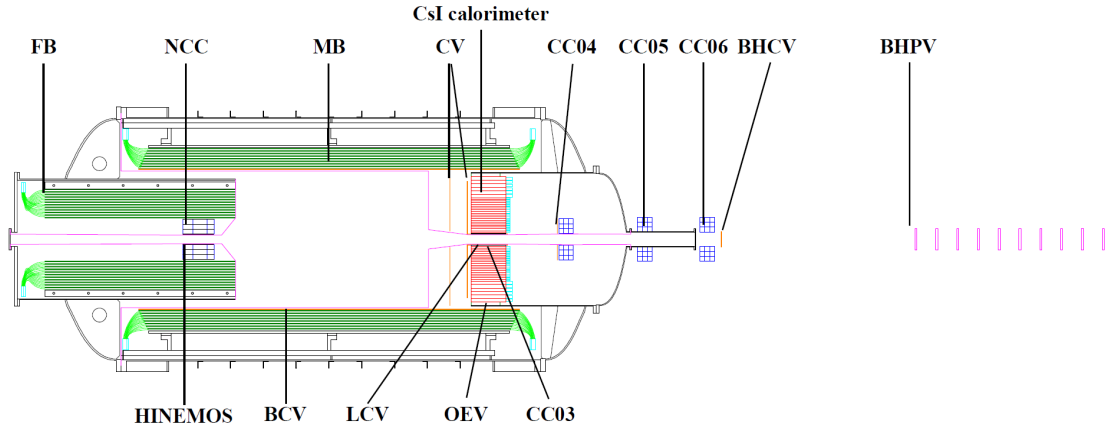
Figure 2.3: Side view of the KOTO detector.

2.3.2.1   CsI Calorimetor

The CsI calorimetor is an endcap electromagnetic calorimeter. The geometry of the CsI calorimeter is a cylindrially stacked CsI crystal arrays of 2716 crystals with a center beam hole. There are two sizes of CsI crystal: The center ones are $2.5 \times 2.5 \times 50 \ cm^3$, and the outer ones are $5 \times 5 \times 50 \ cm^3$. Note that the CsI radiation length (X_0) is 1.85 cm, and the Molière radius (R_M) is 3.8 cm. So the length corresponds to $27 \ X_0$, and the problem of photon punch through and shower leakage is minimized. The light yield is around 100 photo electrons (p.e.) per MeV. The energy resolution of the calorimeter is $\sigma_E/E = 2\%/\sqrt{E} \oplus 0.45\%$.

2.3.2.2   Barrel Photon Detector

The Barrel Photon Detector, usually referred as Main Barrel (MB), is the electromagnetic sampling calorimeter with a sandwiched structure made of lead and scintillator plates, covering the barrel region. It is used to detect the photons hitting the side of the barrel region. The MB detector was a reused one from E391a experiment, and its inefficiency was the main background contribution from $K_L^0 \to \pi^0\pi^0$ decay.

The Front Barrel (FB) has the similar structure as MB, and locates upstream to

complete photon veto hermicity backwards.

2.3.2.3   Charged Veto System

The main Charged Veto referred as CV is the detector in front of the CsI calorimeter to detect the charged particles hitting the endcap region. There are two layers of scintillating plates, each layer being made of scintillating strips, and different orientation in the front and rare plates combine to uniquely identify the x and y hit position. CV is made of light materials in order to reduce the neutron interaction background. Besides the main CV, there is an extra layer of scintillators inside the MB called Barrel Charged Veto (BCV) to detect the charged particles hitting the barrel region. Other charged veto detectors are implemented to complete the hermicity of charged veto detection: HINEMOS to veto the charged particles going backwards through the upstream beam hole, Liner CV(LCV) to veto the charged particles hitting the vicinity of the downstream beam hole, and Beam Hole charged veto (BHCV), to veto charged particles directed downstream, as well as charged particles from the primary beam line.

2.3.2.4   Neutron Collar Counters

Halo Neutron interaction with the neutrons hitting the detectors close to the beam hole (the NCC and CV) is the main source of background. The NCC has two goals: the first goal is to veto the halo neutron events, and the second one is to measure the neutron flux.

2.3.2.5   Collar Counters

A series of Collar Counters named by numbers from upstream to downstream as CC03-CC06 (CC01 and CC02 were removed from E391a and replace by NCC) to capture the photons escaping the beam hole.

2.3.2.6 Beam Hole Counters

There are a series of Beam Hole Photon Veto (BHPV) counters aligned in the primary beam line downstream of the detector system. Its goal is to capture the photons escaping through the beam hole of the CsI calorimeter.

2.3.3 Trigger and Data Acquisition System

The Data Acquisition is based on Analog to Digital Converter (ADC) front-end electronics and three layers of trigger system. Here we will give a brief introduction, and the details will be described in Chapter IV. The Level one (L1) trigger makes a fast trigger decision based on total energy of CsI calorimeter, and a combination of other veto signals for generating different trigger sets for different purposes. For physics trigger, for example, the L1 trigger requires a large CsI total energy and an absence of veto signals (shown in Table 2.2). The Level two (L2) trigger is both a data path and a trigger. The digitized data from the frond-end ADC will be sent and temporarily stored in the memory of the L2 boards before being sent to the L3 trigger. Since we require a large missing P_T for our physics events, the L2 will apply a cut based on the Center-of-Energy (CoE) of the CsI calorimeter. The Level 3 computer farm with 120 cores will apply further cuts depending on the number of clusters in the CsI, and do lossless compression to save space in the hard disk. Afterwards, the data will be transferred to the KEK computer center (KEKCC), and root files are produced for offline analysis.

2.4 Event Reconstruction

This section is a summary of the kinematic reconstruction method for finding the $K_L^0 \to \pi^0 \nu \bar{\nu}$ signal events. Reconstruction of normalization modes like $K_L^0 \to \pi^0 \pi^0 \pi^0$ and $K_L^0 \to \pi^0 \pi^0$ modes is also discussed.

Table 2.2: Level 1 physics trigger cuts

Detector	Threshold
CsI	>550 MeV
CV	<8000 ADC counts (2 MIP)
MB	<200 ADC counts (50 MeV)
NCC	<5000 ADC counts (100 MeV)
CC03	<3000 ADC counts (100 MeV)
CoE	>165 mm

Step 1: *Clustering.*

The electromagnetic showers the photons developed inside CsI typically spread through adjacent crystals. To identify the number of photons from the information of the CsI calorimeter, we first need to use the clustering method to group close-by crystals which have energy deposit. Afterwards, several corrections need to be performed to improve the reconstruction result.

The clustering method is described below: all the crystals with deposit energy >3 MeV are stored in a list. A random crystal (usually the first one in the list) is picked to be the seed of a new cluster, and one iteration is done to choose all the crystals in the list which are within a distance threshold $d_{threshold}(2.8 \times d_{small}$ (width of the small crystals)) with respect to the seed, i.e. $|x - x_{seed}| < d_{threshold}\&\&|y - y_{seed}| < d_{threshold}$. Once chosen, these new crystals become members of the cluster and are removed from the original list. Further iterations are done to pick all the crystals in the list which are within the distance range of each seed until all the crystals are checked. After this grouping process, we obtain a list of clusters, with the deposited energy

$$E_{cluster} = \sum_i e_i \tag{2.9}$$

where e_i is the deposit energy in the crystal i. The x and y position of the cluster is

the energy weighted x and y of all the crystals in the cluster calculated by

$$x_{cluster} = \frac{\sum_i x_i e_i}{\sum_i e_i}, y_{cluster} = \frac{\sum_i y_i e_i}{\sum_i e_i} \qquad (2.10)$$

and x_i and y_i are the center position of the crystal i. The z position is the front surface of the crystal. Due to the fact that the electromagnetic shower developes inside the crystal, we need to do a projection of the cluster position to the surface of the crystals. This step is described in step 2 as position correction. The RMS of the each cluster is calculated by

$$RMS = \frac{\sum_i E_i \times \sqrt{(x_i - x_{cluster})^2 + (y_i - y_{cluster})^2}}{\sum_i E_i} \qquad (2.11)$$

The RMS tells the shape of the cluster, and is a critical cut used to distinguish the merged clusters.

Step 2: *Gamma finding*

This step is to exclude the isolated clusters which might be caused by muons or particles other than photons. All the clusters with energy larger than 20 MeV represents a legitimate photon.

In this step, some corrections are applied. First of all, energy correction is needed, because the energy of the cluster is usually smaller than the energy of the true photon due to the energy leakage from the end or the side of the crystals and also from the 3 MeV energy cut we used in the clustering procedure. This discrepancy can be shown in Figure 2.4, and the energy correction uses the phenomenological equation (*Sato* (2007)):

$$E_{gamma} = (1 + f(E_{cluster})) \times E_{cluster} \qquad (2.12)$$

where the correction function $f(E_{cluster}, E_{threshold}, cos\theta)$ is a function of the cluster energy $E_{cluster}$, energy threshold $E_{threshold}$ and incident angle θ. Also, two types of

crystals should have different correction functions too. For example, for small crystals and an energy threshold of 3 MeV, the correction function is

$$f(E_{cluster}, 3MeV) = 0.014 + 0.052/\sqrt{E_{cluster}} - 0.0074 log(E_{cluster}) \qquad (2.13)$$

where the $E_{cluster}$ is in unit of GeV.
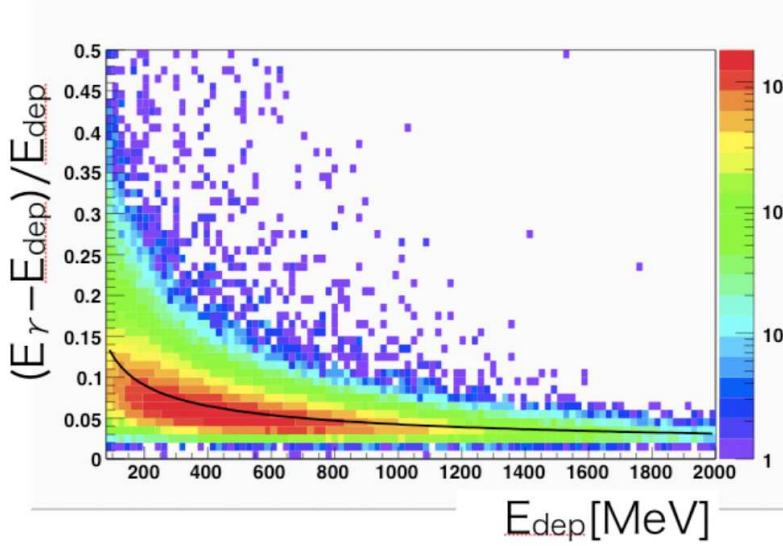
Figure 2.4: The correlation of the ratio of true photon energy and deposit energy difference and deposit energy. The black line is $F = 0.00362 + 0.0388/\sqrt{E_{dep}}$. This figure is taken from *Sato* (2007), and the parameters are different from the ones cited in text. Threshold is also different (1.5MeV).

A position correction is needed, because when the electromagnetic shower develop in the CsI crystals, the shower maximum P_{coe}, which are collected from the end of PMTs are usually off from the hit point projected to the surface of the CsI crystals P_{inc} as shown in Figure 2.5. The offset depends on the photon incident angle.

$$P_{inc} = P_{coe}(1 - Lsin\theta) \qquad (2.14)$$

28

where L is the shower length, which depends on the energy of the shower by

$$L(cm) = X_0 \times (6.49 + 0.992 log(E_{cluster}))$$ (2.15)

The parameters are obtained from Monte Carlo, and $E_{cluster}$ is in unit of GeV. We don't know the incident angle before the reconstruction is done, so correction iterations need to be done after the reconstruction without the position correction is done.
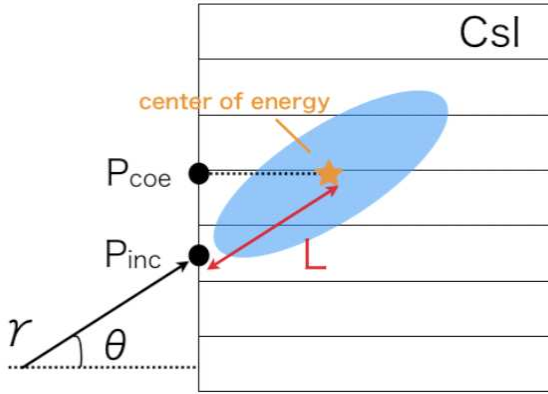
Figure 2.5: Schematics of the development of electromagnetic shower, and the discrepancy between the incident position P_{inc} and the detected position P_{coe} is shown.

After the angle is obtained from the 1st iteration of reconstruction, the energy needs to be re-corrected, since the energy leakage depends on the incident angle as well. A template of the energy correction function $f(E_{cluster}, E_{threshold}, cos\theta)$ is extracted from MC, and based on the template, the correction function is obtained by having a linear interpolation for $cos\theta$ and $E_{threshold}$, and a spline interpolation for $E_{cluster}$.

Step 3: *Vertex reconstruction*

When the positions and deposit energies of the photons are obtained, we are able to reconstruct the π^0 decay vertex assuming the fixed π^0 mass. From conservation of

momentum.

$$p^\mu_{\pi^0} p_{\pi^0 \mu} = (p_1 + p_2)^\mu (p_1 + p_2)_\mu \tag{2.16}$$

where $p^\mu_{\pi^0}$ is the four-momentum of π^0, and p^μ_1 and p^μ_2 are the four-momentum of the two photons. In the π^0 center of mass frame, $p^\mu_{\pi^0} p_{\pi^0 \mu} = -M^2_{\pi^0}$, and in the laboratory frame,

$$(p_1 + p_2)^\mu (p_1 + p_2)_\mu = -E_1 E_2 + \vec{p_1} \cdot \vec{p_2}$$
$$= -2E_1 E_2 (1 - cos\theta)$$

So the relation obtained from the Lorentz invariance is

$$cos\theta = 1 - \frac{M^2_{\pi^0}}{2E_1 E_2} \tag{2.17}$$

Also, we have a geometric relation shown in Figure 2.6, that

$$cos\theta = \frac{d^2_1 + d^2_2 - r^2_{12}}{2d_1 d_2} \tag{2.18}$$

From the two equations above, the decay vertex z position (Z_{vtx}) can be obtained.

In the case of $K^0_L \to \pi^0 \pi^0 \pi^0$ and $K^0_L \to \pi^0 \pi^0$, 6-photon and 4-photon events are selected, and π^0 reconstruction is done for all combinations of each two photons (there are $C^2_6 = 15$ combinations for $3\pi^0$ final state, and $C^2_4 = 6$ combinations for $2\pi^0$ final state). The best pairing with the smallest of χ^2 defined as $\chi^2 = \sum_{i=1}^{3} [Z_{K^0_L} - Z_{vtx}(i)]^2 / \sigma_{vtx}(i)$ is selected. In the $3\pi^0$ case, the K^0_L decay vertex
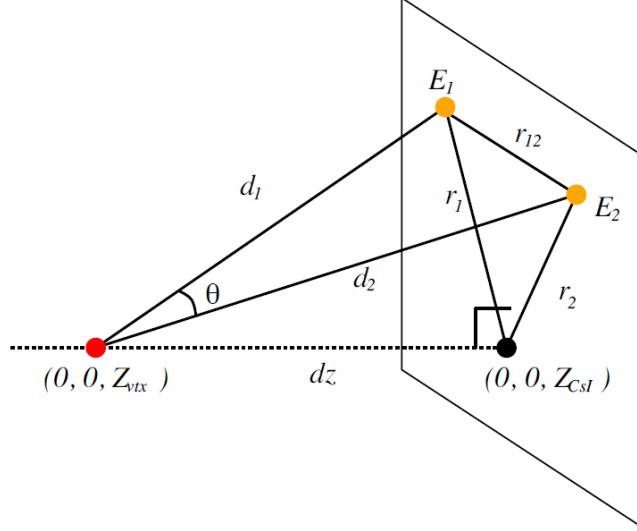
Figure 2.6: Schematic figure of the π^0 reconstruction from two photons in the CsI calorimeter.

$(X_{K_L^0}, Y_{K_L^0}, Z_{vtx})$ is

$$Z_{vtx} = \frac{\sum\limits_{i=1}^{3}[Z_{vtx}(i)/\sigma_{vtx}(i)]^2}{\sum\limits_{i=1}^{3}[1/\sigma_{vtx}(i)^2]} \tag{2.19a}$$

$$X_{K_L^0} = \frac{Z_{vtx} - Z_{target}}{Z_{CsI} - Z_{target}} \sum_{i=1}^{6} E_\gamma X_\gamma(i)/E_{K_L^0} \tag{2.19b}$$

$$Y_{K_L^0} = \frac{Z_{vtx} - Z_{target}}{Z_{CsI} - Z_{target}} \sum_{i=1}^{6} E_\gamma Y_\gamma(i)/E_{K_L^0} \tag{2.19c}$$

and the K_L^0 energy and momentum is obtained by

$$E_{K_L^0} = \sum_{i=1}^{6} E_\gamma(i) \tag{2.20a}$$

$$P_{K_L^0} = \sum_{i=1}^{3} p_{\pi^0}(i) \tag{2.20b}$$

31

2.5 Conclusion

In this chapter, we introduced the method of measuring the branching ratio of $K_L^0 \to \pi^0 \nu \bar{\nu}$. The focus is to discuss the measurement of the three variables: the number of signals (N_{signal}), the K_L^0 flux, and the signal acceptance (A_{signal}). To identify the $K_L^0 \to \pi^0 \nu \bar{\nu}$ decay, a selection rule of *selecting events with only two photons and large P_T* is used, and the detector system should be able to reconstruct the decay vertex as well as veto background events.

CHAPTER III

Detectors and Calibration Methods

3.1 Overview

This chapter will have detailed description of important detector properties and calibration method of the most important detectors: CsI and MB detectors which I devoted my efforts to.

3.2 CsI Electromagnetic Calorimeter

3.2.1 Structure

The geometry of CsI calorimeter was introduced in Chapter 2.3.2.1. The x-y plane view is shown in Figure 3.1.(a) as well as a picture of it in 3.1.(b).

Each CsI crystal is wrapped by aluminized mylar to reduce gas permeability and increase light reflection. At the downstream of the CsI crystals, there are the silicone cookie and the UV filter before the cathode of PMT. The silicone cookie is to increase transmission, and the UV filter will filter out the fast component of the Cherenkov light, which has a reduced transparency. The PMTs works at high voltages around 1500 V, supplied by a Cockcroft-Walton (CW) base (*Masuda* (2013)) with the features of low bleeding current and low noise. The structure of each CsI crystal is sketched in Figure 3.2.
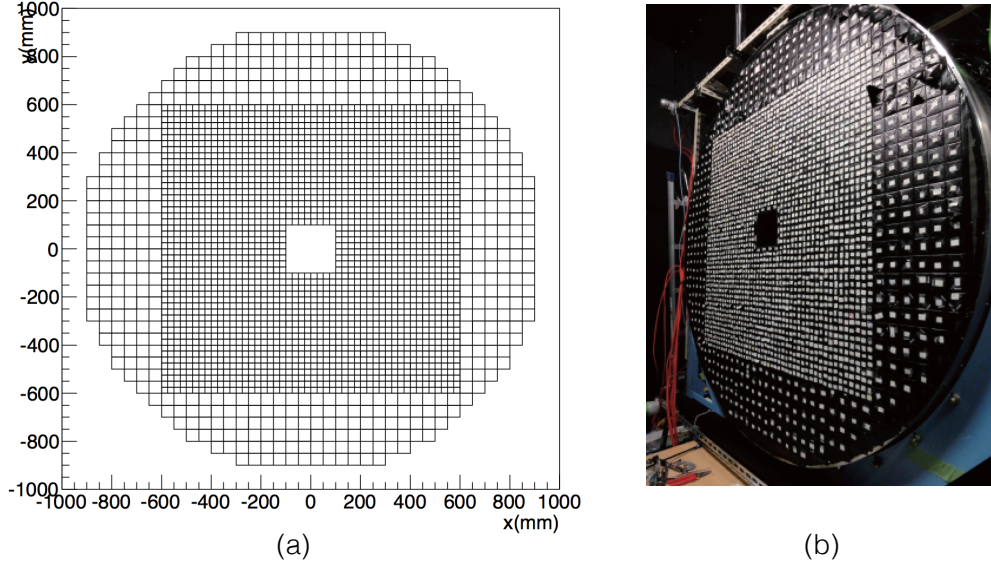
Figure 3.1: (a) Geometry of CsI Calorimeter viewed from upstream. (b) Picture of the CsI Calorimeter

The CsI crystals should have the capability to detect photons with energy from 1 MeV to 1 GeV. The designed output of the PMT is 1V/GeV pulse height. To achieve the sensitivity of detecting 1 MeV photon, a noise level of 180 μV_{rms} is required for the amplifier design.

To monitor the stability of the gain, light from a PIN photo diode is fed to each crystal through fibers. The wavelength of the laser output is 360nm-400nm, and the laser shines at the frequency of 1 Hz throughout the experimental period. Under vacuum, circuit discharges occur for some channels, so a lower voltage was applied, or turned off. In the data taking, 2 CsI channels were turned off.
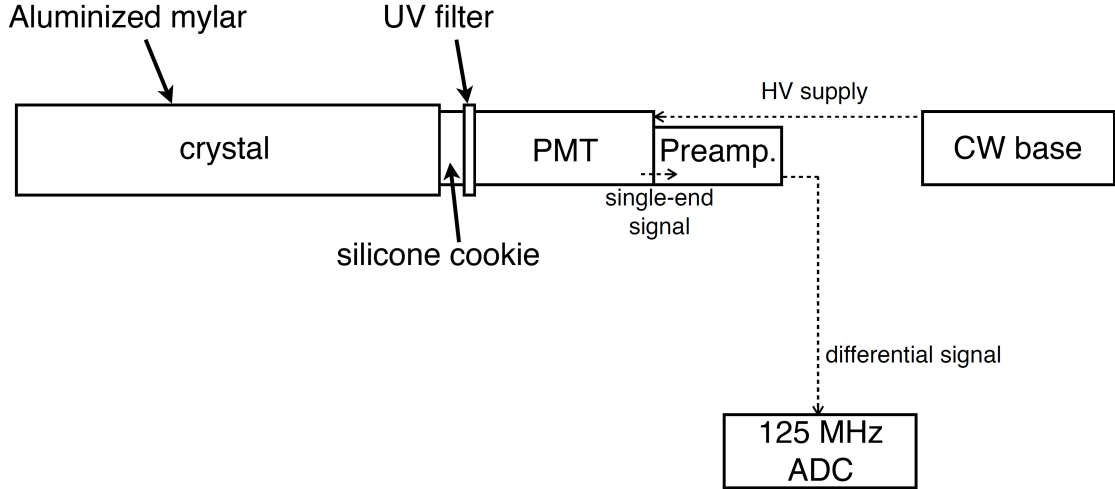
Figure 3.2: The structure of each CsI crystal.

3.2.2 Calibration Methods

3.2.2.1 Cosmic Ray Calibration Method

Cosmic ray calibration is to roughly tune the high voltages applied to the PMT amplifier to obtain a constant energy scale between energy and ADC counts. Cosmic ray muons interact with CsI crystals as MIPs (minimum ionizing particle) with dE/dx loss, i.e. the energy deposit in the crystal array is proportional to the length of track passing through. For CsI, this number is 5.63 MeV/cm for the typical cosmic ray muon energy. In each event, the cosmic ray track is reconstructed using the Hough transformation as described in thesis (*Takahiko* (2014)). Combined with z information obtained from MB z information, the length of the track is determined, and the deposited energy is also determined. Figure 3.3.(a) shows a typical cosmic ray event. A Landau function, which describes the energy deposit of a charged particle passing through matter is used to fit the energy deposit peak. For each channel, the Landau distribution peak ADC count / MIP energy is tuned to be as close as possible. To trigger the calibration data, plastic scintillators are located on top and at the bottom of the CsI arrays, and scintillation coincidence is triggered. Figure 3.3.(b)

shows the ADC count distribution of all the crystals after PMT gains are adjusted. A 2% deviation is achieved for all the channels.
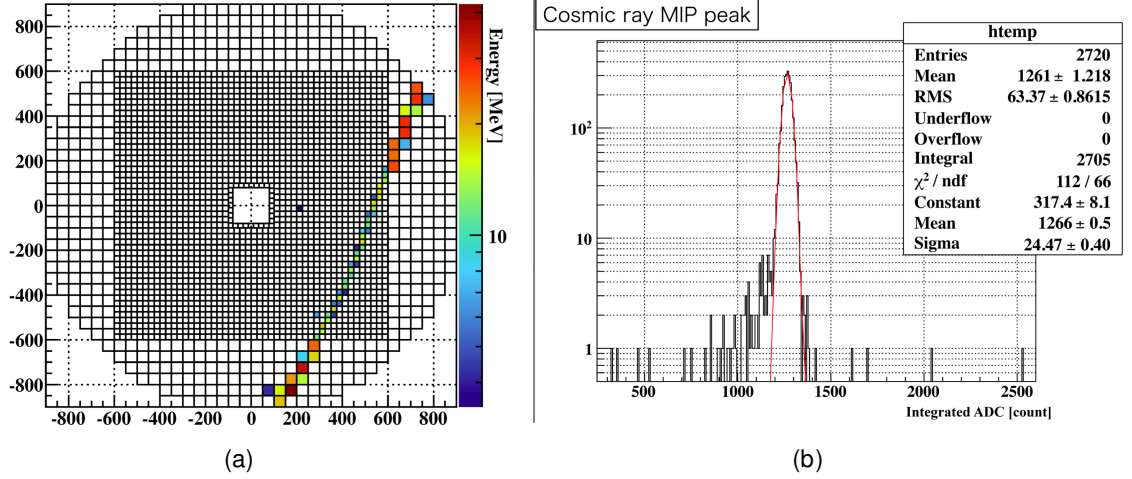
Figure 3.3: (a) Example of cosmic ray event. (b) The ADC count distribution for all the CsI channels after cosmic ray calibration.

3.2.2.2 $K_L^0 \to \pi^0\pi^0\pi^0$ Calibration Method

$3\pi^0$ calibration method is used to determine the relative energy scales between CsI modules. The known information is the position and energy of each cluster noted as x_i, y_i, Z_{CsI} and E_i. Assuming that the K_L transverse momentum is 0, there are three unknowns in the reconstruction process: the decay vertex of K_L. In the first step, the 6 photons are paired up using the least χ^2 method described in section 2.4, after which the decay vertex v_x, v_y, v_z is known as well as the momenta for π^0.

$$p_{i,\gamma}^{\mu} = E_i \frac{(1, x_i - v_x, y_i - v_y, z_{CsI} - v_z)}{\sqrt{(x_i - v_x)^2 + (y_i - v_y)^2 + (z_{CsI} - v_z)^2}} \tag{3.1}$$
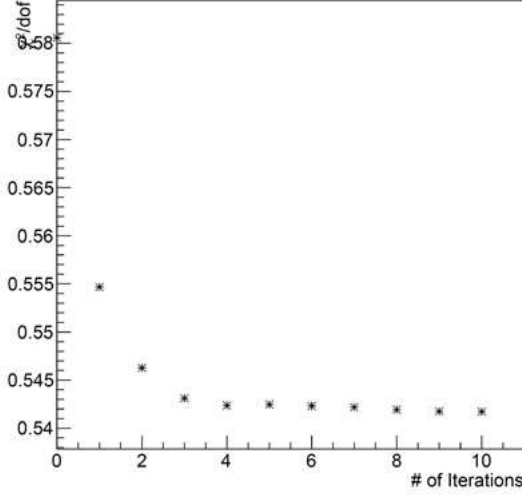
Figure 3.4: The $\chi^2/d.o.f$ vs the number of iterations in one $K_L^0 \rightarrow \pi^0\pi^0\pi^0$ application.

At the same time, there are 6 kinematic constrains:

$$(p_1 + p_2)^\mu (p_1 + p_2)_\mu = -M_{\pi^0}^2 (for \ each \ \pi^0) \tag{3.2a}$$

$$(\Sigma p_i)^\mu (\Sigma p_i)_\mu = -M_{K_L^0}^2 \tag{3.2b}$$

$$\Sigma x_i \cdot E_i = v_x \cdot \Sigma E_i \tag{3.2c}$$

If we set one cluster's energy unknown, we will have 6 constraints and 4 unknowns, which will give 2 degrees of freedom. We build a Lagrange multiplier and $\chi^2(Sumida$ (2008)) and find the energy for the photon by minimize the χ^2. Figure 3.4 shows the convergence of χ^2/ndf evolved with number of iterations.

3.2.2.3   Al Target Calibration

Al Target run is a special run for CsI calibration and for neutron study. In Al target run, two aluminum plates are inserted into the beam line as shown in Figure 3.5. K_L^0s and neutrons interact with the plate and secondary π^0s generate 2 photons in the CsI. Since the decay position is fixed, this event is kinematically unique and the π^0 mass can be reconstructed. After the Al target calibration, the overall scale of calibration factors are determined. Figure 3.6 shows the π^0 mass distribution after

37
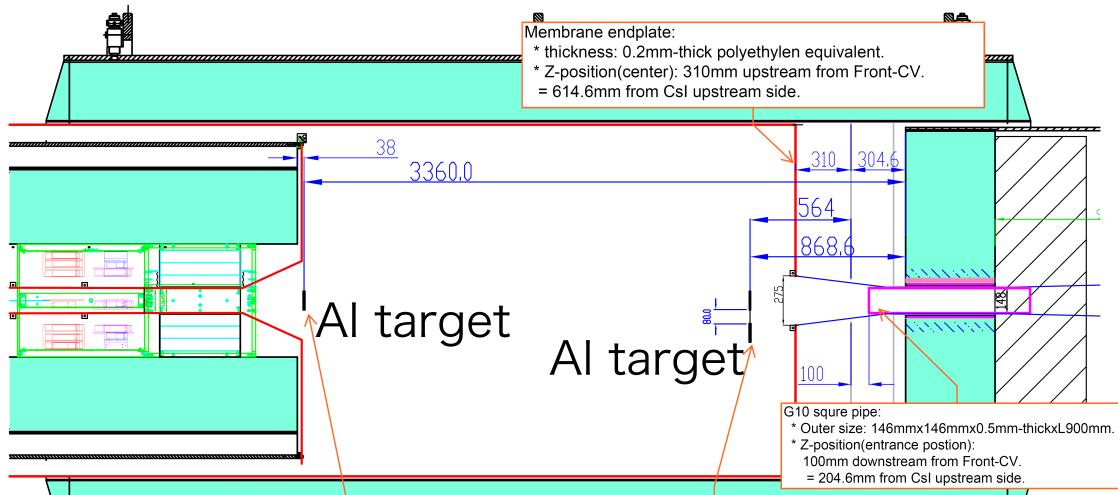
Figure 3.5: The appuratus of Aluminum target run.

the calibration.

3.3 Main Barrel

3.3.1 Structure and Efficiency Curve

Main Barrel is the photon veto covering the side of barrel region. It is comprised of layers of lead and scintillator plates. The requirement of MB design is 10^{-4} inefficiency for energy deposit larger than 100 MeV to suppress $K_L^0 \to \pi^0 \pi^0$ decay mode. Figure 3.8 shows the structure of the MB modules. Figure 3.7 shows the efficiency curve of the MB and the upgraded KOTO MB.

3.3.2 Calibration Method

3.3.2.1 Cosmic Ray

The goal of the calibration involves two topics: 1) adjust the timing between different modules; 2) Unify the energy of each module. Here, the method will be briefly described.

The MB is a two-end readout. The PMTs at both ends of the barrel module have
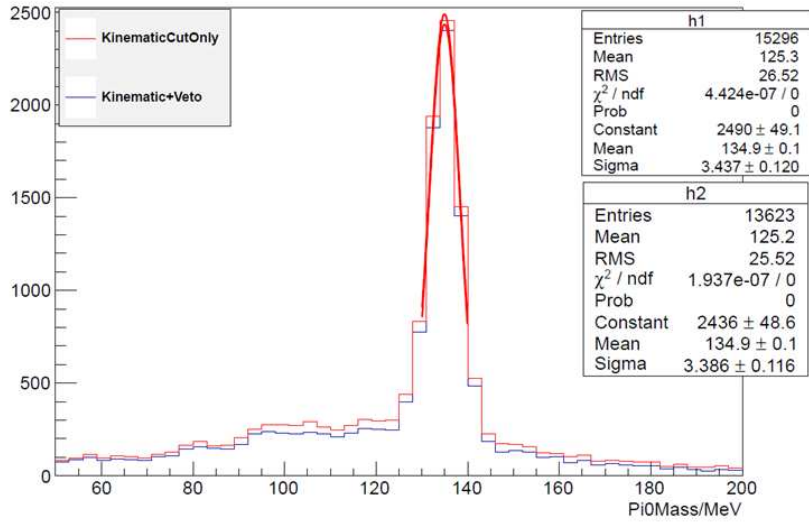
Figure 3.6: The mass distribution of the reconstructed π^0 in Al Target run after calibration.
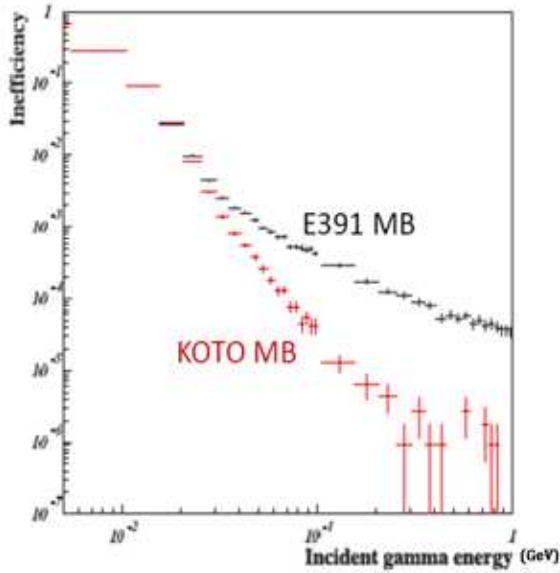
Figure 3.7: The efficiency curve of the E391 MB and the new proposed MB.
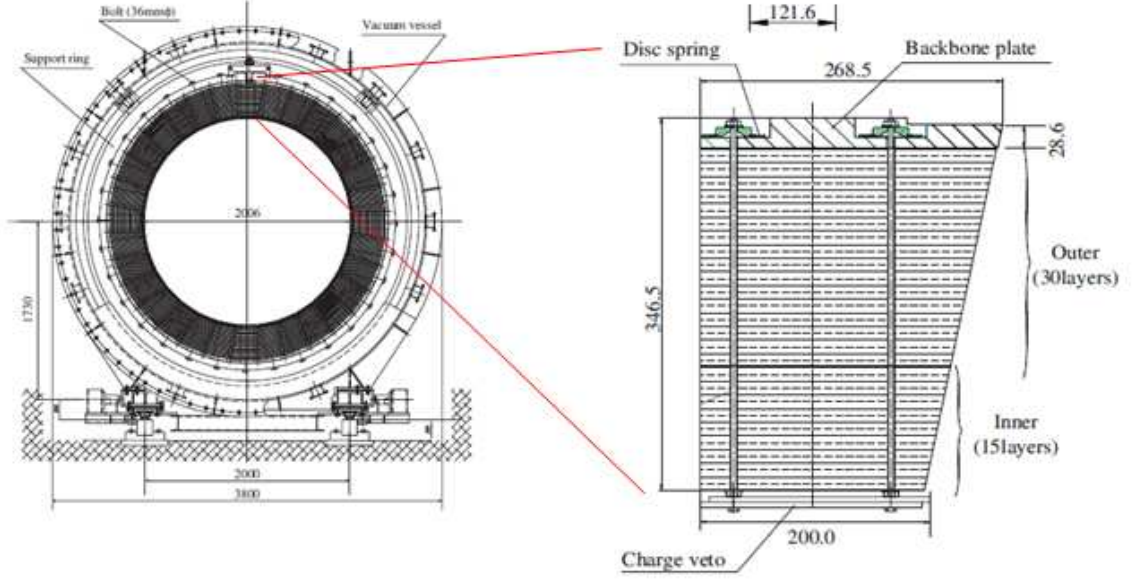
Figure 3.8: Main Barrel structure

different time delays from PMT or front-end cables labeled as δt_i, and there are 2*N free parameters, where N is the number of MB modules(96). From the measured time labeled as t_i, we know the real time is

$$
\begin{aligned}
t_i &= t_i + (L/2 + z)/v + \delta t_i (upstream\ channels) \\
&= t_i + (L/2 - z)/v + \delta t_i (downstream\ channels)
\end{aligned}
\tag{3.3}
$$

In the above equation, L is the length of MB module, and the zero point of z is the center of modules, and v represents the speed of light in scintillator. This problem can be factorized into two problems:

1) Timing adjustment within one module

$$
t_i^{upstream} - t_j^{downstream} = t_i - t_j + \delta t_i - \delta t_j + 2z/v
\tag{3.4}
$$

2) Timing adjustment between modules

$$
t_i^{upstream} + t_j^{downstream} = t_i + t_j + \delta t_i + \delta t_j + L/v
\tag{3.5}
$$

40
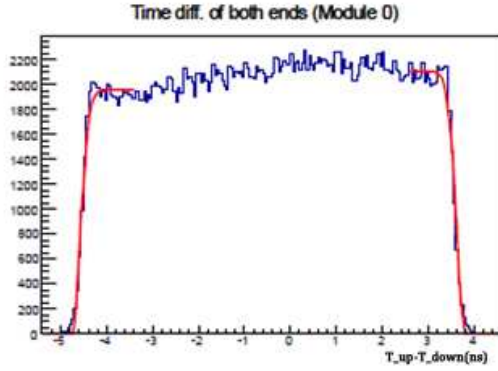
Figure 3.9: The time differences betwen the two ends of one MB module

The benefit of timing calibration is that the z position can be found.

Step 1: Timing alignment within one module.

The first step is to adjust the timing between the two ends. An example of good timing adjustment is that a MIP signal hitting the center of the module generate two signals which reads the same timing. To do that, all the tracks are collected, and the timing differences are collected for both ends. Some examples are shown in Figure 3.9. The distribution should have two well defined edges with a fixed length corresponding the the length of the module. The center of the distribution is identified from fitting the two edges, and the deviation of the center time from 0 is labeled as the inner module timing calibration factor. The fitting functions are:

$$a_0 \left(1 - e^{-\frac{1}{2}\left(\left(\frac{max(x,a_1)-a_1}{a_2} \right)^2 \right)} \right) \tag{3.6}$$

In the above equation, a_0 is related to the number of events, a_1 is the position of edge, and a_2 is the slope of the transition edge.

Step 2: Timing alignment between modules

After the timing within a single module is calibrated, we need the define the timing of the module from the timing of the two ends which is calculated as the average of the two ends. To align the time between different modules, we select tracks which hit diagonal modules. After TOF correction, the difference between each pair of the

41
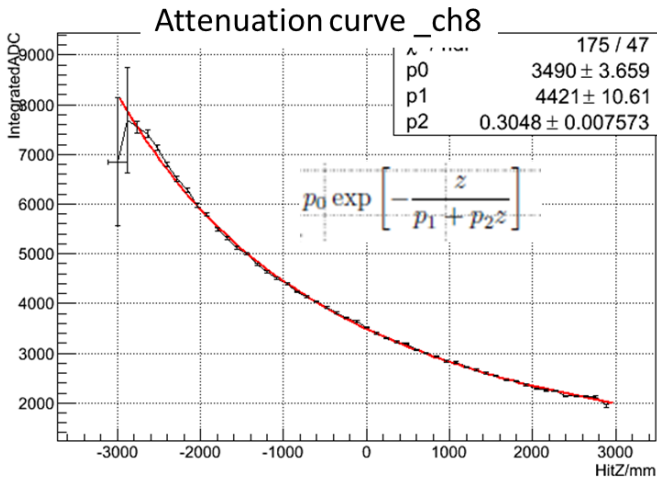
Figure 3.10: The attenuation curve for Module ID 8.

modules are filled in an array. Each element of the array is determined by fitting all the events with gaussian, and a gaussian mean is used. Side modules have small statistics, so a χ^2 cut is used to make sure the gaussian fit is OK.

After all the array elements are determined, a χ^2 method is used to determine the best Δt. The χ^2 is defined as

$$\chi^2 = \sum_{i,j} \frac{T_{ij} + \delta\delta t_i - \delta\delta t_j}{Terror_{ij}} \tag{3.7}$$

In the above equation, $T_{ij} = T_j - T_i$, with $T_i = t_i^{upstream} + t_i^{downstream}$, and $\delta\delta t_i = \delta t_i^{upstream} + \delta t_i^{downstream}$, and $Terror_{ij}$ is the associated error of T_{ij}.

Step 3: Calibrate energy

The light is attenuated as it propagates along the module before collected by the PMTs following the rule:

$$E(z) = E_0 e^{-\frac{z}{\lambda + \alpha z}} \tag{3.8}$$

The attenuation curve is ploted in Figure 3.10. Fitting with Equation 3.8 obtains the attenuation constants $\lambda = 4421 \pm 11mm$, and $\alpha = 0.30 \pm 0.01$.

Figure 3.11 shows the result of the MB calibration for the 2013 May run.
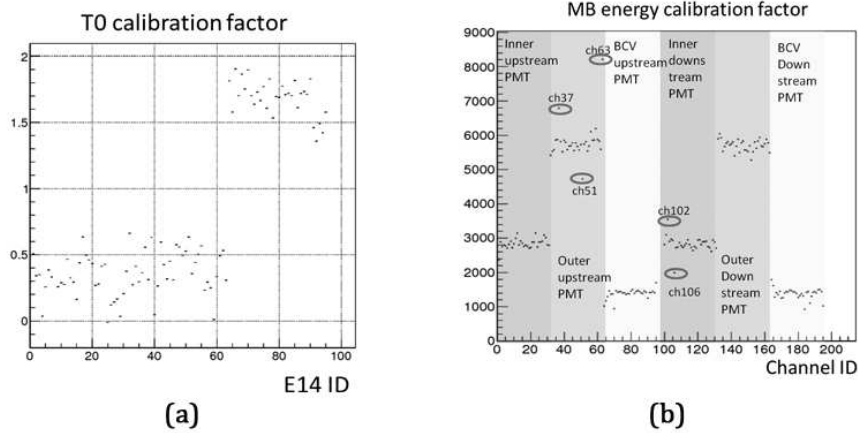
Figure 3.11: (a) The t0 calibration factor. (b) The energy calibration factor.

3.4 Charged Veto

3.4.1 Structure

The CV is a two-layered structure in front of CsI. The module layout is shown in Figure 3.12.(a). The thickness is 3 mm and width is 70mm. Wavelength shifting fibers are used to increase the light yield. The scintillation light is detected by multi-pixel photon counter (MPPC), which is silicon APD arrays with average light yield of 19 p.e. per 100 keV.

3.4.2 Inefficiency

Inefficiency comes from fiber grooves in the CV modules. For π^-, it has an additional inefficiency source due to charge exchange with nuclei($\pi^- p \rightarrow \pi^0 n$). The inefficiency of the CV is measured to be less than $2.5 \times 10^{-5}(Naito$ (2014)).
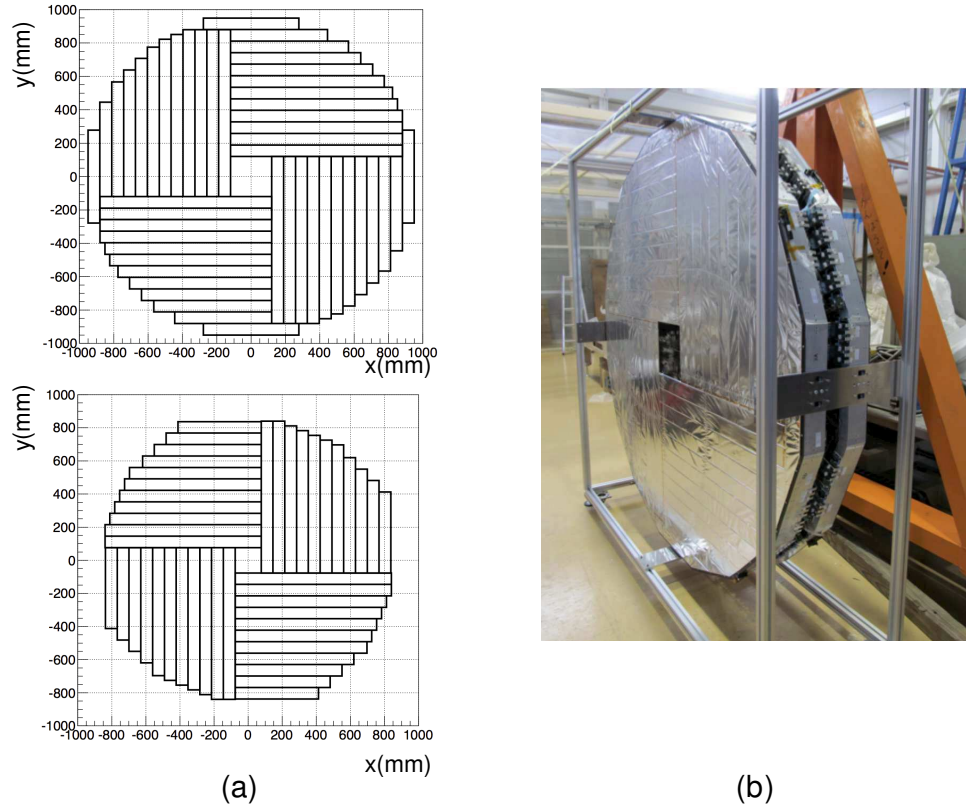
Figure 3.12: (a) The sketch of CV module layout of the front CV (top) and rear CV(botton). (b) A picture of the assembled CV detector

3.5 Other Detectors

3.5.1 Front Barral

Front Barrel (FB) is the photon barrel detector upstream of the decay region. It has the same structure as MB with a different length and radius. There are 32 modules, and each has single end PMT read out.

3.5.2 Neutron Colar Counter (NCC)

The largest background in E391a is halo neutrons hitting the detector material close to the beam hole. NCC is used both for vetoing such event and for measuring the neutron background. It has 56 undoped CsI crystals sectioned in the z direction, which
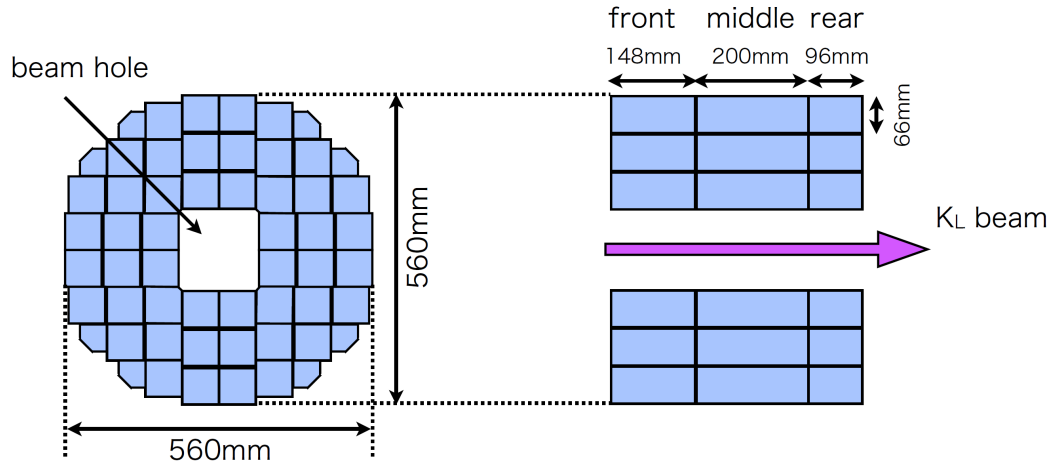
Figure 3.13: The geometry of NCC detector.

faciliates distinguishing γ, which deposits most of its energy in the front section and neutrons, which penetrates further and deposits energy in middle and rear sections.

3.5.3 CC0X

CC03-CC06 are collar counters completing hermecity on the downstream side(Figure 3.14). CC03 covers the innermost surfaces of the CsI beam hole to avoid photon energy leakage into the beam hole. CC04-CC06 locates downstream of CsI. All of these detectors are made of stacking CsI crystals and plastic scintillators.

3.5.4 Beam Hole Charged Veto (BHCV)

BHCV is the charge veto placed between CC06 and BHPV alligned with beamline. It's made of 8 3mm-thick plastic scintillator (Figure 3.15).

3.5.5 Beam Hole Photon Veto (BHPV)

BHPV is a set of 25(In the 2013 May run, only 11 were installed) modules aligned with the beam line in the most downstream section(*Maeda* (2014)). The goal of this detector is to detect photons from K_L^0 decay that travel through the beam hole region,
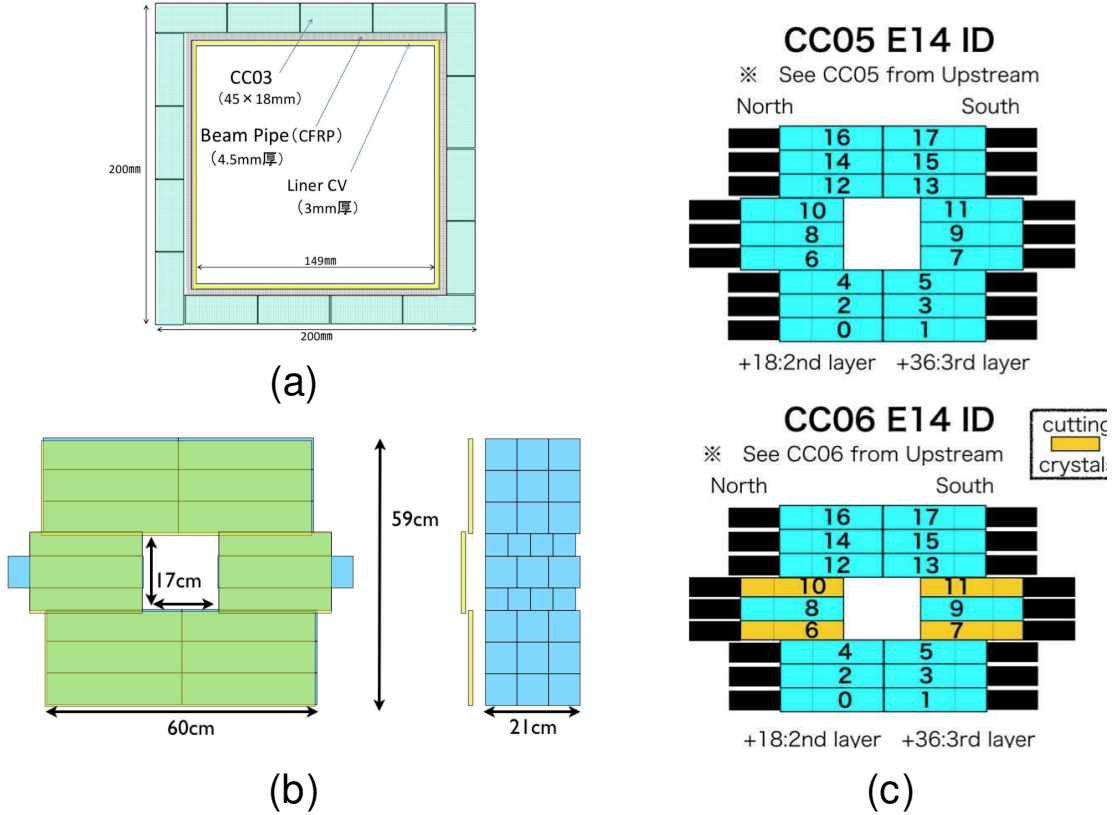
Figure 3.14: The geometries of collar counters. (a) CC03. (b) CC04. (c) CC05 and CC06

while remaining insensitive to kaons and neutrons. It is critical to remove $K_L^0 \to \pi^0\pi^0$ background when one γ with relatively small energy missed detection by Main Barrel due to the limited efficiency in small energy regions, and the other γ highly boosted and travels downstream the beam hole. The design value of BHPV inefficiency is 10^{-3} at 1GeV.

The design of the BHPV module is to improve high γ detection efficiency while avoid interactions with the neutral beam itself. The main contaminations are beam neutrons and γs, which are mostly of small kinematic energy. BHPV is a Cherenkov photon detector, and the neutral beam particles do not generate Cherenkov light.

To use BHPV as veto, a coincidence of larger than 3 consecutive modules having signals is required. This is to further distinguish beam neutron hits, which have
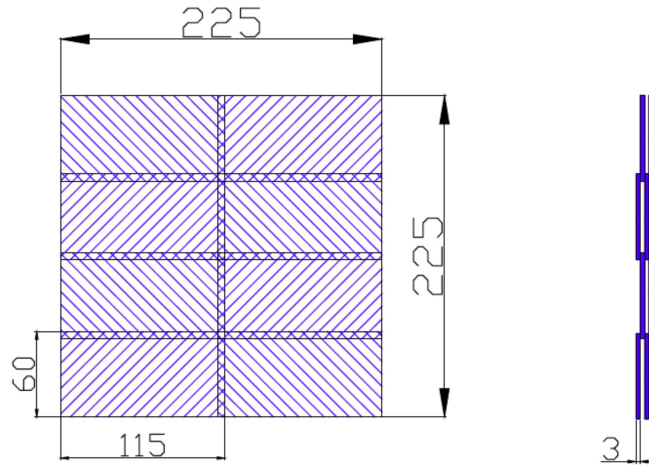
Figure 3.15: The geometry of BHCV.

isotropic shower, and beam low energy γs, whose radiation length is small.
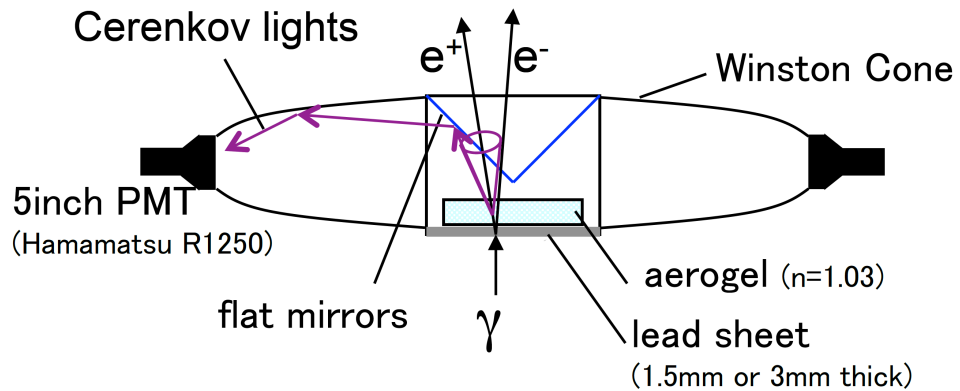
Figure 3.16: BHPV module structure.

3.6 Run Condition

The 2013 May data was collected over 100 hours of beam time with accumulated protons on target as 1.6×10^{18}. The beam terminated earlier than schedule with 1/5 of expected run time. It was due to a power supply problem of the slow extraction magnet, causing the beam to be extracted in a short time. The T1 target was partially evaporated resulting in release of radiative material.
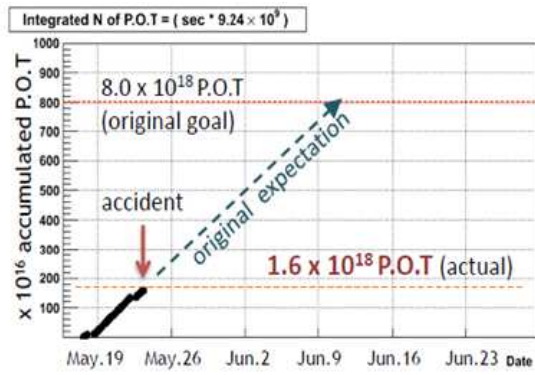
Figure 3.17: The accumulated protons on target for the 2013 May run

CHAPTER IV

Data Acquisition

4.1   Overview

The KOTO Data Acquisition (DAQ) system consists of a Analog-to-Digital Converter (ADC) based front-end and a three-layered trigger system, where level 1 (L1) and level 2 (L2) are hardware triggers and level 3 (L3) is based on software. The top-level design is shown in Figure. 4.1, and the diagram with more details on hardware layout is shown in Fig. 4.2.

The total number of detector channels is 3678. Table 4.1 shows the channel count for each detector. The ADC boards are housed in 17 VME crates, where each crate has a processor and a backplane for VME control. The MACTRIS board, which is the central control board, is located in the middle slot of the L1 Trigger crate, with all the 20 L1 trigger boards including the CsI trigger board and veto trigger board. The L2 boards along with the COE MACTRIS board are self-contained in the L2 trigger crate. The Ethernet output from each L2 board is fed into an Ethernet-fiber media converter, and is transported to the L3 PC cluster via a long fiber, where the fiber-Ethernet media converter translates back to Ethernet signal and enters the back-end network. The back-end network is based on a 48-port switch, where segments of the same event are routed to a targeted PC in the cluster. The L3 cluster is a 40-node 4 core cluster with 16 GB RAM and 2TB hard disk on each node.
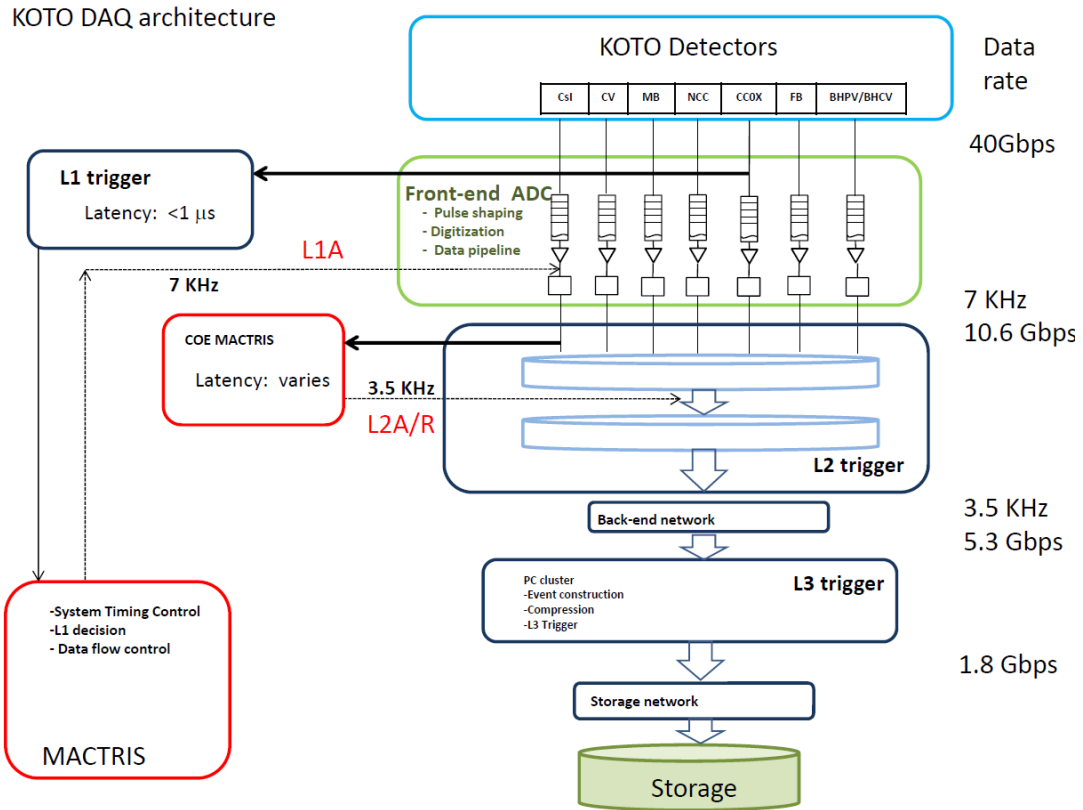
Figure 4.1: The top-level schematic design of the KOTO DAQ system.

The front-end 125MHz ADCs take the analog signals from the detectors, shape the pulses through a 10-pole filter and digitize the pulse. The ADC boards have 2 separate data I/O connection to the L1 and L2 boards. The digitized data is sent to L1 trigger system continuously. In the L1 trigger, a trigger decision (L1A) is made based on the deposited energy and timing of the CsI crystals and the veto detectors. Once trigger decision is made, the L1A signal is sent back to the ADC and the ADC will collect the 32 clocks before and after the L1A signal (64 clock sample window) and package it into a packet and send to L2.

The L1 system is to make fast trigger decisions with very little latency. There are 9 types of triggers for different purposes. Their definition of trigger conditions and
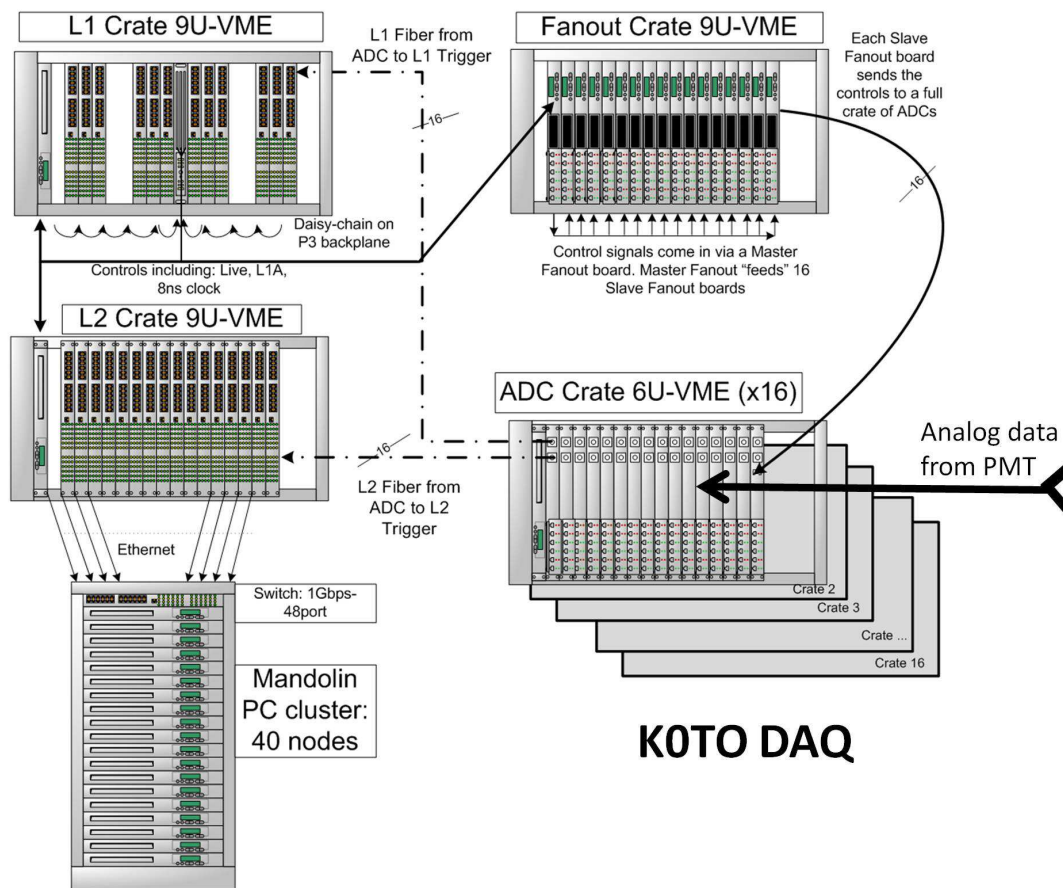
Figure 4.2: The top-level schematic design of the KOTO DAQ system with more cabling and hardware details.

rates of each trigger types are shown in Table 4.2. Some of the triggers are at high rate, and thus need to be pre-scaled to be able to be handled by the back-end. When each L1 accepted event is sent to L2, a L2 decision is made for each event based on the Center of Energy (CoE) to enhance large P_T events and if passed, those events will be temporarily stored in the memory on board, and sent the the L3 PC cluster for temporary storage. Long-term storage and analysis is performed in the KEK computer center (KEKCC), and the data is continuously transferred from J-PARC site to KEKCC via local network at the maximum speed of 2 Gbps.

Table 4.1: The DAQ channel counting and ADC module counting for each detector.

Detector	Number of Channels	ADC Module Count	
		125MHz	500MHz
CsI	2716	176	0
CV	184	12	0
MB + BCV	196	12	0
NCC	204	13	0
CC03	32	2	0
CC04	64	4	0
CC05	64	4	0
CC06	64	4	0
FB	32	2	0
OEV	44	3	0
LCV	1	1	0
BHCV	8	0	2
BHPV	24	0	6
Other(Cosmic, Laser)	48	3	0
Total	3678	236	9

4.2 Design Requirement

The DAQ design should meet the three requirements:

1) It should have good timing resolution to be able to distinguish between signal and accidental background at high beam intensity;

2) It should also have high throughput to reduce DAQ dead time and be capable of handling large amount of data;

3) It should have efficient in the selection of physics events.

For requirement 1), the beam intensity is high, so the accidental activities from the beamline is tremendous. To distinguish between a "real event" and an "accidental event", a tight cut based on timing is required. To achieve a good timing resolution, we need the whole pulse information. In E391a experiment, a TDC was used for timing measurement, which is not immune to beamline accidentals. If we have the pulse information, we can tell the accidental events or pile-up events by distinguishing multiple-pulse events.

Table 4.2: Trigger set. Alias: CsI Et: CsI Et > 5500 counts (550MeV); Veto: CV<8000 count (2 MIP), CBAR <2000 count (50 MeV), NCC< 5000 counts (100 MeV), CC03 <3000 (100 MeV); COE: CoE>165mm; RC (Region Counting): the number of regions with CsI Et >$100MeV$ is larger than 4.

Trigger Type	Trigger Condition	Prescale Factor	Scaled Trigger rate (Trigger/spill)	Comments
Physics	CsI Et && Veto && COE	1	6.4K	physics trigger
Normalization	CsI Et && Veto	30	0.74K	$3\pi^0$,$2\pi^0$,2γ events
Minimum Biased	CsI Et	300	0.62K	All K_L^0 decays
$3\pi^0$ Calibration	CsI Et && RC &&Veto	10	0.32K	$3\pi^0$ events
Cosmic I	OffSpill & NCC Et	1	32	Off spill cosmic ray events for NCC calibration
Cosmic II	OffSpill & OEV Et	1	42	Off spill cosmic ray events for OEV calibration
Cosmic I	OffSpill & CsI Et	2	84	Off spill cosmic ray events for CsI calibration
External I	clock ‖ laser	1	87	External clock and laser events
External II	Tmon	1	94	Target monitor trigger

For requirement 2), the current design has a few bottlenecks in terms of data throughput. Each ADC output has 2.5 Gbps data rate, and the total system's rate is 612.5 Gbps. The V2V bus in L2 (see Section 4.5.2) has a maximum rate of 32 Gbps. Each L2 has a 2 Gb on board memory for buffering on spill of data, which takes 16 Gbps data rate considering 16 L2 triggers and a 2s-on, 6s-off beam structure. And the Ethernet readout of L2 board limits to 16Gbps. The network connecting JPARC site and KEKCC has maximum speed of 2 Gbps. At each stage, the data reduction ratio should be optimized to avoid the bottleneck at that stage.

For requirement 3), an effective trigger should both be able to help reducing the throughput, and also enhance the $K_L \to \pi^0 \nu \bar{\nu}$ signal.

4.3 Front-end ADC

The analog signals from the PMTs of the CsI crystals, the MPPC of the CV modules and most other detectors are fed into ADC's one of the 16 inputs directly or through a 50Ω single-ended to 100 Ω differential converter.

There are two types of ADCs: most detectors use the 125MHz sampling rate 14-bit ADCs, and some beam hole detectors(BHCV and BHPV), which have high counting rates use 500MHz 12-bit ADCs.

In the 125MHz ADC, there is a 10-pole shaping filter before each ADC chip to shape the sharp pulse from PMT output, with very sharp dropping edge and a large tail, into a Gaussian-like shape as shown in Fig 4.4. The purpose of shaping is to filter out the high frequency component and achieve better timing resolution. The timing resolution of 125MHz ADC is 160 ps by fitting the 10 samples around the peak with Gaussian function.

The 14 bit 125 MHz ADC chip allows a dynamic range of 16.4 K counts to represent 1.6∼ 2 GeV energy range, so the bit representation of 1 MeV is 8 ∼10 ADC counts in pulse height. After the digitization, the data is processed in the FPGA chip

where data from the 16 inputs are synchronized. The data at this stage is forked with one branch starts to calculate the sum of the 16 channels, which is continuously sent out via the 2.5 Gbps optical link to L1 board. The other fork is pipelined and wait for the L1 decision.

As soon as one L1A trigger is made, the FPGA starts to assemble the event information by taking 32 samples before and after the trigger point. The width of the window is 64, which is trade-off between more accidental activities with larger window width, and less accurate pedestal estimation with smaller window width. The size of an event is 471 kB plus headers.
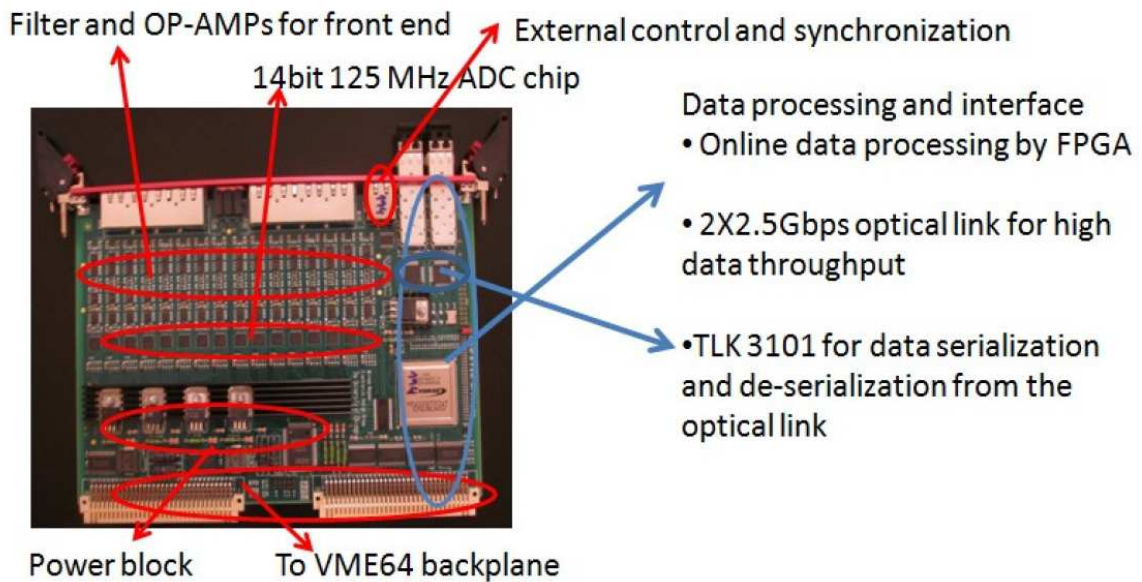
Figure 4.3: Picture of 125 MHz ADC board with the main function parts circled.

4.4 Level 1

4.4.1 Structure

L1 trigger needs to make Level 1 decision based on CsI energy and veto signals. As a result, the L1 trigger boards are programmed as *"CsI trigger boards"* and *"veto trigger boards"*. The hardware configuration is shown in Figure 4.5.
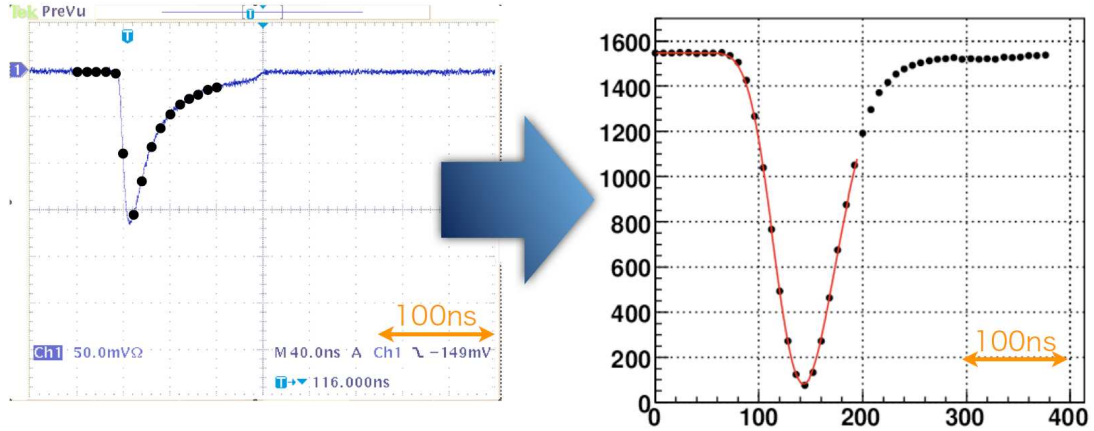
Figure 4.4: The pulse shaping of the 10-pole LC filter from the PMT output (left) to the Gaussian shape (right). The black dots show the sampling point.

For the "CsI trigger boards", the most common CsI trigger is to calculate the total energy (E_{total}) of all the CsI channels. To achieve this goal, all the "CsI trigger boards" need to communicate via the Daisy Chain in the backplane of the L1 crate. Each Daisy Chain has 24 bits communication between adjacent slots, i.e. the board in slot n should be able to fetch information from the Daisy chain output of the slot n-1. In this way, the partial total energy can be calculated using 18 out of the 24 Daisy chain bits. The MACTRIS board, which sits in the middle slot, will access the final summation from both the left and right Daisy chain. L1A will be made if CsI Et is larger than 5500 counts, corresponding to 550 MeV.

For the "veto trigger boards", we need to compare the total energy of each veto detector to a threshold and a single bit output indicating larger or smaller than is needed for making veto trigger. To accomplish this, 6 Daisy chain bits are reserved, each of which represents one veto detectors for L1 veto signal. Veto signal also needs to be made within a veto window, which are 4 clock cycles around the CsI Et peak.
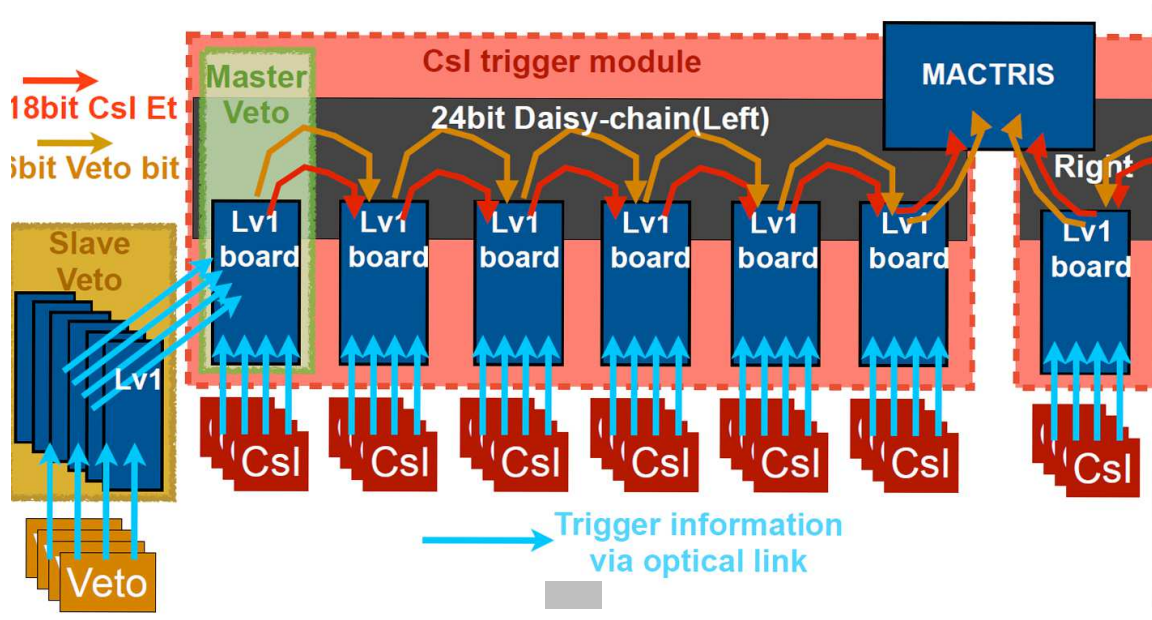
Figure 4.5: The left half of the Daisy chain structure of L1 trigger decision. The L1 triggers are programmed as "CsI trigger boards" and "veto trigger boards", and 6 bits of the 24-bit daisy chain is reserved for veto signals, and the other 18 are for the CsI Et calculation. Only the Master veto board is able to control the Daisy chain veto bits, and the other slave veto boards outputs to the Master veto vias optical fiber.

4.4.2 The Mactris Board and Fanout System

The Mactris board is the central controller board. It generates the system clock, makes the L1A decision and controls the data flow of the L2 system. Mactris board and ADC board communicate via the fanout system. Mactris generates three signals: LIVE, indicating the beam on and off; L1A, CLK and ADC can generate ERROR signal back to Mactris if needed. These four control signals are distributed to the ADC boards in a two-layered fanout way: the signal is sent to the a master fanout with 16 copies of output, and each master fanout output feeds into one slave fanout, having 16 output each, and in total generates 256 copies of control signals, each driving one ADC board.

4.5 Level 2

4.5.1 CoE Cut

L1 physics cuts are supposed to remove charged decay (80%) plus neutral decay with any photons missing the CsI fiducial region. The remaining trigger rate at 24 KW beam is reduced to 7 KHz, but is still beyond the throughput the back-end can handle. Nevertheless, there is a merit feature of background events passing L1 but not physically interesting: P_T in the final state should be small, as long as conservation of momentum is held and the P_T and radial span of the K_L beam is tailored to be small. The Center of Energy (CoE) radius, which can be mathematically represented as

$$CoE = \frac{\sqrt{(\sum_i x_i E_i)^2 + (\sum_i y_i E_i)^2}}{\sum_i E_i}, \tag{4.1}$$

of background events from $K_L \rightarrow \pi^0 \pi^0 \pi^0$ and $K_L \rightarrow \pi^0 \pi^0$ should also be small, the result of which is shown from MC study Fig.4.6 *Carruth* (2013)(Note that in this study, statistics is not normalized to the same POT). In the expression above, E_i is the energy deposit in crystal i, and x_i and y_i are the center coordination of the crystal i. It is easy to see that CoE radius is both correlated with P_T and Z_{decay}, but MC study (*Carruth* (2013)) show that due to the signal box in Z_{decay}, the signal loss due to CoE cuts off the signal events with large Z_{decay} will be largely compensated by the Z_{decay} cut. as shown in Figure 4.7.

4.5.2 Structure

The Level 2 (L2) system comprises of one L2 master board (CoE Mactris) for handling the L2 trigger and 16 identically programmed L2 trigger boards.

Each L2 board has two FPGAs: the Virtex 5 (V5) as a master FPGA, and a Virtex 4 (V4) as a slave. A top-level schematic of the logic design is sketched in Figure. 4.8.
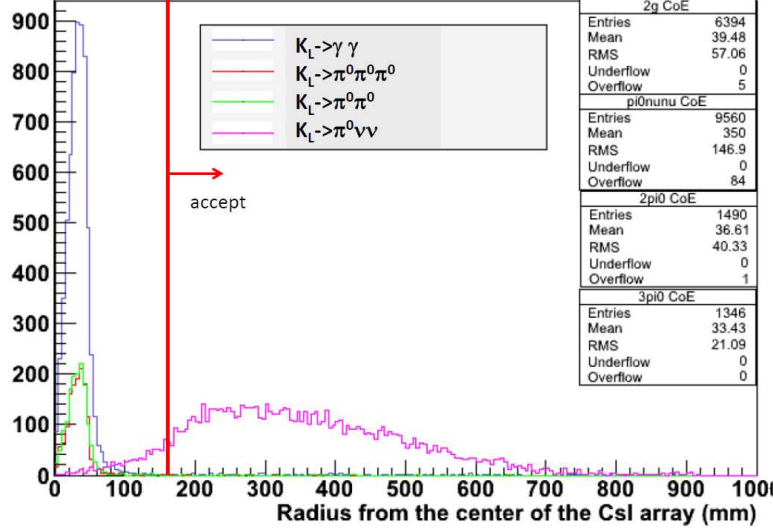
Figure 4.6: The CoE radius distribution of main neutral modes and the signal mode. Pure MC samples without accidental overlaid is used. More than 95% background reduction is expected if the veto inefficiency is not considered. Note that statistics is not normalized to the same POT.

The V5 handles the CoE calculation and processes the L2 trigger, whereas the V4 receives data accepted by L2 and sent from V5 via the 32-bit V2V data bus, wherein data is temporarily stored in an on-chip 2 Gb DDR2 memory, followed by a readout and packaging into an Ethernet packet.

Below is the data and control flow of the Virtex 5. For each of the 16 input fibers, the data from the ADC fiber inputs is first decoded by the TLK deserializer, and buffered in the $input\_FIFO$, the depth of which can hold up to 7 trigger simultaneously. A parallel path to the data stream is the CoE stream, where the COE_feeder modules decode the CoE partial sum information from the CoE headers appended to each packet, and calculate a local sum (include $\sum_i E_i$, $\sum_i x_i E_i$ and $\sum_i y_i E_i$) of the 256 channels on that trigger board. The total sum is sequentially calculated via the same Daisy-Chain protocol as the L1 trigger. A typical latency for a L2 trigger is 1.2

59
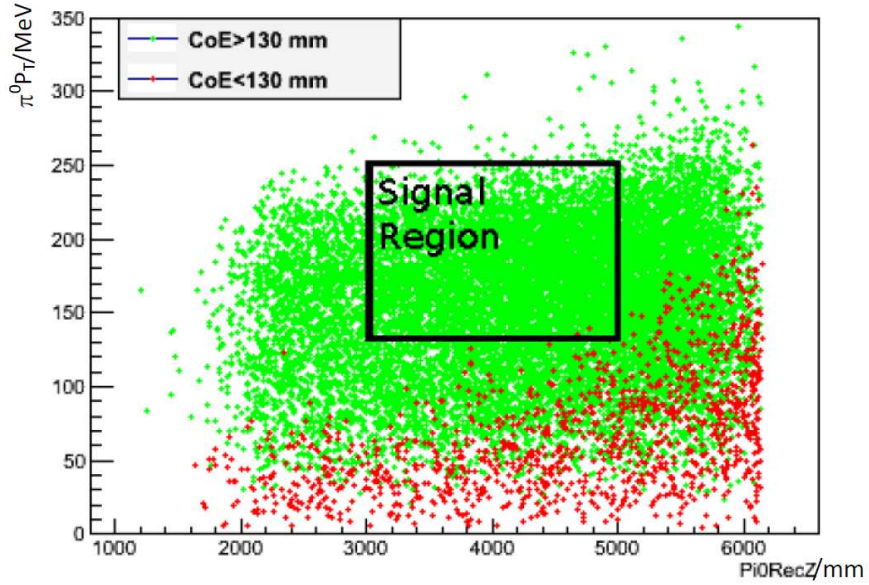
Figure 4.7: The P_T vs Z_{decay} scattering plot for MC signal events. The signal box is indicated by the square box. The signal loss ratio, i.e. red dots with CoE radius <130mm but still fall into the signal region, is on the order of 1/1000.

μs. While a L2 decision is being made, one packet is dumped into the $Queue\_FIFO$ and wait for the L2 decision. If L2 makes a reject decision, the $Queue\_FIFO$ will be cleared, which takes almost no latency. Otherwise, the data will be read out by the data multiplexer (MUX) and sent to V4. It's helpful to notice that the multiplexing with 16 channels in and 1 channel out is currently a bottleneck of the whole DAQ system. This back pressure will be propagated back to the $input\_FIFO$, and cause it to be full and data to be truncated. To prevent this situation from happening, a data flow simulation is implemented in the MACTRIS board to predict the data flow. Before the $input\_FIFO$ is full, the MACTRIS will stop issuing new L1A. The DAQ dead time introduced is 20%.

This paragraph will introduce how the V4 handles the buffering of data. There are two 2 Gb DDR2 memory chips on board, and the current buffering scheme is a double-buffer scheme, where for one spill, the data is written in one of the two memories, and the data written to the other memory from the previous spill is read out simultaneously, assembled by the Ethernet interface and sent out via the 1 Gbps Ethernet port. As a result of such design, the limit on the total amount of data per trigger board is 2 Gb. There are 16 L2 boards and the memory takes 2 seconds to fill, which gives the total throughput of 16 Gbps.
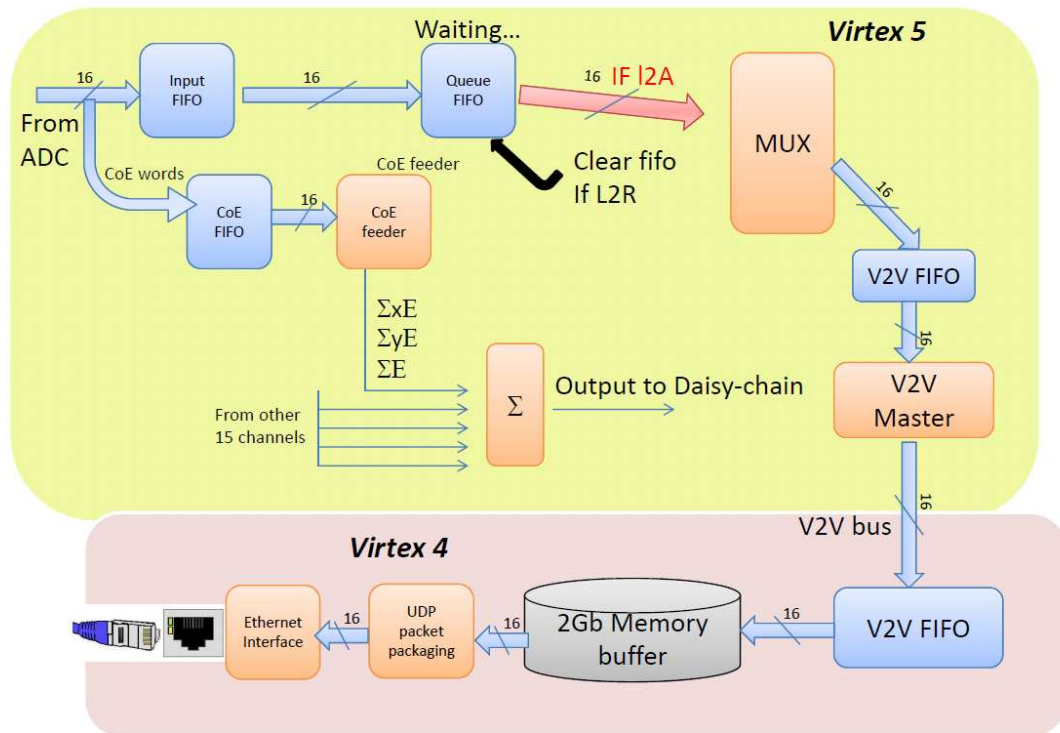
Figure 4.8: Top level firmware design for L2 trigger board.

4.5.3 Data Flow Control and Simulation

We have argued in the previous section that a data flow controller is needed to prevent in $Input\_FIFO$ in the L2 firmware from being full and data corrupted. The data flow controller is implemented in the MACTRIS board, and here's how the

simulation works. There's an internal counter, which is an estimate of how many triggers are in the $Input\_FIFO$. This counter will increase by 1 when a new L1A is issued, and decrease by 1 when all the boards report one trigger read out from the $Input\_FIFO$. This simulation is on the conservative side, since the latency between L1A issued and data dumped into the $Input\_FIFO$ is not considered. In this consideration, the introduced DAQ dead time is 20%, i.e. 20% of the time, the L1 trigger is idle.

To improve the DAQ dead time, a C-code simulation is done considering different factors of improvement. In this simulation, L1 requests (L1req) are generated with random gap between each other but with a fixed average rate: L1req rate (L1req rate = 14 KHz is the value for 24 KW beam intensity). When a L1req is generated, the number of triggers in the $Input\_FIFO$ is increased by one, and the number will decrease by one when a time dilation of Δt finishes. The Δt depends on the time it takes for the multiplexing of 16-in-1-out data readout(Δt depends partially on the memory refreshing rate, and a good estimation of a realistic value is 16.7×10^3 clock + freshing time). When the number is larger than maximum depth of the $Input\_FIFO$ N (N=7 is the current situation), L1A is disabled. L1req signals, only when they are not rejected because L1A disabled, is a legitimate L1A. The ratio of $L1A/L1req$ is the quantity the simulation aims to maximize. L2 reduction ratio (L2A ratio) is also an important factor here, since if the L2R is issued, the data will be removed immediately, and the data multiplexing back pressure is 0 for a L2R events.

Below is the result of different factors affecting the L1A/L1req:

- N

  Figure. 4.9.a shows the dependence of L1A/L1req ratio on L1req rate by varying the $Input\_FIFO$ size N. In reality, N = 7 (green dots), and realistic values for Δt = 17000 clock cycles and L2A ratio $\approx$ 33% is used. The star is the data with L1req rate=14 KHz and L1A/L1req ratio = 0.8. It's noted that simulated

L1A/L1req ratio is 10% better than real situation, in that the L1req's time micro-structure is not simulated, where in reality, triggers are more clustered in time. The conclusion from this simulation indicates that an improvement of <5% is expected when trigger rates is >50 KHz even the size of buffer is increased by a factor of 2.7. Enlightened by this fact, possible improvements can be made by using newer versions of FPGA with more resources.

- L2A ratio

  Figure. 4.9.b indicates that when L2A ratio is <40% and L1req rate around 20 kHz and 60kHz, the effect on L1A/L1req ratio is almost linear. To improve the situation from this end, new algorithm or L2 cuts is needed on top of the current CoE cut. One possible proposal is to implement hardware clustering algorithm at this stage. But current L2 hardware design has limited communication between different boards, so a hardware upgrade is necessary to achieve this goal.

- Δt

  Figure. 4.9.c tells us that decreasing the amount of time for multiplexing data out of the $Input\_FIFO$ changes significantly the L1A/L1req ratio in the L1req rate range from 20kHz up to 100kHz. The only way to decrease the Δt is to use compression before the data enters the L2 stage. This fact guides us to apply compression in ADC as a short term DAQ upgrade step.

4.5.4 Performance

The physics trigger takes a CoE cut at 165mm, which has an average reduction factor of 3. The online CoE has some deviation from real CoE:

- 1) the energy is not calibrated between channels.

- 2) Due to online calculation only takes integers, the x and y position of each crystal is represented as unit of the size of small crystals. So any position variation smaller than the unit size is not considered.

- 3) The fluctuation of pedestals will affect the calculation of energy, since the pedestal of each channels is sampled once per run.

- 4) To calculate the energy sum, a sum over the 64 samples is calculated. In such case, any accidental activities will change the CoE.

Of the 4 factors shown above, factor 2) has a negligible effect. And 1) and 3) in total will bring a total signal loss of 3%, which is calculate from Figure. 4.10, the number of events offline accepted (red) but online falls below the threshold. Factor 4) has the biggest influence. In Figure. 4.11, the accepted ratio (CoE accepted events / Total events) is ploted for signal and background events, where signal has a 10% accidental loss, and background contamination is at 1% level.

4.6 DAQ Back-end and Level 3

4.6.1 Software Architecture

Level 3 is software based. Each L2 board does the packaging of event information into Ethernet UDP packets. Each packet contains part of the information of one event from 16 channels. In the PC side, they need to receive the information of a whole event so as to do event builder. And the IP address of a single event is targeted to one PC. A switch routes the packets to correct host. There are four steps the L3 needs to do: packet capture and event builder, L3 cut, compression, storage to hard disk.

The L3 software is a multi-threaded design. For each event, it needs to be captured by the custom software from the Network Interface Controller (NIC) card, filtered and

moved to local memory; fit into an event based on the header information. Once one event is built, it needs to be analyzed to generate L3A/R based on some advanced cuts. Compression needs to be done to save hard drive space. And finally, the data needs to be moved from RAM to hard drive. The 1st three steps needs to be done in RAM due to its high access speed.

If done in series, the backlog from data transfer from RAM to hard disk will cause dead time which will propagate back to cause latency at the packet capture step. The system memory for the NIC is limited and doesn't allow for large latency. Packet loss will occur if the system memory overflows. Due to such reason, parallel processing is required, and the multi-threading is the easiest solution. There are four independent threads performing each of the four tasks. The timing sequence of the multi-threading system is presented Fig 4.12.

The "capture thread" uses the pcap library based on udp whose advantage over tcp is that its speed, but it doesn't have bidirectional communication to guarantee that all packets are received. But we will show later that by optimizing the software architecture, we could be able to handle the packet loss rate at a manageable level.

The "compression thread" will apply a lossless compression to the binary raw data. The lossless compression uses the following algorithm. For each channel, a waveform will be either pedestal fluctuation in most cases, and a pulse whenever there's signal. The pedestal level is high around 300∼500 counts. So most of the information is actually storing the pedestals. In this compression algorithm, the minimun energy within the 64 samples are found. And find the range of the pulse and find the minimal integer n such that $peakHeight < 2^n$, which means the waveform can be compressed to be n-bit. The compression ratio is

$$compression\ ratio = \frac{3 + nSample \times n/(8bits/byte)}{2bytes/sample \times nSample} \approx \frac{n}{16} \qquad (4.2)$$

for 64 samples. Figure 4.13 shows the compression ratio of all the channels for a typical event. For most channels which have only pedestal fluctuation (width 3 counts say) falls mostly into a 3-bit and 4-bit representation. Channels with real pulse or CV channels, which have single photoelectron noise peak, often contributes to the tail.

The *cut thread* is currently not applied, but is reserved for additional L3 cuts. Some ready-to-use cuts are the cluster number cut.

The *store thread* is to move the data from RAM to hard disk, which is the slowest thread.

At the beginning of each spill, all the threads toggle to process a specific piece of the RAM. The total amount of RAM needed for each thread is 140MB, which corresponds to the maximum amount of data stored in the L2 board.

4.6.2   Performance

In the physics data taking, 29 L3 nodes are used for data capture, which is limited by the number of ports of the back-end switch. Each node has 4 CPUs and 16 GB of memory. After compression, the total data throughput is 1.7 Gbps. The L3 packet loss rate is controlled with 0.18% of spills having 20% or more packet loss as shown in Figure. 4.14.

4.7   DAQ Upgrade

4.7.1   System Expansion

With an increase number of total DAQ channels with new detectors, more channels using 500MHz readout, the total number of ADCs, L1 and L2 trigger boards increasing, and possible a new L1.5 trigger expose the current DAQ design to a limit.

In the current fanout system, the master fanout has 16 outputs, which limits the maximum number of ADC crates to be 16, assuming each output can drive one slave

fanout and one ADC crate. In face of that, new master fanout board is needed to increase the output port to 32 to allow for a larger system.

As to the trigger side, the L1 is currently using all the 20 slots, if new veto detectors are needed to make the L1 decision, an extra crate is needed to house the extra veto detectors. This situation requires a better capacity of distributing the control signals from MACTRIS to multiple crates, which is currently only limited to 2 crates. A new MACTRIS design should have expanded capability of communication . Another requirement is that the temporary buffer size needs to be extended such that more trigger information can be readout for future capability. Besides, new MACTRIS should have its own data stream with Ethernet output so that the trigger board data can be transferred and stored in PC independent of the other data stream.

4.7.2 Compression

We've shown in the previous section that if we apply data compression in ADC, the L2 $Input\_FIFO$ full introduced DAQ dead time can be greatly improved. The current proposal is to pursue this direction by applying lossless compression using the algorithm identical to the current L2 algorithm. A core difficulty is that the CoE calculation requires a strict synchronization in between data coming out of the ADC boards, the case of which will be broken if different channels have different lengths of data. Also, the data flow control becomes more complicated, and should be limited by the worst case scenario, so the gain needs to be studied before further pursuing.

4.7.3 L2 Upgrade

To achieve the goal of having bigger reduction ratio in L2, a more powerful L2 cut should be considered, one of the most promising option being a hardware clustering cut. The RCE (Reconfigurable Cluster Element) provides an opportunity to achieve this goal. It has a full-mesh backplane with 10 GB inter-board speed. Multiple RCE

boards are re-configurable, and the back board also gives flexible I/O to the rest of DAQ system.
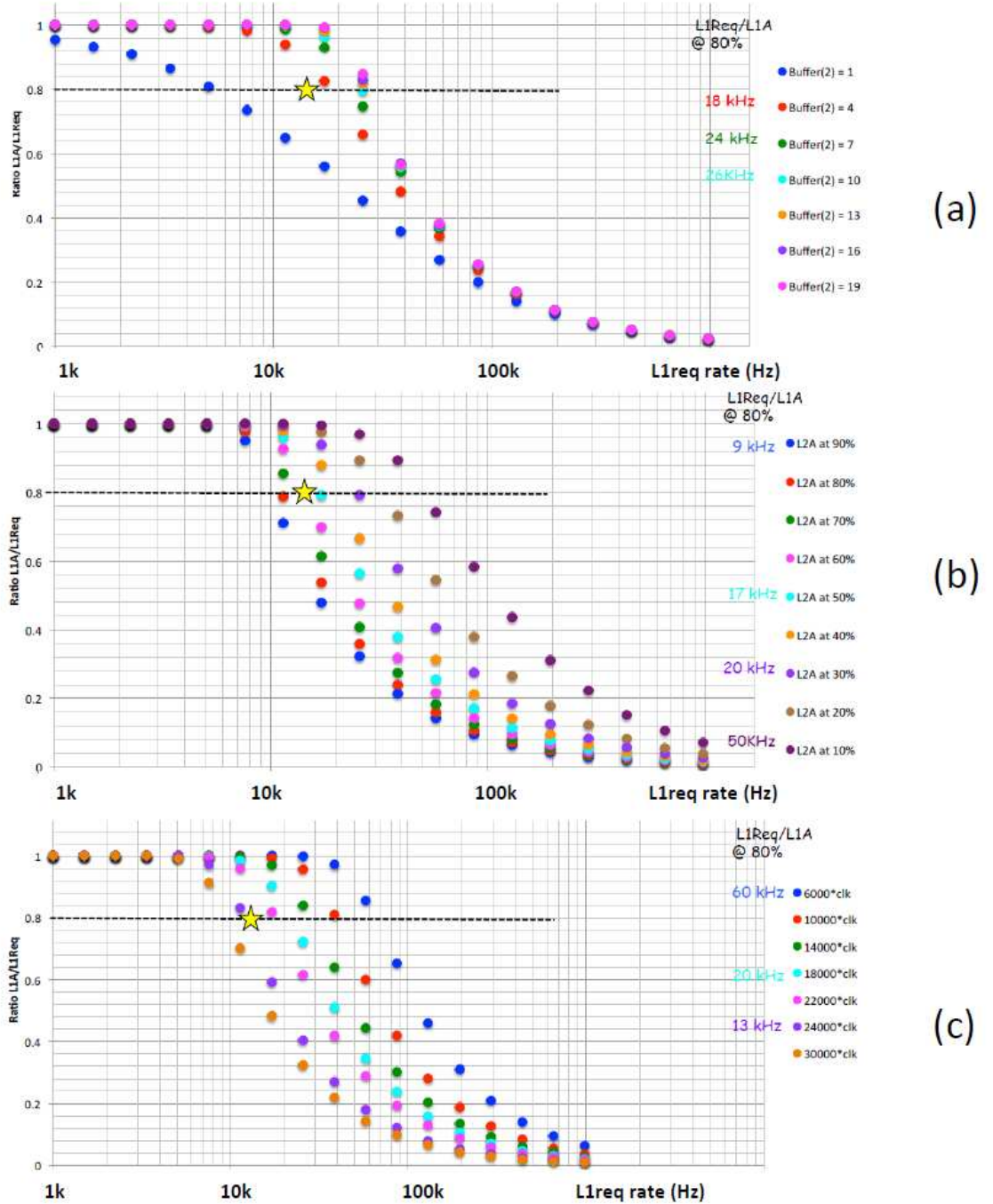
Figure 4.9: L2 data flow simulation using the model described in the text. The L1A/L1req ratio is plotted with respect to L1req rate. The star in each plot shows the realistic L1req rate and L1A/L1req ratio. a) Change the buffer size N (real value=7). b) Change the L2A ratio. c) Change the Δt.

69
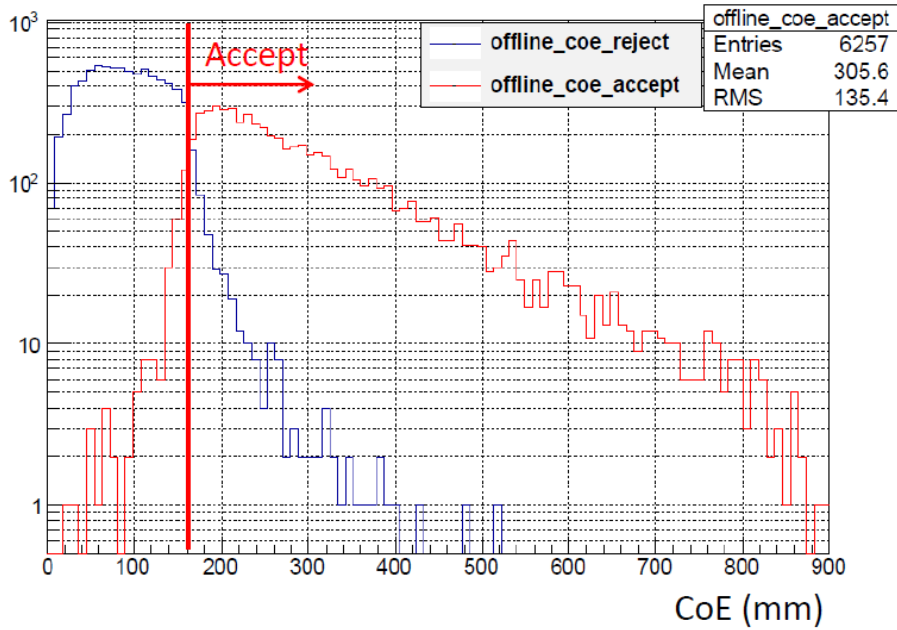
Figure 4.10: The online CoE distribution of offline calculated CoE <threshold (blue), and the offline calculated CoE >threshold (red). The red events under the threshold estimate the signal loss.
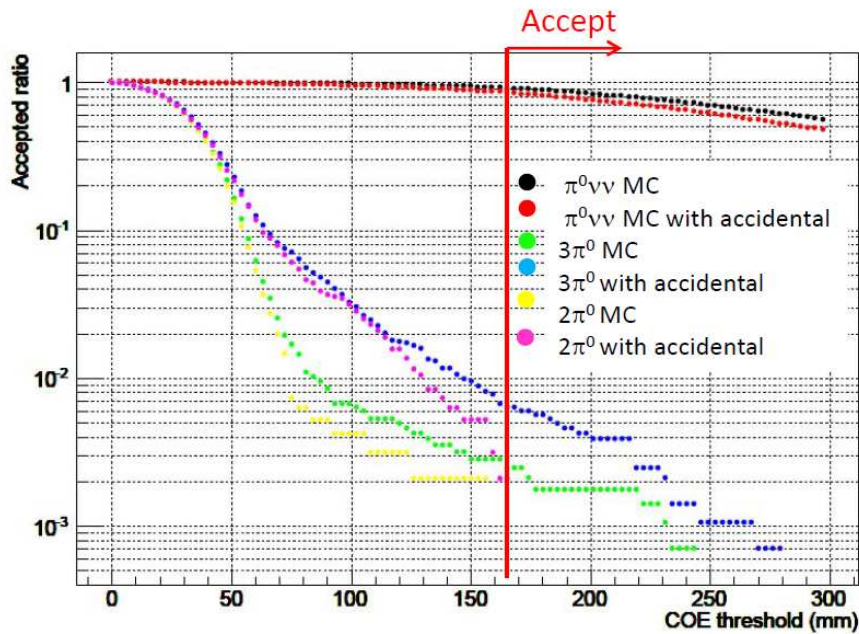
Figure 4.11: CoE Accidental Loss. Accepted ratio (ratio of number of CoE accepted events over total number of events) with respect to CoE threshold. Both pure MC samples and MC samples with accidental overlaid are presented.

70
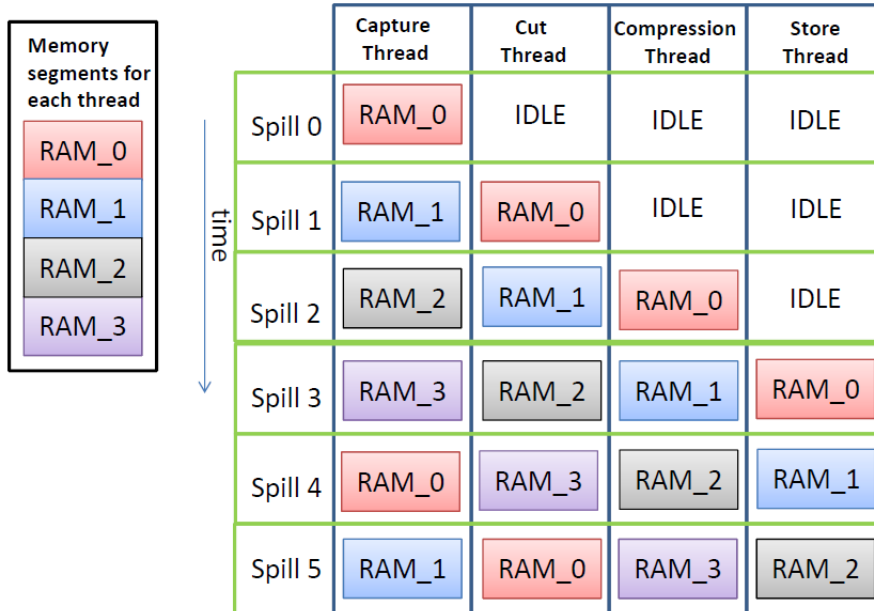
Figure 4.12: The time sequence of memory segments and multi-threads.
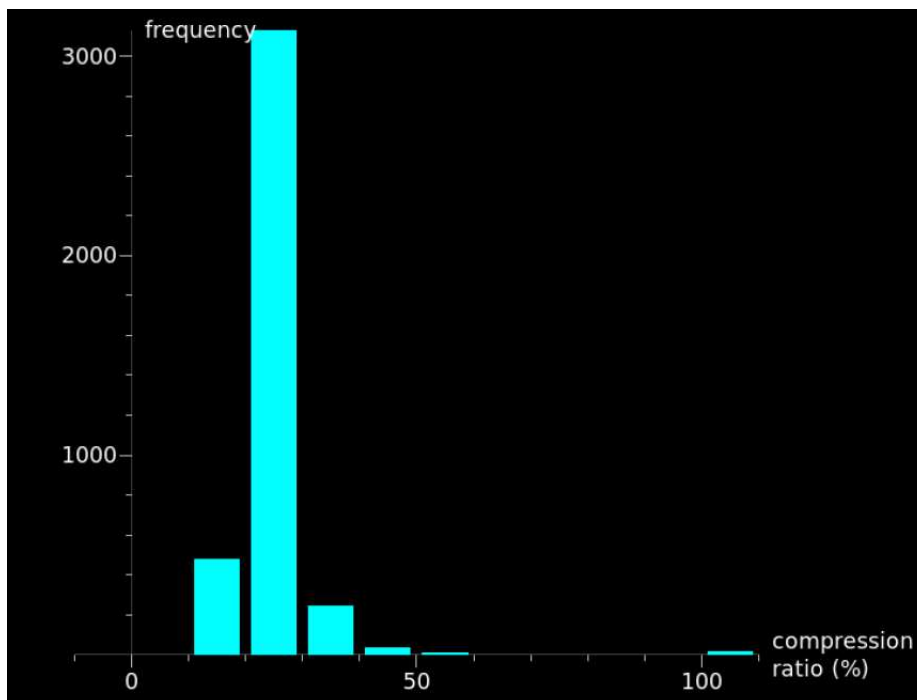
Figure 4.13: The compression ratio for all the channels in a typical event. Most channels which have pedestal fluctuation can be compressed into 4-bit representation(25% compression ratio). The average compression ratio is 30%

71
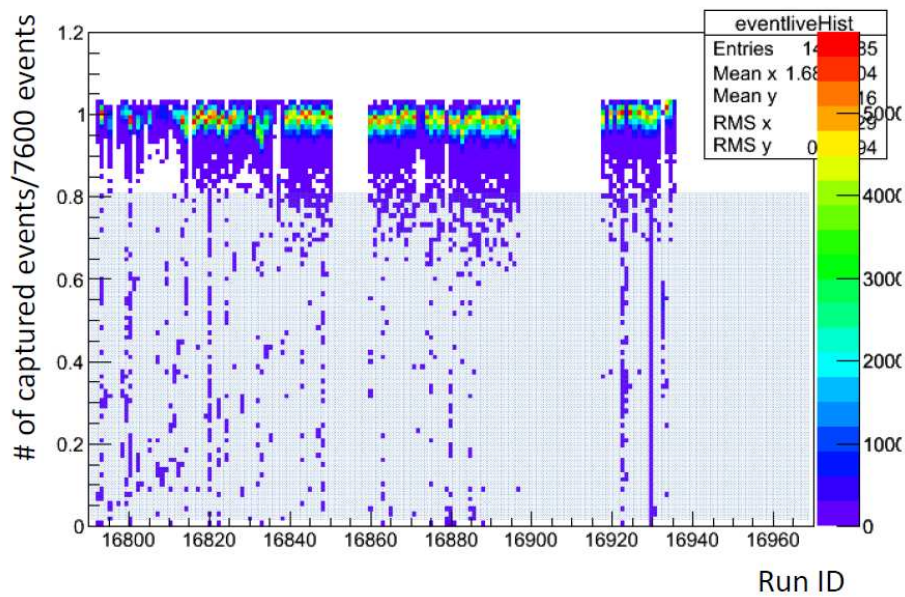
Figure 4.14: The ratio of number of L3 captured events over average maximum number of triggers (7600) for each spill in terms of time for all the physics runs. The portion of spills with with >80% packet loss is 1.8%.

CHAPTER V

Monte Carlo

5.1 Overview

We use the Monte Carlo simulation method to

1. Estimate the sources of background.

2. Measure the acceptances of each normalization modes in K_L^0 yield measurement.

Therefore, it's critical that we can reproduce the data from Monte Carlo, and understand the source of any differences. In such sense, having a more realistic Monte Carlo will reduce the systematic errors.

The K_L^0 decay Monte Carlo is based on Geant4 (*Agostinelli et al.* (2003)) library, and the beam neutron simulation is based on Geant3 (*Brun et al.* (1987)) and FLUKA(*Bhlen et al.* (2014) and *Ferrari et al.* (2005)). The idea of the Monte Carlo simulation is as follows. Each primary beam particle is generated with the pre-known spectrum (see section 5.2). Spacetime is discretized into steps and at each step, the fate of the particle is determined by ambient material and physics, where the probability of each physics state is computed and a random number is made according to probability distribution. This process repeats itself until the energy of the particle goes below the cut off energy, decays or travels outside the space the simulation is designed.

The energy scale of the interested process is around GeV and smaller, so the low energy physics packages are used like QGSP_BERT, which handles hadrons below 10 GeV. For neutron interactions, FTF_BIC package is used. There are different levels of simulations: the fast simulation will treat the detector as a non-responsive detector, and each particle will be stopped when its trajectary intersects with the surface of the detector, when the hit position, timing and energy are recorded. This type of simulation is fast and is mainly used to estimate the counting rate of each detector. On the other hand, in a full simulation, the detectors are responsive, and detailed interaction between the particles and detector materials are calculated. Each track, like the e^-, e^+ and γ in a electromagnetic shower are recorded as a collection, and the energy deposit can be later calculated after each of the tracks is corrected by detector response (Section 5.3).

5.2 Beam Line Simulation

5.2.1 K_L^0 Beam Simulation

The K_L^0s are generated 20 m downstream of the production target. The K_L^0 spectrum (including spatial distribution and the momentum and angle spectrum) is an input to the simulation, and was measured during a beam survey test($Koji$ (2012)).

The momentum distribution is shown in Figure. 5.1, and it's modeled by an asymmetric Gaussian as

$$\frac{dN}{dp} = N_0 exp\left[-\frac{(p-\mu)^2}{2\sigma^2}\right] \tag{5.1}$$

$$\sigma = \sigma_0(1 - (A + S \times p)(p - \mu)) \tag{5.2}$$

where N_0 is an arbitrary scale factor, μ is the mean of the distribution, σ_0 is the standard deviation at μ, and A and S are higher order asymmetry parameters. A fitting with data shows a measurement of these parameters as Table. 5.1.

74
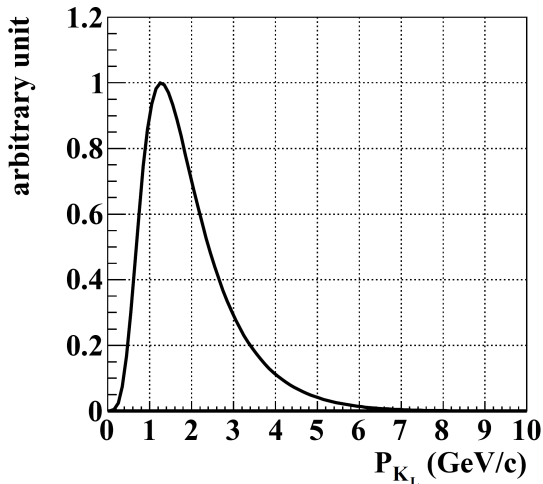
Figure 5.1: The momentum distribution used for modeling K_L^0 beam.

Table 5.1: The measured parameters of the beam profile in Equation. 5.1.

μ	1.41991 GeV
σ_0	0.810237 GeV
A	-0.301413
S	0.017092

The positions of the K_L^0 beam is generated by having a uniformly generated profile at the target position ($x = \pm 9.1mm$ and $y = \pm 1mm$) followed by making a projection onto the position where the K_L^0 beam is generated. The angle of the K_L^0 beam is also uniformly generated within the allowed range defined by the positions of the collimators (see *Takahiko* (2014)). There is an overall beam position shift in the transverse position to reflect the shift of the collimators during the experiments. The final beam position is $x = +6.2\,mm, y = +1.98\,mm$.

5.2.2 Neutron Beam Simulation

The biggest background of the E391a experiment is from the halo neutron interacting with the detectors close to the beam hole and generating π^0 and η, which have signal-like final state. To estimate this source of the background, a halo neutron beam simulation is necessary. The neutron simulation can be verified from NCC signals and from the Al target run.

5.3 Detector Response

5.3.1 CsI Calorimeter

The CsI crystals have energy resolution expressed as

$$\sigma_E/E = a/\sqrt{E} \oplus b \oplus c/E. \tag{5.3}$$

where $\oplus$ means adding in quadrature. The first stochastic term contains statistics-related fluctuations like the intrinsic shower fluctuations, photoelectrons statistics and dead material at the front of the calorimeter. The second constant term is from detector non-uniformity and calibration uncertainty. The third term is the electronics noise, and is independent of energy. The third term is negligible in the design of the experiment. For the two types of crystals, the designed energy resolution is quoted:

$$\sigma_E/E = 0.2\%/\sqrt{E} \oplus 0.45\% \tag{5.4}$$

Iwai (2012) for the small crystals and

$$\sigma_E/E = 0.4\%/\sqrt{E} \oplus 0.8\% \tag{5.5}$$

Sumida (2008) for the big crystals.

In the Monte Carlo, some effects which contribute to the energy resolution of the CsI crystals are not taken into account in the native simulation code, but will be manually applied as detector response. For the CsI, the following corrections to the energy and timing are applied.

- Light Yield Non-uniformity along the length of the crystal.

  Cerenkov shower generated at different depths of the crystal will have different energy deposit at the PMT at the end of the crystal due to propagation loss
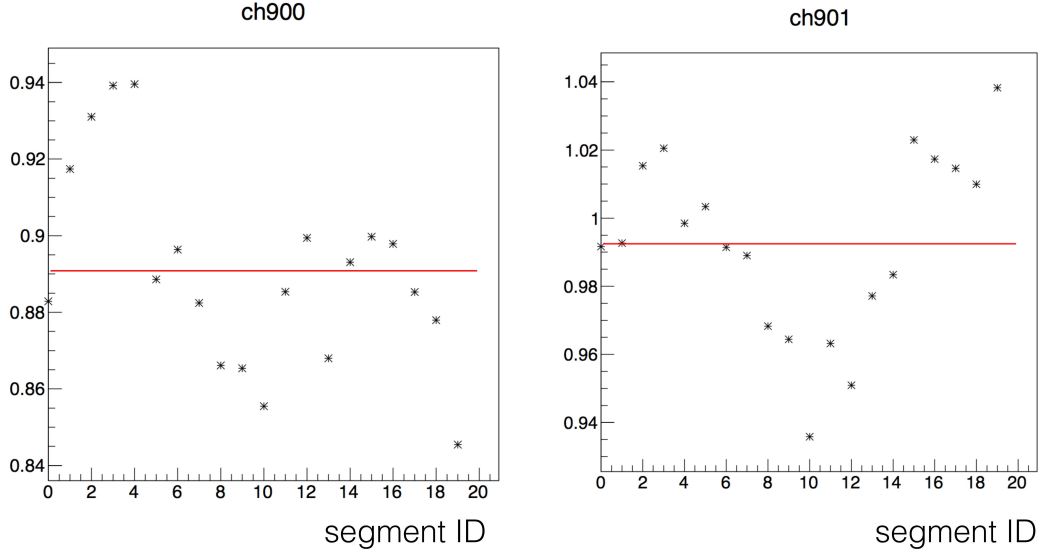
Figure 5.2: The light yield distribution along the length of some sample CsI crystals. Segment ID is small when moving towards the upstream.

and the wrapping of the crystals. To simulate this effect, a study of the non-uniformity was done to measure the relative light yield w.r.t length. In the study, a ^{137}Cs radiation source, which emits 662 KeV photons is placed at different z positions with 25mm interval, and the light yield is measured at each point. Fig. 5.2 shows some example of the measured result.

In the MC simulation, a collection of electromagnetic shower tracks are collected, and for each track, its energy is linearly corrected using the values of energy and track z position.

$$e(ch, z) = \frac{ly(ch, z)}{\Sigma_z ly(ch, z)/nSegments} * e \tag{5.6}$$

with ly(ch,z) the template light yield of each crystal with id ch, and position z. nSegments is the number of segments for each crystal, which is 20. After non-uniformity correction, different tracks are grouped according to their timing and position information, and electromagnetic shower can be reconstructed.

- Photo-electron statistics

  The actual CsI crystal light yield is different from the design value. From Chapter 3.2.1 , the silicone cookie, situated between the end the CsI crystal and the photo-cathode of the PMT, was used to enhance the transmission in the UV region. During the vacuum test, however, the Ethernet cables outgassed an organic solvent, which was deposited on the silicone cookie, and the transmission spectrum is decreased in the UV region. As a result, the effective light yield is reduced. To solve this issue, another type of cable (LINDY cable) is used after being baked to minimize the out-gas. But at the same time, the light yield needs to be re-evaluated and tuned under the vacuum situation .

  The overall light yield is tuned by maximizing the agreement of different kinematic distributions between MC and data. The final value is 9 photo-electrons. After the light yield is determined, the number of photo-electrons generated at the PMT follows the Poisson statistics with mean at the value of the measured value.

- Pedestal fluctuation

  The pedestals from the ADC noise is measured channel by channel, and is added to the simulated energy. A typical width of the ADC pedestal is ± 3 counts.

- Energy-calibration introduced inaccuracy.

  As shown in section 3.2.2.2, the $3\pi^0$ calibration method is performed to adjust the relative energy scale of the CsI crystals. But this method has intrinsic imperfection. For crystals close to the edges, including crystals around beam hole, around the outer layer of the array, and around dead CsI channels and unstable channels, the energy of the electromagnetic shower is easily leaked, and the recorded energy is smaller. The $3\pi^0$ calibration, on the other hand, will be able to recover the original energy, and therefore have a larger calibration
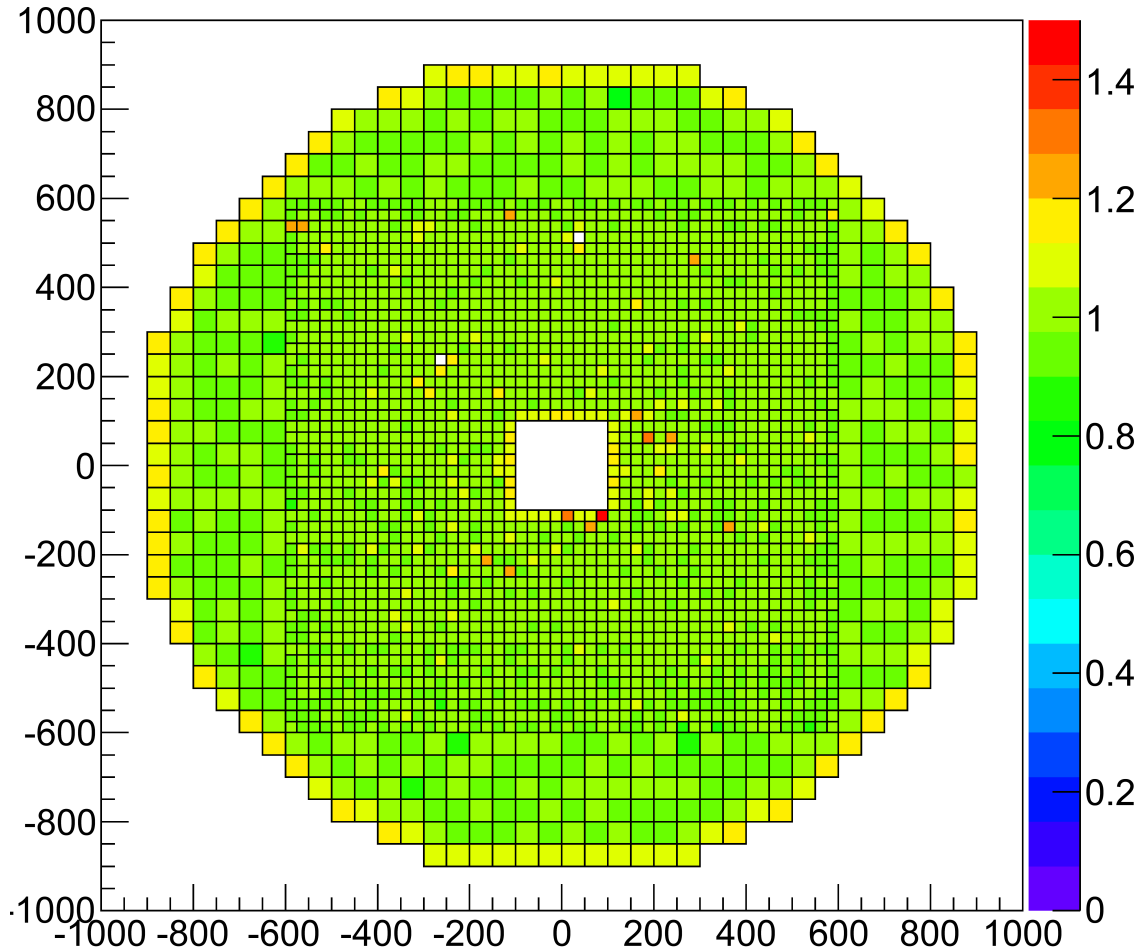
Figure 5.3: The miscalibration factors used for the 2013 May run data.

constant for these edge crystals. To show this effect, the same calibration process is applied to MC data, and the edge crystals will have similar enhancement of their calibration constant, which will reproduce data. Figure, 5.3 shows the map of the correction constants for the 2013 May run.

- Cherenkov light propagation delay.

5.3.2 Charged Veto Detector Response

In the MC, the following effects are studied.

- The non-uniformity of light yield along the length of each module is measured,

79

and accordingly, each track, depending on its hit position, has its deposit energy linearly corrected using this non-uniformity template.

- photo-statistics correction using Piossion functions.

- Ground noise simulating the ADC pedestal is added.

- Two-end readout is simulated by sharing the energy and timing.

5.3.3 Main Barrel Detector Response

Because the MB modules are long, the propagation energy attenuation and time delay are not negligible. To simulate this effect, the additional response is included. Depend on the hit z position, the energy deposit in the PMT is

$$E_{upstream} = e \times exp\left[-\frac{z - z_{upstream}}{a(z - z_{upstream}) + b}\right] \tag{5.7}$$

$$E_{downstream} = e \times exp\left[-\frac{z_{downstream} - z}{-a(z_{downstream} - z) + b}\right] \tag{5.8}$$

5.4 Simulate Beam Accidentals

When the beam power increases, the pileup effects meaning more than one event is captured in one sample window become more significant. In such cases, the way we determine energy and timing will be wrong. The most significant effect will be the cases where one accidental hit arrives slightly earlier than the triggered events, and the waveform of one veto detector is deformed and the timing shifts earlier and falls outside the veto window and therefore the event not vetoed.

To simulate this effect, we take a special type of of trigger named Tmon trigger, (i.e. Target Monitor trigger) to record a snapshot of the whole detector system at random times. Tmon trigger is triggered on the target monitor energy deposit, which is a scintillator close to the target, and reflects any activity in the production target.

Table 5.2: Monte Carlo sample statistics for each decay mode. The POT for data is 1.43×10^{18}.

Decay Mode	Branching Ratio	Number of files	P.O.T	Ratio to normalization trigger
$K_L^0 \to \pi^0\pi^0\pi^0$	19.52%	5000	1.21×10^{16}	2.54
$K_L^0 \to \pi^0\pi^0$	8.64×10^{-4}	500	2.74×10^{17}	57
$K_L^0 \to \pi^+\pi^-\pi^0$	12.54%	500	1.89×10^{15}	40%
$K_L^0 \to \pi^\pm e^\mp \nu$	40.55%	500	5.83×10^{14}	12%
$K_L^0 \to \pi^\pm \mu^\mp \nu$	27.04%	500	8.74×10^{14}	18%
$K_L^0 \to \gamma\gamma$	5.47×10^{-4}	1500	4.32×10^{17}	90
$K_L^0 \to \pi^0\nu\nu$	N/A	500	N/A	N/A

We further add the Tmon data to the MC event in the way below. The energy of each channel is the sum of the tmon event and the MC event, and timing is determined in the same way as data waveform.

5.5 Monte Carlo Data Sample Statistics

We generate the Monte Carlo samples for each K_L^0 decay mode, as well as the beam neutrons. Each MC file has 5000 K_L^0s generated at target. Table 5.2 shows the statistics of each mode compared to the amount of data collected.

CHAPTER VI

K_L^0 Flux Measurement

6.1 Overview

The goal of this chapter is to calculate K_L^0 flux from the three normalization modes: $K_L^0 \to \pi^0 \pi^0 \pi^0$, $K_L^0 \to \pi^0 \pi^0$ and $K_L^0 \to \gamma\gamma$. From K_L^0 flux, the single event sensitivity can be calculated.

These three modes are chosen because first of all, the decay modes have only photons in the final state and the KOTO detector has good photon energy resolution and consequently good ability of reconstructing π^0 vertex. Second, these three modes have relatively large branching ratios and large statistics. Moreover, these three modes have different event geometries and acceptances, so independent K_L^0 flux measurements from the three modes can be a cross check of the analysis method. It's also a good way to understand the systematic uncertainties of the experiment.

The structure of this chapter is as follows: section 6.2, 6.3 and 6.4 will start with explanation of reconstruction methods, and the cut conditions for the three normalization modes. Afterwards, the acceptance is calculated from Monte Carlo, which is compared with data for agreement check. It is followed by the result of K_L^0 flux and systematic uncertainty estimation.

6.2 $K_L^0 \to \pi^0 \pi^0 \pi^0$

6.2.1   Reconstruction Method

The $K_L^0 \to \pi^0 \pi^0 \pi^0$ samples are events having 6 or more photon hits in the CsI crystals. There are cases where more than 6 photons hit the CsI crystals, which is most likely from pileup events or accidental activity coincidence. In such cases, six clusters which have the closest timing are selected, and the ones not included are called "*extra photons*" whose timing will be a kinematic cut later. Figure 6.1 shows the event display of an $K_L^0 \to \pi^0 \pi^0 \pi^0$ event.
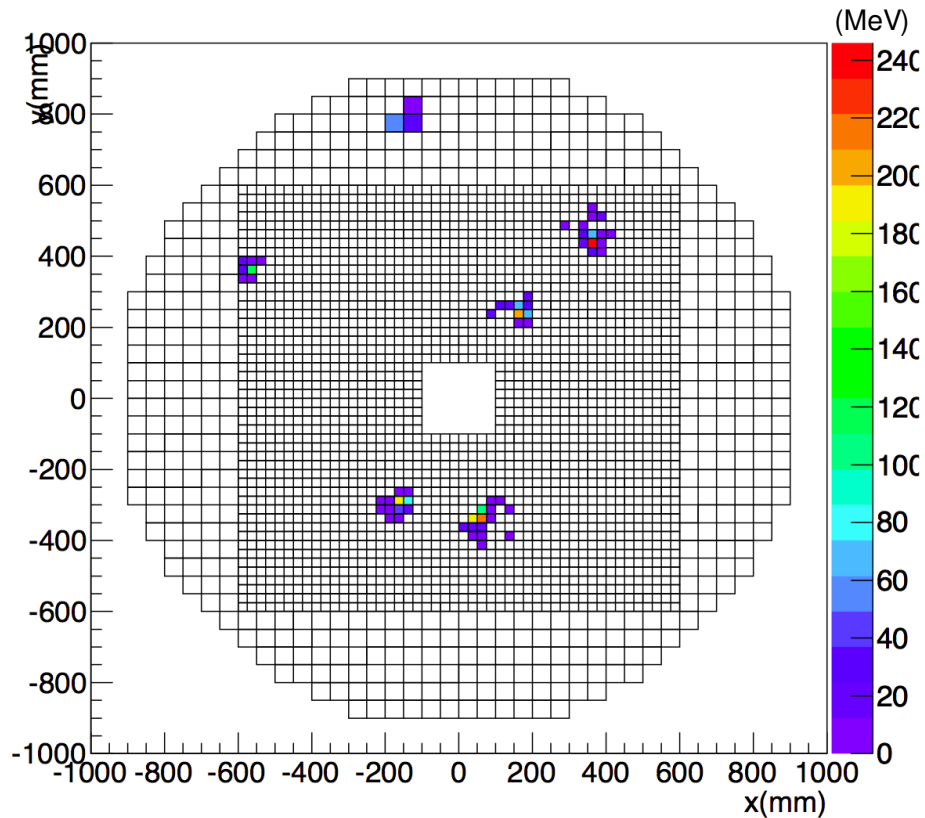
Figure 6.1: The event display of one $K_L^0 \to \pi^0 \pi^0 \pi^0$ event

The K_L^0 reconstruction will be performed with the information of the six photons. The process is as follows.

As the first step, π^0 vertex reconstruction is done for all combinations of two

photons assuming a fixed π^0 mass and a fixed transverse decay point at origin. In this step, the total number of combinations is $C_6^2 = 15$. Of all the pairing choices, the one with the smallest χ^2 is chosen. The pairing with 2nd best χ^2 is also recorded for cuts later. The detailed process is described in section 2.4.

The probability of mis-paring using this method is shown in Figure 6.2. The plot is drawn from $K_L^0 \to \pi^0\pi^0\pi^0$ MC with accidental overlaid. The mis-paring ratio, i.e. the ratio of the number of mis-paired events and the number of reconstructed K_L^0 is 28.2%. With kinematic cuts, the mis-matched ratio is reduced by a factor of 100, and with veto cuts, the Dalitz decay and extra photon events are removed, which gives a mis-pairing ratio of less than 1%.
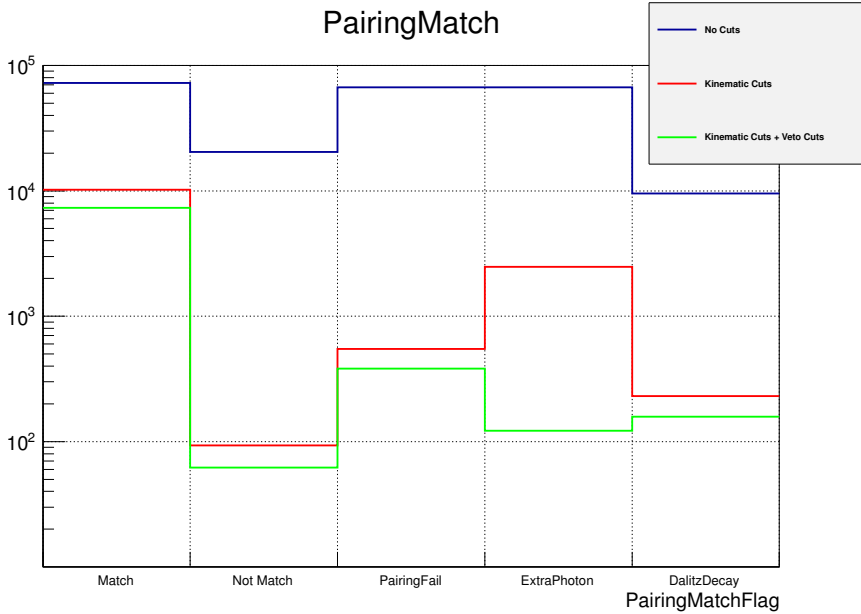
Figure 6.2: The mis-pairing in $K_L^0 \to \pi^0\pi^0\pi^0$ reconstruction. $K_L^0 \to \pi^0\pi^0\pi^0$ Monte Carlo sample with accidental overlaid is used. Bin 1 means all the 6 photon pairing are correct; Bin 2 means any of the 6 photon pairing is wrong; Bin 3 means the matching between the 6 CsI photons and the Monte Carlo tracks cannot be matched, which comes from either an energy mis-match due to shower leakage or merged/escaped photons in company with an accidental hit; Bin 4 contains events with more than 6 photon hits; and Bin 5 is Dalitz decay.

Step two is to calculate the momentum of the pions and kaons. Step one fixed the z positions of the 3 π^0s (z_i) and their resolution (σ_{z_i}). And the x and y positions

are the CoE projected to the target z position. Up to this point, we've assumed the pions having the fixed mass and zero transverse position. Now we can release that constraint, and calculate the kinematic variables of the 3 π^0s. The transverse positions of all the 3 π^0s are at the identical position of the K_L^0, and the momentum can be calculated purely from geometry. The π^0 mass can be calculated thereafter.

To get the correct number of K_L^0, an extra correction with respect to the DAQ efficiency is needed. There are two factors affecting the DAQ efficiency. First, the DAQ trigger efficiency from L2 finite buffer (ϵ_2). Second, the DAQ packet loss efficiency from backend L3 (ϵ_3). The combinational effects has a DAQ efficiency ϵ_{DAQ} which is around 0.8. This number is recorded for each run, and Figure 6.3 shows the variation of the efficiency with respect to time. To compare Monte Carlo and data, the ϵ_{DAQ} is considered for each run, i.e. $N_{signal}^{data} = \sum_i N_{signal,i}/\epsilon_{DAQ,i}$.

6.2.2 Event Selection

The minimal sets of cuts are applied to reduce cut correlations. $K_L^0 \to \pi^0\pi^0\pi^0$ events can be kinematically constructed without using veto information. Table 6.1 lists the kinematic cuts.

Photon energy cut: The energies of the all the 6 photons should be within the range of 100 MeV and 2 GeV (Figure 6.4.(a)-(b))to take advantage of the CsI energy resolution and discard merged clusters.

Photon hit position cut: A CsI fiducial region is defined to make sure that the photon is far away from the center or the edge of the CsI arrays to avoid energy leakage. The fiducial region is defined as between the square of side length 150 mm around the beam hole, and a circle with 850 mm radius. The distribution of the minimum x or y coordination is shown in Figure. 6.4.(c), and the maximum radius shown in Figure 6.4.(d)

Photon distance cut. For all the pairs of the 6 photons, the distance in between
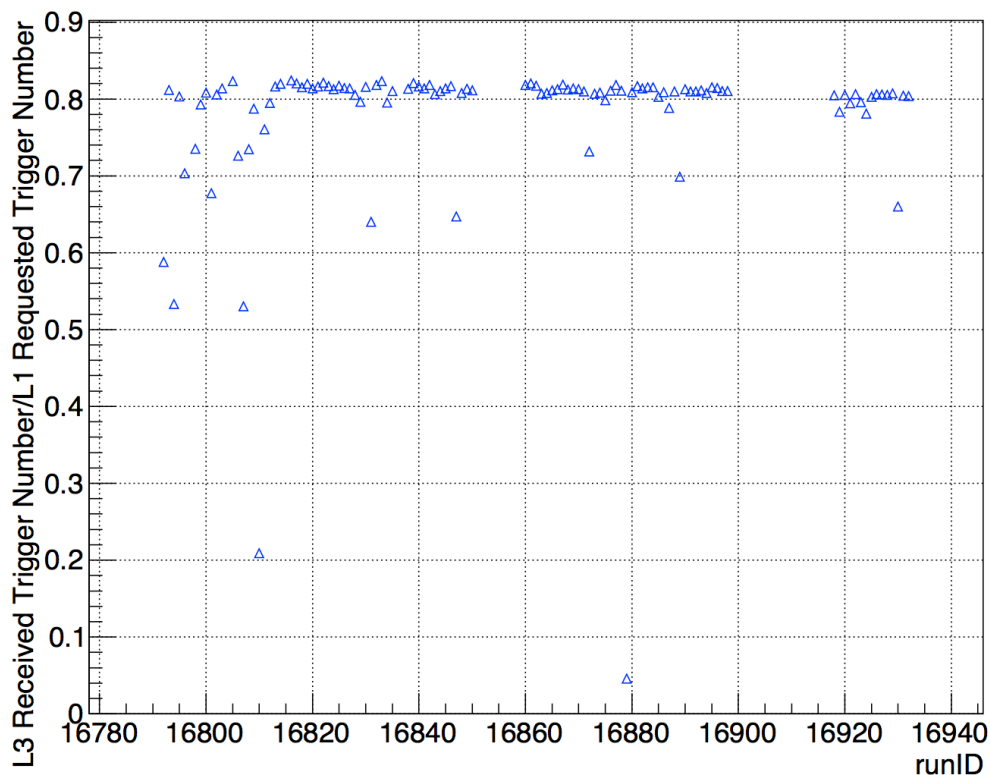
Figure 6.3: The DAQ Efficiency coefficients for each run during the physics data taking

should be larger than 150 mm to suppress clusters formed by multiple photons merging together(Figure 6.5.(a)).

Extra photon timing cut. In case of accidental activities or pileup, the physical event can still be usable as long as the other photons are out of time, i.e. $\delta t > 3ns$(Figure 6.5.(b)).

Once the pairing is done, this set of cuts will suppress mis-pairing events.

π^0 *mass cut.* The biggest deviation of π^0 mass from PDG value 134.98 MeV should be within $\pm 10 MeV$(Figure 6.5.(c)).

π^0 δz *cut.* The maximum distance between the reconstructed π^0 should be within 400 mm(Figure 6.5.(d)). For a 2 GeV π^0, its mean free path $\beta\gamma c\tau = 10^{-7}m$, which is far smaller than the cut.

K_L^0 *decay position cut.* The fiducial decay region is determined from 3000 mm to 5000 mm(Figure 6.6.(a)), where the NCC and CV are excluded to avoid background.

K_L^0 χ_z^2 *cut.* The maximum accepted χ_z^2 is 20 (Figure 6.6.(b)) to make sure the best reconstructed K_L^0 is kinematically sound.

$K_L^0 \Delta\chi_z^2$ cut. In cases of more than one K_L^0, a well separated χ_z^2 removes ambiguous reconstructions. In this analysis, the threshold is set to be 50(Figure 6.6.(c)), which is tight to make sure the sample is pure.

6.2.3 Reconstruction Result

We first check the result from minimum biased triggered events. With all the kinematic cuts applied, the background level is 0.68%. The main backgrounds come from $K_L^0 \rightarrow \pi^\pm e^\mp \nu$ and $K_L^0 \rightarrow \pi^\pm \mu^\mp \nu$ events overlaid with an accidental events with 6 photons.

Figure 6.7 shows the critical kinematic distributions of K_L^0s after all cuts. The K_L^0 beam profile of x and y projection(6.7.(a)-(b)) can be reproduced at the position of T1 target. And the transverse and longitudinal momentum of the K_L^0 beam can be well reproduced as well.

The most important distribution is the K_L^0 mass distribution as shown in Figure 6.8. The reconstructed K_L^0 mass center is 497.9 ± 0.1 MeV, 0.3 MeV higher then the PDG value. The mass width is 4.1 MeV. In the MC, however, the mass center is 497.6 MeV with width of 4.0 MeV. Near the peak value, a positive slope in the data/MC ratio plot indicates a light peak shift and a difference in slew. Some further discussion about this top is in section 6.2.6.

6.2.4 Acceptance Estimation

The Acceptance is estimated from Monte Carlo, which means the ratio of the number of reconstructed $K_L^0 \rightarrow \pi^0 \pi^0 \pi^0$ events and the total number of generated K_L^0
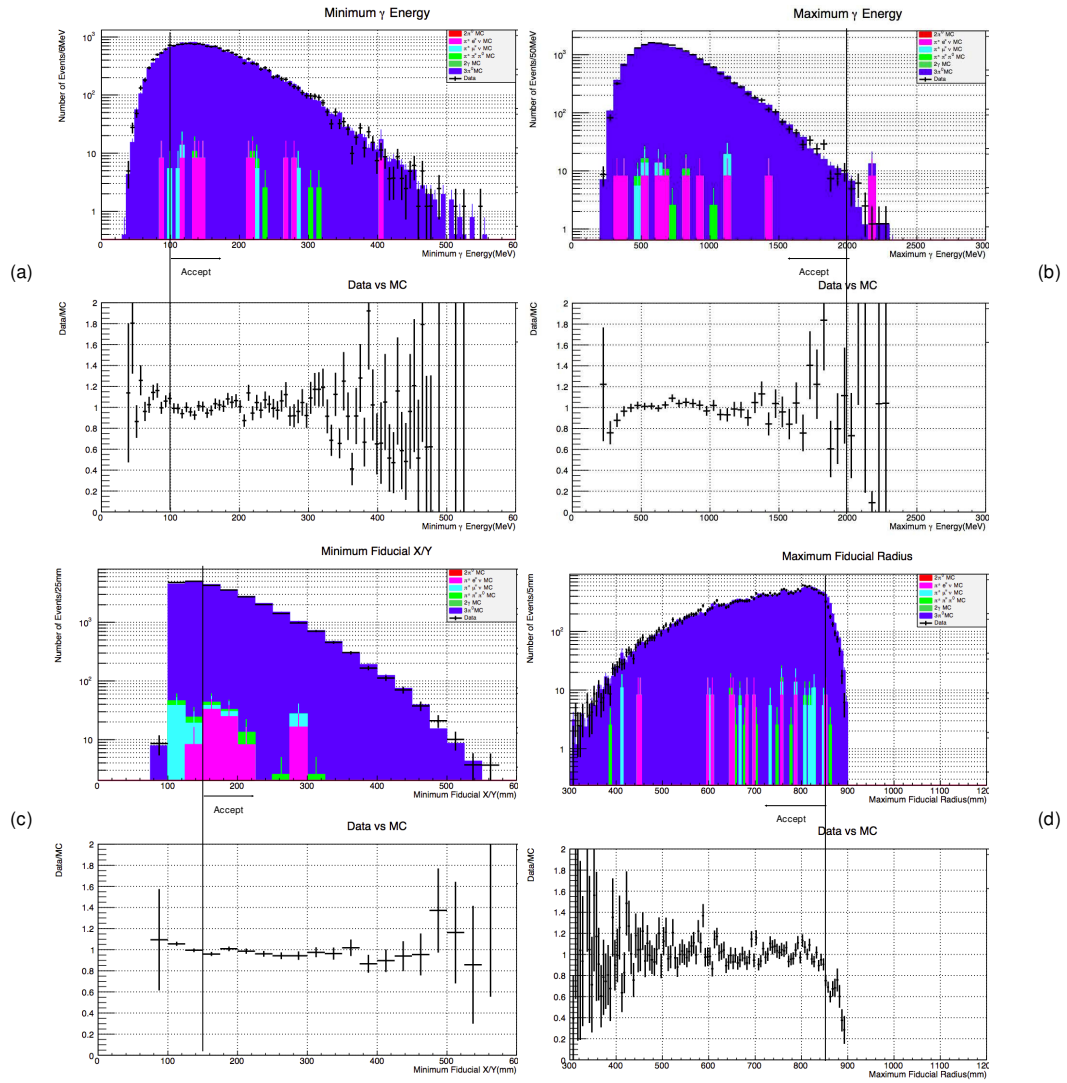
Figure 6.4: The kinematic cuts for $K_L^0 \to \pi^0 \pi^0 \pi^0$ selection(Part I). All the kinematic cuts are applied except the cut under study. (a)-(b) The minimum/maximum photon energy of each event. (c)-(d) The minimum x (or y) and maximum radius of all the 6 photons.
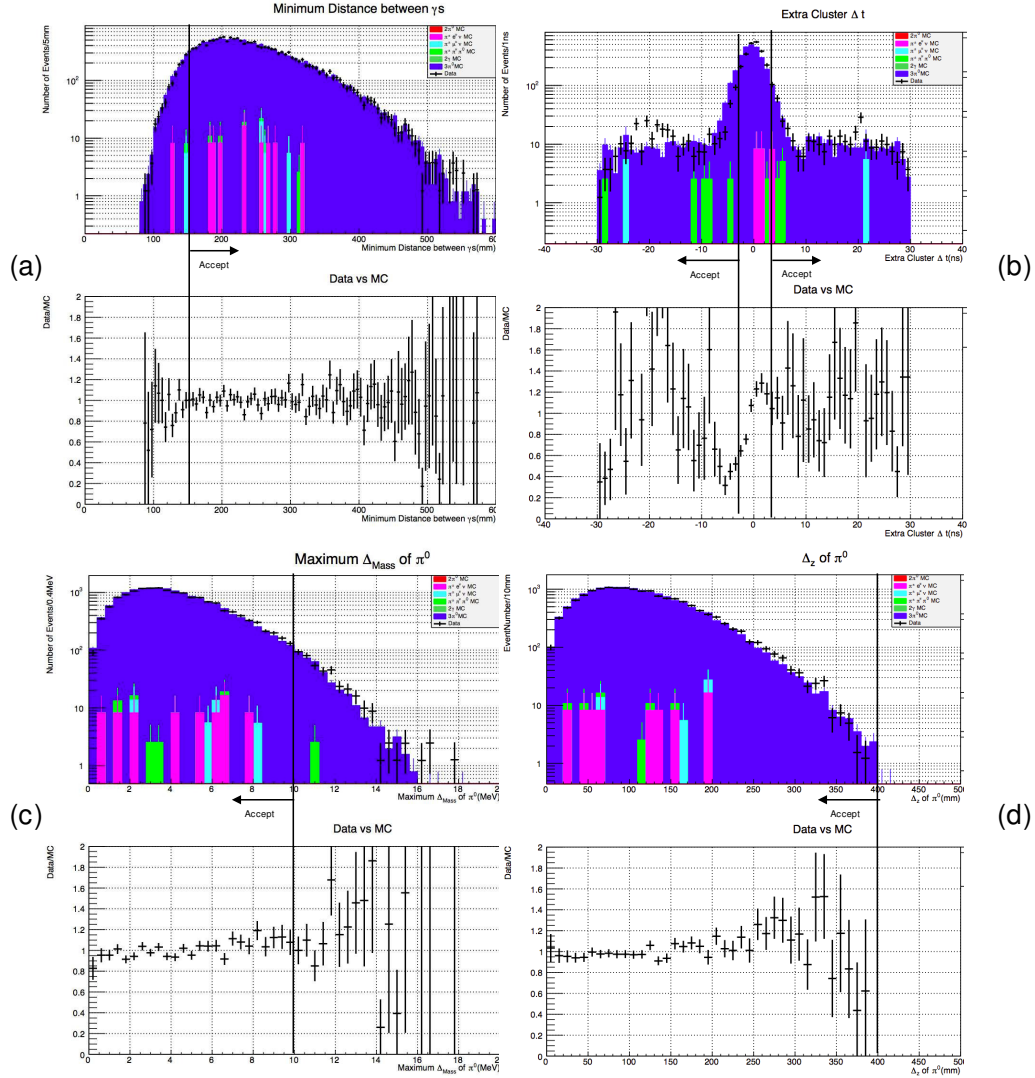
Figure 6.5: The kinematic cuts for $K_L^0 \to \pi^0\pi^0\pi^0$ selection (Part II). All the kinematic cuts are applied except the cut under study. (a) The minimum distance between each photon pair. (b) The timing distribution of the extra photons. (c) The distribution of the maximum π^0 mass deviation from PDG value. (d) The distribution of the biggest distance between reconstructed π^0s.

(a)

(b)

(c)
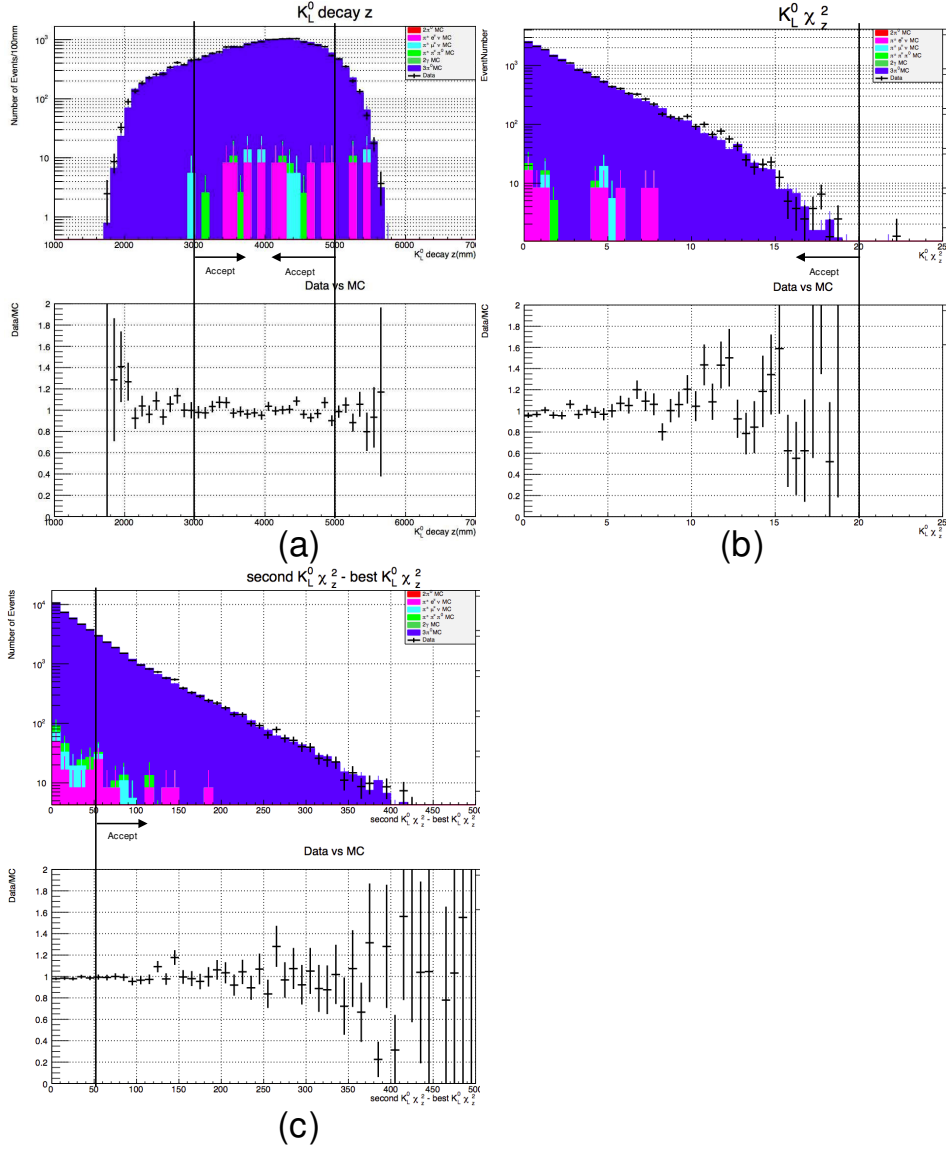
Figure 6.6: The kinematic cuts for $K_L^0 \to \pi^0\pi^0\pi^0$ selection (Part III). All the kinematic cuts are applied except the cut under study. (a) The K_L^0 decay z position. (b) The χ_z^2 distribution of the reconstructed K_L^0. (c)The distribution of the difference between the 2nd best reconstructed K_L^0 and the best K_L^0.
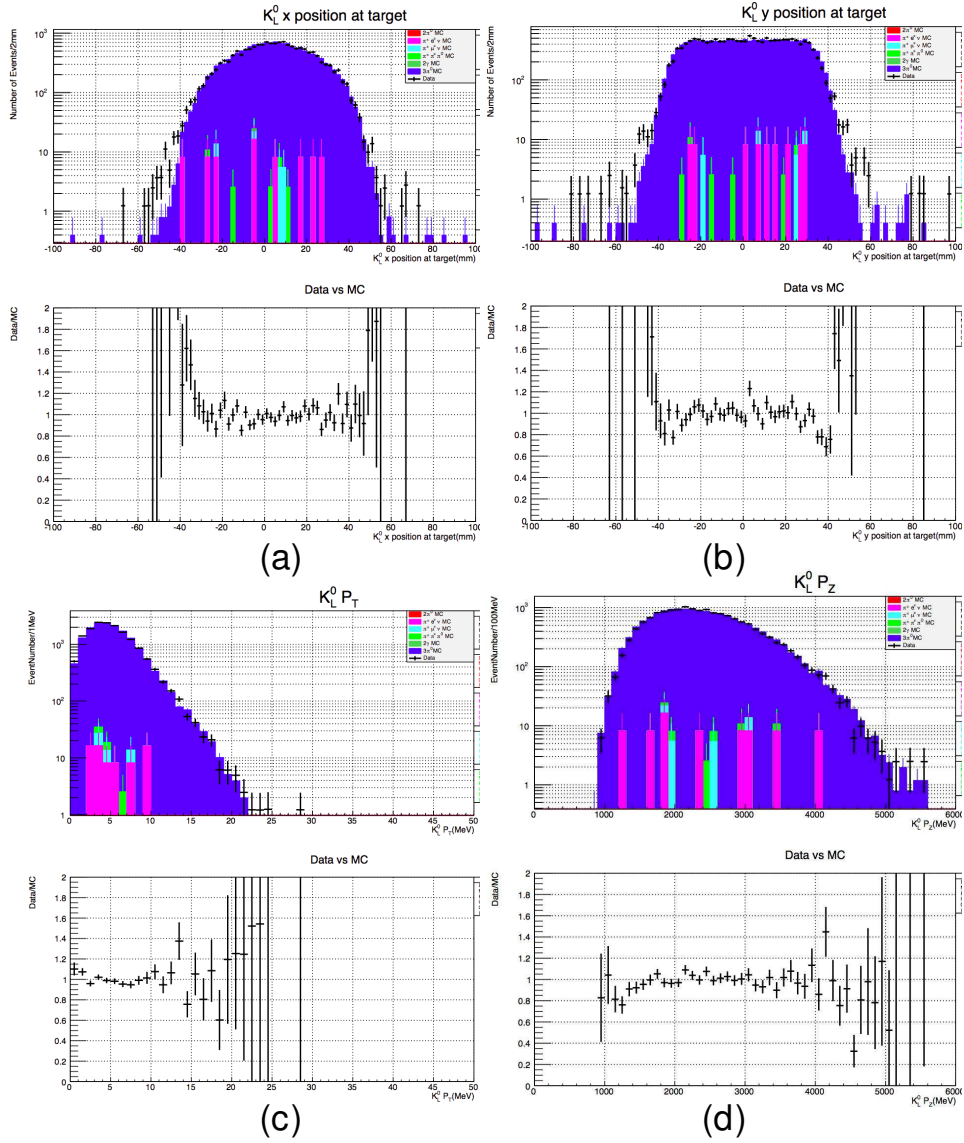
Figure 6.7: The kinematic distributions of K_L^0s after kinematic cuts. (a) The K_L^0 beam profile at T1 target projected in x direction. (b) The K_L^0 beam profile at T1 target projected in y direction.(c) The transverse momentum. (d) The longitudinal momentum.

Table 6.1: Kinematic cuts of $K_L^0 \to \pi^0 \pi^0 \pi^0$ reconstruction

Cut	Range	Comment
Photon energy	[100 MeV, 2 GeV]	The energies of the 6 photons should all be within this range
Photon hit position	[150mm, 850mm]	The x and y positions should be larger than the square of 150mm side, and radius smaller than 850mm
Minimum distance between photons	>150 mm	All combinations of the 6 gammas should have relative distance within this range to avoid cluster merging.
δt for extra photons	>3ns	The timing of the extra photons should be well separated from the main event timing
π^0 maximum δm	<10MeV	The maximum of the difference of reconstructed π^0 mass with respect to the PDG value
π^0 maximum δz	<400mm	The maximum of the difference betwen reconstructed π^0 z position
K_L^0 decay z	[3000mm, 5000mm]	Fiducial decay region
K_L^0 χ_z^2	<20	
ΔK_L^0 χ_z^2	>50	If there are more than one K_L^0s reconstructed, the differences between the second and the best K_L^0 should be large enought to remove ambiguous reconstruction
$\Delta m_{K_L^0}$	<15MeV	Difference between reconstructed K_L^0 mass and its PDG value
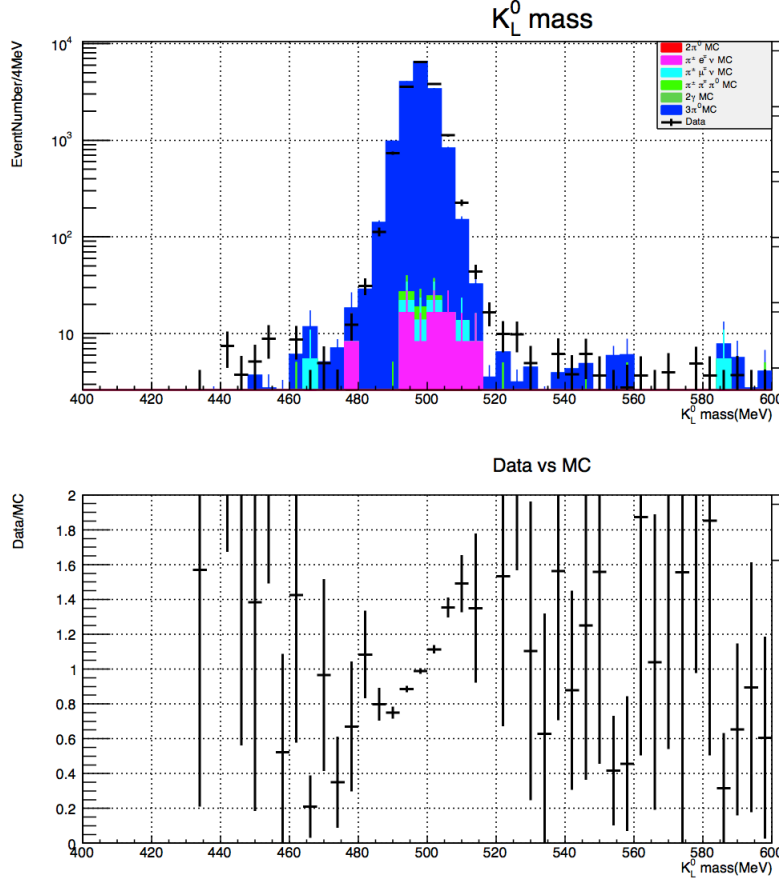
Figure 6.8: The K_L^0 mass distribution from $K_L^0 \to \pi^0\pi^0\pi^0$ decay mode

at target. The acceptance for the minimum biased trigger is

$$A_{3\pi^0} = (1.60 \pm 0.01_{stat}) \times 10^{-8} \qquad (6.1)$$

6.2.5 Veto Loss Due to Shower Leakage and Backsplash

For normalization triggers, there are two cases where $K_L^0 \to \pi^0\pi^0\pi^0$ signal events are mistakenly vetoed on-line: the back-splash and shower leakage. The back-splash cases, illustrated in Figure 6.9.(a), are cases where the electromagnetic shower have backward reflected components and some low energy electrons travel backwards and deposit energy inside the CV. The shower leakage cases mean the clusters which hit close to the outer edge of the CsI crystals have part of their energy deposit inside

Table 6.2: The veto cuts applied offline to remove the online veto effect for normalization events

Offline veto cut	Cut value
MB total energy	50 MeV
CV total energy	0.8 MeV
CC03 total energy	100 MeV
NCC total energy	100 MeV

the MB modules as illustrated in 6.9.(b). The CV veto energy distribution (Figure 6.10)for the normalization modes shows the online cut effect.
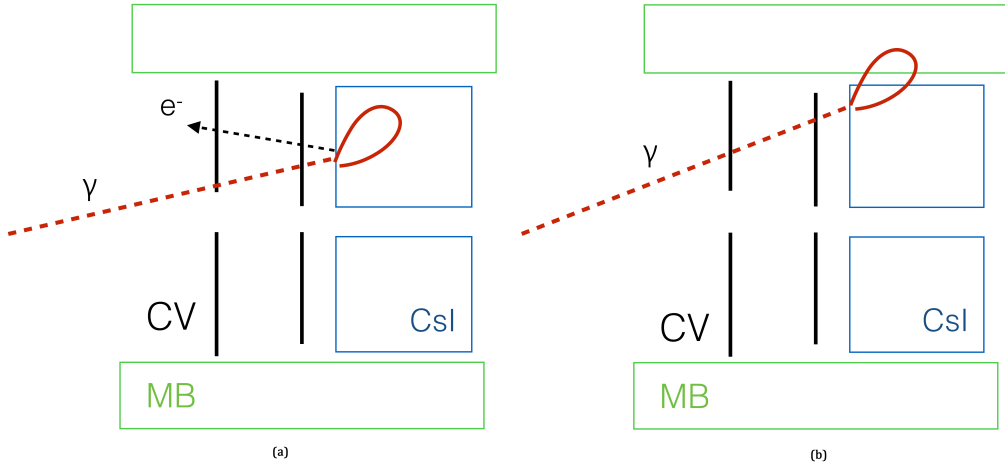
Figure 6.9: The cartoon of events that causes online veto loss. (a) The backsplash events. (b) The shower leakage events

The event loss can be measured by comparing the number of reconstructed $K_L^0 \to \pi^0\pi^0\pi^0$ events between minimum biased data sets where no online veto is applied, to the normalization data sets where online veto is applied. The same set of cuts are applied. And the signal loss is measured to be 14.8%. To remove this online cut effect, some extra veto cuts slightly tighter than the online cuts are applied offline before the analysis is done.

The table of offline veto cuts are shown in Table 6.2. The normalization mode's result is concluded in section 6.2.8.
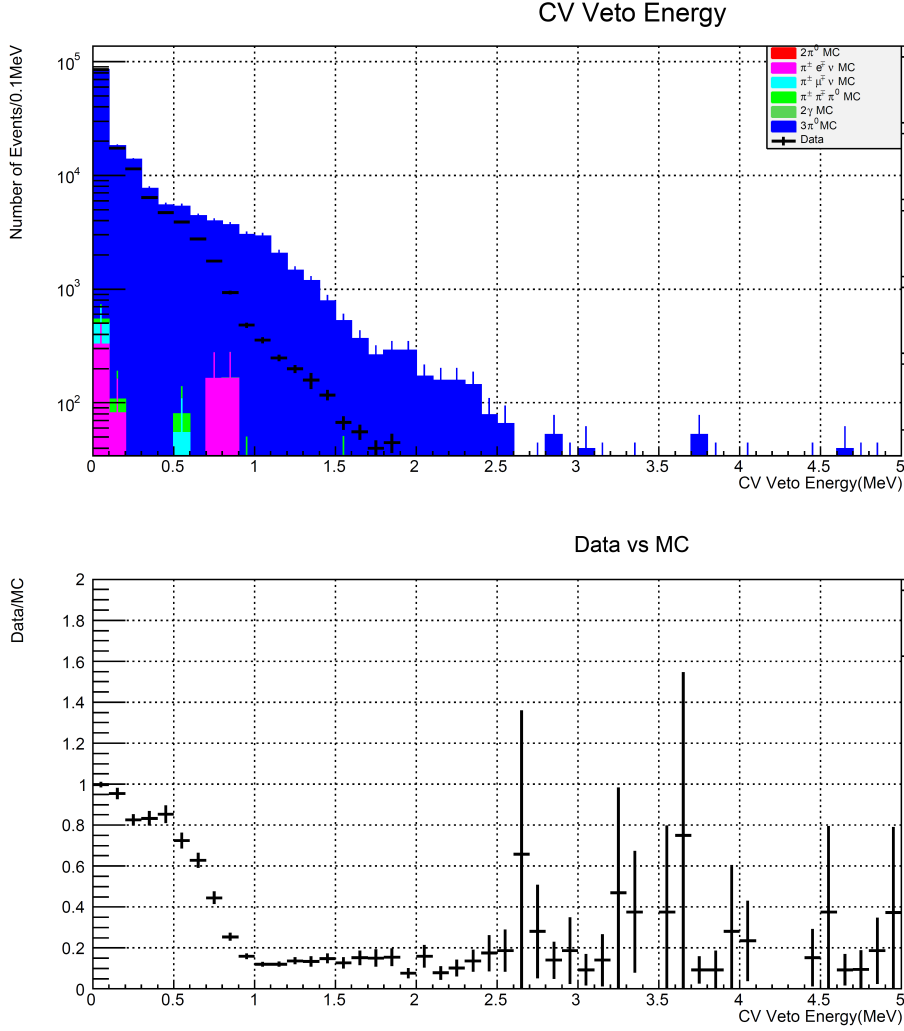
Figure 6.10: The CV veto energy distribution of normalization events after all the kinematic cuts, and without offline veto cuts.

6.2.6 Discussion on the K_L^0 Mass Distribution

As shown in section 6.2.3, the K_L^0 mass peak mean is 0.3 MeV higher than the MC (PDG value as well), and a difference is skewed. Here the sources of the discrepancies are explored.

In the lowest order, the mass peak shift points to the overall energy scale of the CsI detector, which comes from the Al target calibration. But it should not be a critical one since the reconstructed π^0 mass is correct as shown in Figure. 3.6. However, this point is still studied to understand the sensitivity of the K_L^0 mass peak value to the

95
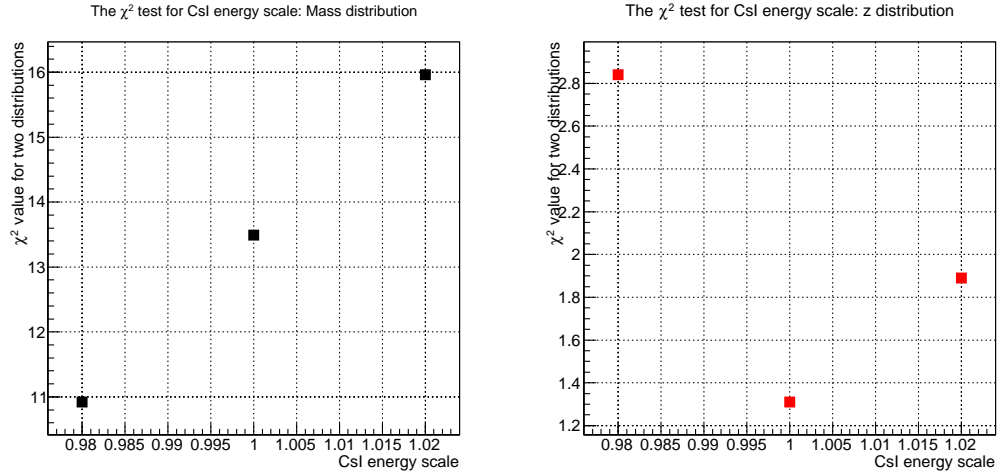
Figure 6.11: The χ^2 test results in terms of the CsI energy scale sensitivity to K_L^0 mass peak and decay z.

overall energy scale. Here an overall energy scale variation of 2%is applied to each CsI crystal for the MC samples. And a χ^2 test is performed in terms of the mass distribution and the decay z distribution. Figure 6.11 shows the χ^2 values of between the mass distribution χ^2 test (left), and the decay z position (right) between data and MC. The distributions themselves are concluded in the Appendix A

The mass distribution shows a preference of smaller energy scale but the decay z distribution prefers the energy scale $= 1$. Combined results conclude the energy scale is correct.

Higher order effects like the light yield are more sensitive to the shape of the mass distribution. Section 6.2.7 indicates the systematic uncertainties from the K_L^0 mass cut is as little as 0.2% and is further efforts are neglected.
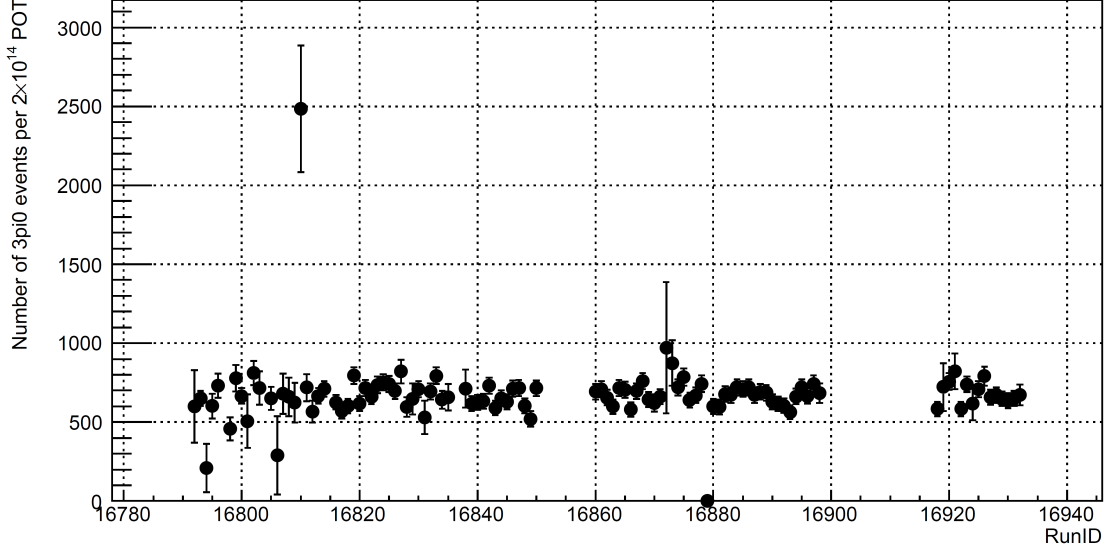
Figure 6.12: The number of reconstructed K_L^0 events every 2×10^{14} POT as a function of run ID.

The stability of number of reconstructed K_L^0s during the whole run period is recorded in Figure 6.12 as a way to show stable detector state and data quality.

6.2.7 Systematic Uncertainties

The systematic uncertainty comes from detector response the Monte Carlo cannot simulate well. This discrepancy will cause the acceptance to deviate from the "true" value. To quantitatively describe this effect, we define the exclusive acceptance, which means the ratio of number of events with all cuts and the number of events with one cut removed, i.e.

$$A_i = \frac{Number\ of\ events\ with\ cut\ i}{Number\ of\ events\ without\ cut\ i} \tag{6.2}$$

The exclusive acceptance reflects if the cut i is related. If cut i is completely unrelated, the number should be 1. The other quantity is the fractional difference F_i, where

$$F_i = \frac{A_{Data,i} - A_{MC,i}}{A_{Data,i}} \tag{6.3}$$

97

. In this definition, the fractional difference is the difference between Monte Carlo and data normalized to data, and the farther away from 0 F_i is, the bigger difference between Monte Carlo and data is. And to get the systematic uncertainty, it can be calculated by summing up all cuts:

$$SysErr^2 = \frac{\sum_{i=allcuts}(F_i/A_{Data,i})^2}{\sum_{i=allcuts}(1/A_{Data,i})^2} \tag{6.4}$$

The exclusive acceptance and fractional difference of each kinematic cut is plotted in Figure 6.13 for minimum biased events and Figure 6.14 for normalization events. For minimum biased trigger, the biggest contribution is from the $K_L^0 \Delta\chi^2$ cut, which is enhanced by its big reduction ratio. And the total systematic uncertainty is 1.76%. For normalization trigger, on the other hand, the photon position cut has the biggest contribution making the systematic uncertainty increased to 3.4%.
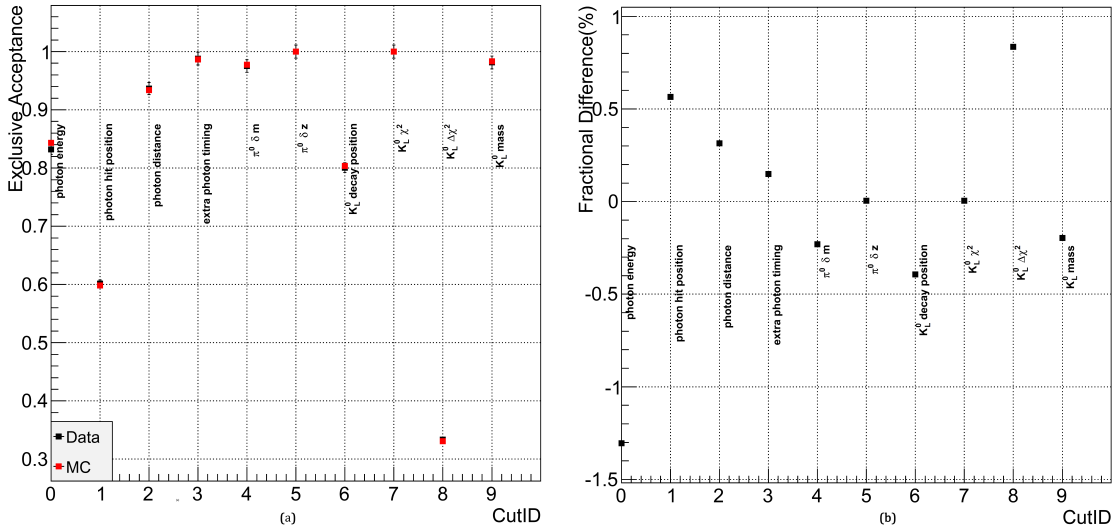

Figure 6.13: The systematic uncertainty of the K_L^0 flux measurement from $K_L^0 \rightarrow \pi^0\pi^0\pi^0$ minimum biased samples. (a) The exclusive acceptance (Equation 6.2) of each cut. (b) The fractional difference (Equation 6.3) of each cut.

6.2.8 Conclusion

The K_L^0 flux calculation from the $K_L^0 \rightarrow \pi^0\pi^0\pi^0$ mode is summarized in Table 6.3.
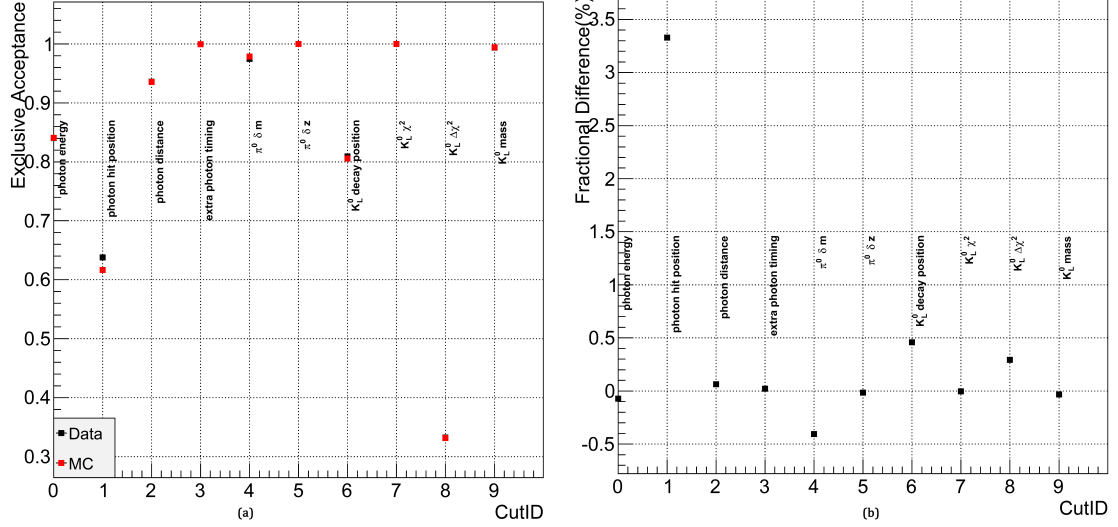
Figure 6.14: The systematic uncertainty of the K_L^0 flux measurement from $K_L^0 \to \pi^0\pi^0\pi^0$ normalization samples. (a) The exclusive acceptance (Equation 6.2) of each cut. (b) The fractional difference (Equation 6.3) of each cut.

Table 6.3: K_L^0 flux measurement from $K_L^0 \to \pi^0\pi^0\pi^0$ mode

Trigger Mode	Number of signals	Acceptance	Flux
Minimum biased	$(16.05 \pm 0.13) \times 10^3$	$(1.60\pm0.01)\times 10^{-8}$	$(3.01 \pm 0.03_{stat} \pm 0.01_{sys}) \times 10^{11}$
Normalization	$(127.91 \pm 0.36) \times 10^3$	$(1.30\pm0.01)\times 10^{-8}$	$(2.96 \pm 0.02_{stat} \pm 0.02_{sys}) \times 10^{11}$

6.3 $K_L^0 \to \pi^0\pi^0$

6.3.1   Reconstruction Method and Event Selection

Events with 4 photon hits are selected. Similar to $3\pi^0$ case, all combinations of pairing is considered and the pairing with the smallest χ^2 is chosen (details described in section 2.4).

The handling of veto is critical for this mode since the biggest background is $K_L^0 \to \pi^0\pi^0\pi^0$ with MB missing detection. The first step to handle veto is to choose a veto timing window. Once reconstruction is done and decay time is fixed, the veto energy deposit within a few ns is recorded. For most of the veto detectors, the veto energy is determined by the largest energy deposit in a single module.

99

The kinematic cuts are identical to the values used for $K_L^0 \to \pi^0\pi^0\pi^0$ (Table 6.1). The veto cuts are included in Table 6.4. Figure 6.15, 6.16, 6.17 show the distribution of each kinematic cut. Figure 6.18 shows the kinematic values of the K_L^0 after all the cuts. The veto energy distribution is listed in Appendix B.

Table 6.4: Veto cuts of $K_L^0 \to \pi^0\pi^0$ reconstruction.

Detector	Veto Energy (MeV)	Veto Time Window (ns)
MB	2	60
FBAR	2	40
OEV	2	20
CV	0.2	80
BCV	1	60
LCV	0.6	30
NCC	2	40
CC03	3	30
CC04 Scintillator	1	30
CC04 CsI	3	30
CC05 (Scintillator)	1	30
CC05 (CsI)	3	30
CC06 (Scintillator)	1	30
CC06 (CsI)	3	30
BHCV	0.3	200
BHPV	3 (Coincident hits)	200

Due to the fact that the offline veto cuts are much tighter than the online veto cut, the online cut does not affect the result. Also the normalization trigger has larger statistics than the minimum biased trigger, so only the normalization mode result is shown here. The minimum biased result will be concluded in section 6.3.4.

6.3.2 Acceptance

From the K_L^0 mass distribution, the signal region 485-505 MeV has a non-neglegible amount of $K_L^0 \to \pi^0\pi^0\pi^0$ background. To extract the number of background, MC is relied on and the acceptance is calculated as

$$A_{2\pi^0} = \frac{number\ of\ 2\pi^0\ MC\ events\ after\ all\ cuts}{Generated\ K_L^0 \times Br(K_L^0 \to \pi^0\pi^0)} \tag{6.5}$$

Figure 6.15: The kinematic cuts for $K_L^0 \to \pi^0\pi^0$ selection(Part I). All the kinematic cuts are applied except the cut under study and the K_L^0 mass cut. (a)-(b) The minimum/maximum photon energy of each event. (c)-(d) The minimum x (or y) and maximum radius of all the 6 photons

Figure 6.16: The kinematic cuts for $K_L^0 \to \pi^0\pi^0$ selection (Part II). All the kinematic cuts are applied except the cut under study and the K_L^0 mass cut. (a) The minimum distance between each photon pair. (b) The timing distribution of the extra photons. (c) The distribution of the maximum π^0 mass deviation from PDG value. (d) The distribution of the biggest distance between reconstructed π^0s.
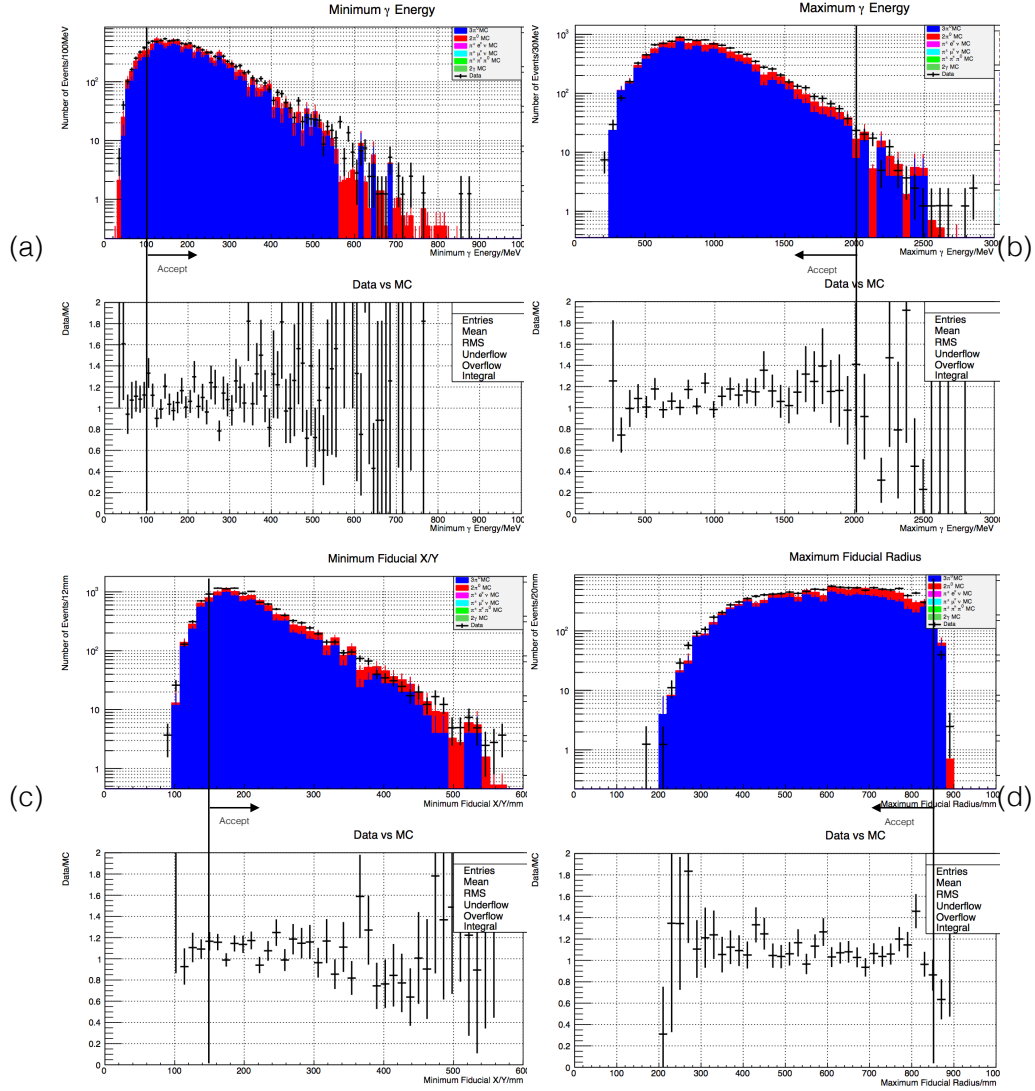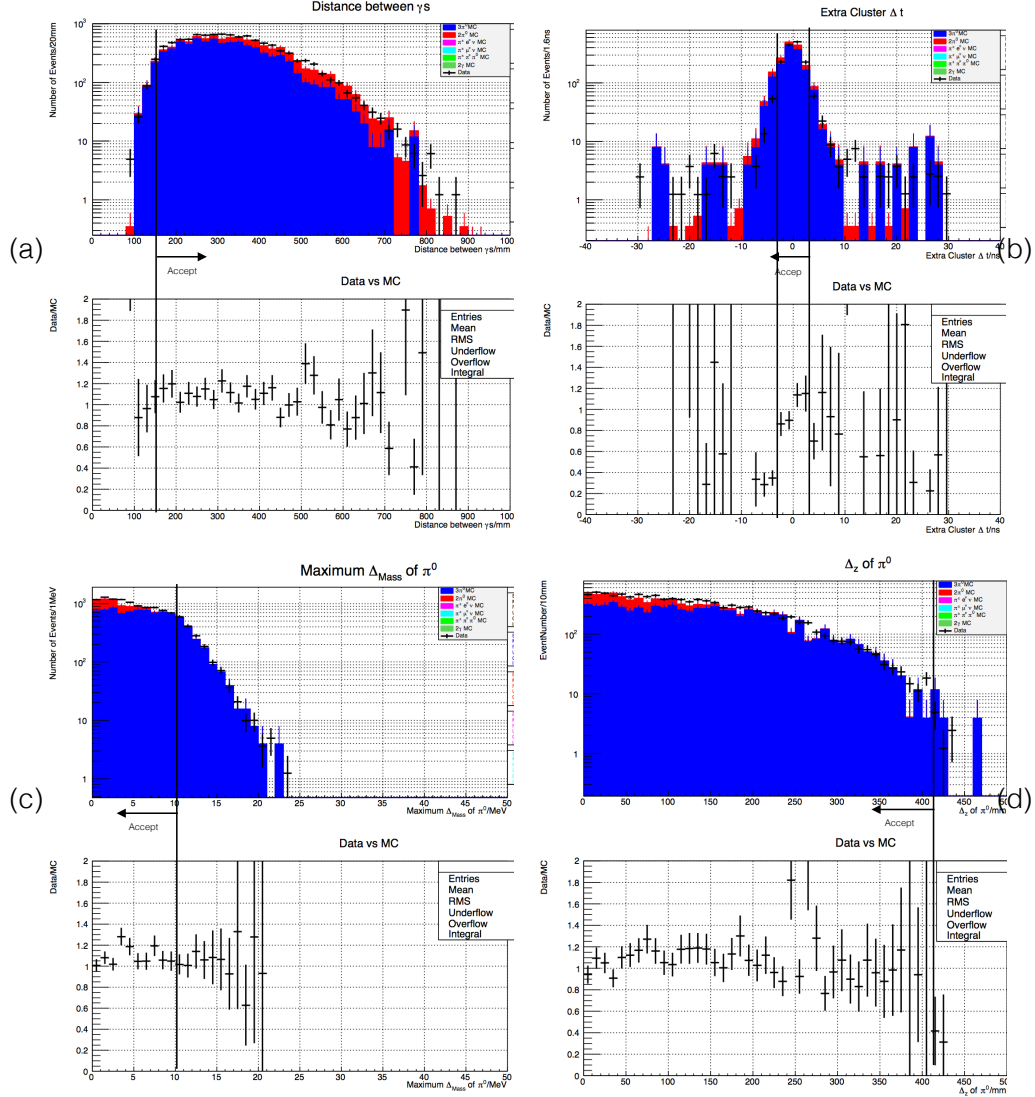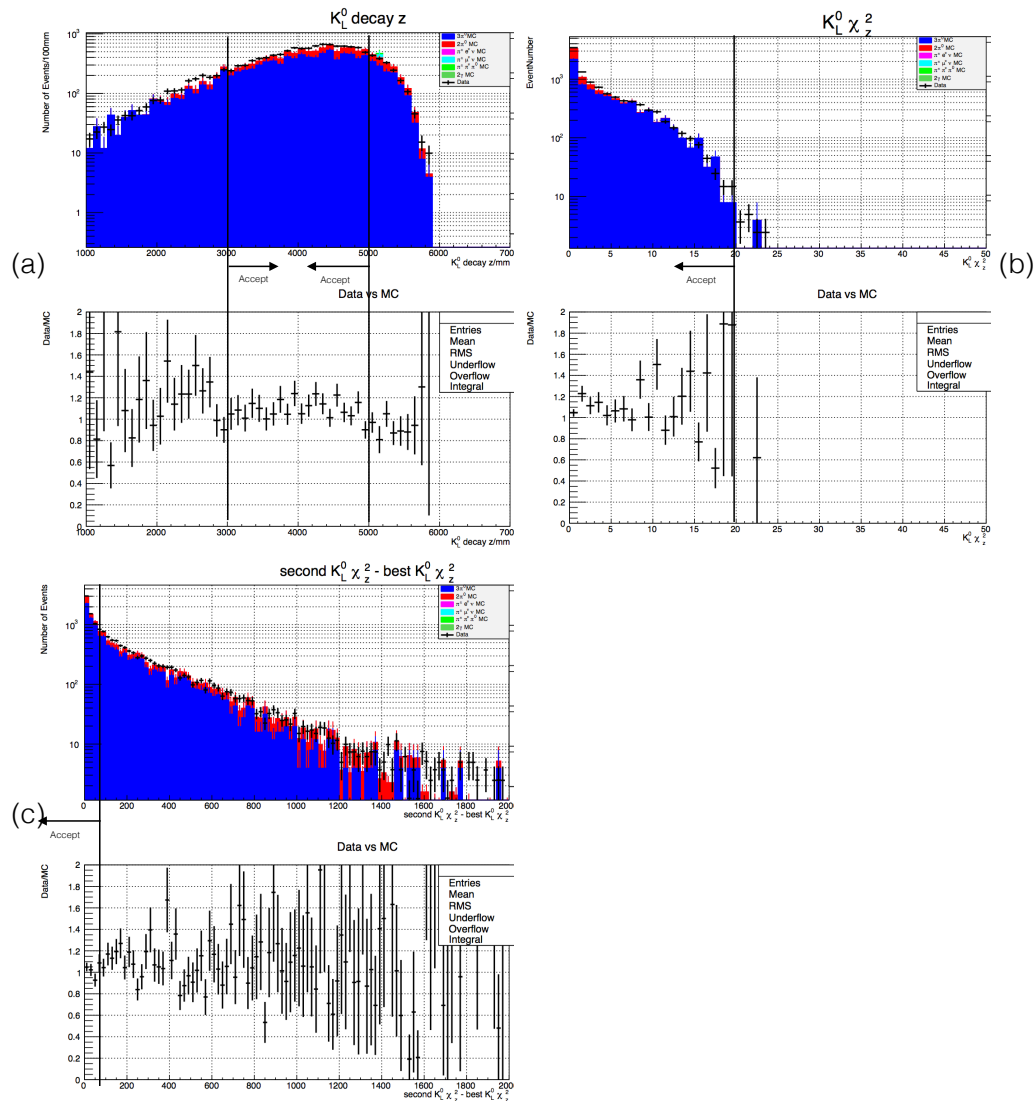
Figure 6.17: The kinematic cuts for $K_L^0 \to \pi^0\pi^0$ selection (Part III). All the kinematic cuts are applied except the cut under study and K_L^0 mass cut. (a) The K_L^0 decay z position. (b) The χ_z^2 distribution of the reconstructed K_L^0. (c)The distribution of the difference between the 2nd best reconstructed K_L^0 and the best K_L^0.
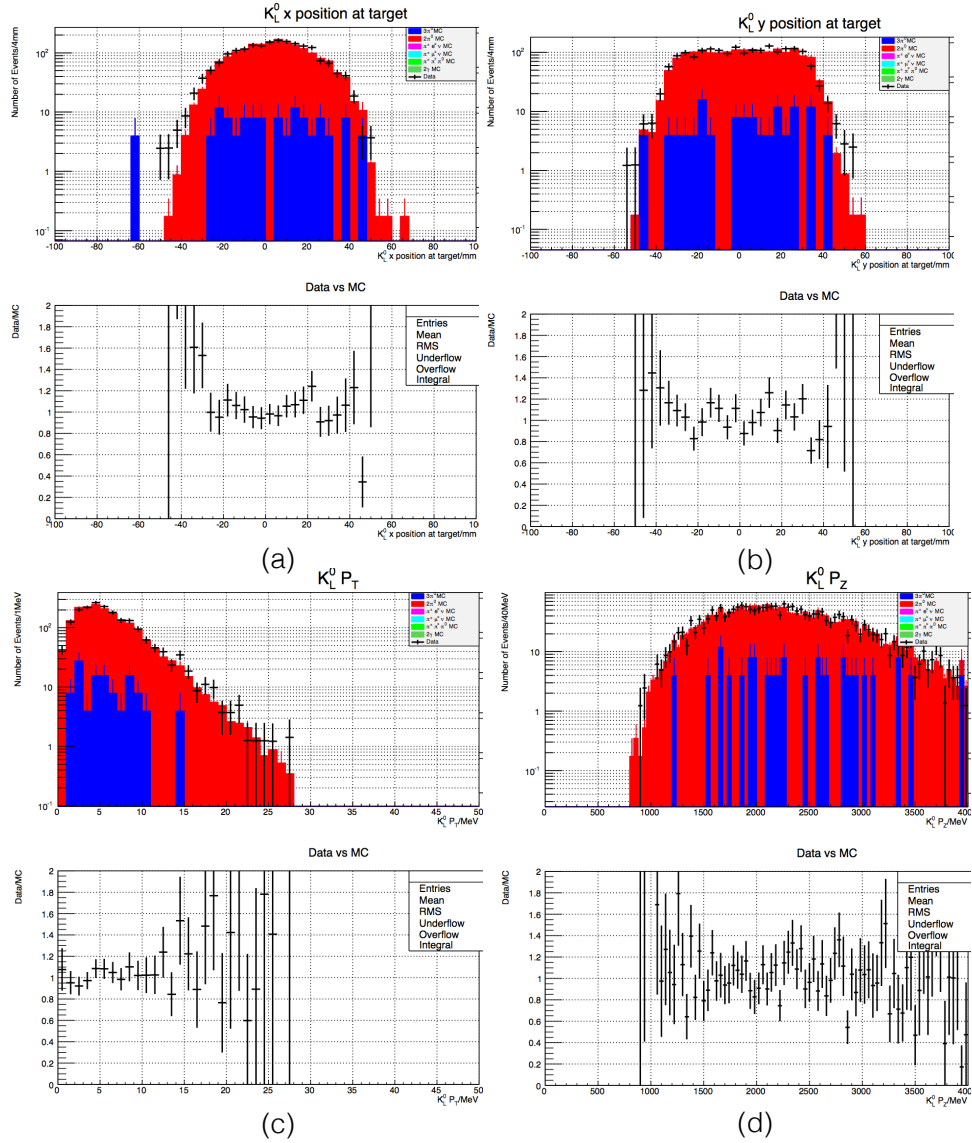
Figure 6.18: The kinematic distributions of K_L^0s after all cuts cuts. (a) The K_L^0 beam profile at T1 target projected in x direction. (b) The K_L^0 beam profile at T1 target projected in y direction.(c) The transverse momentum. (d) The longitudinal momentum.

104

Figure 6.19: The mass distribution of reconstructed K_L^0 from $K_L^0 \to \pi^0\pi^0$ mode.

The result is $(1.82 \pm 0.01_{sys}) \times 10^{-7}$.

6.3.3 Systematic Uncertainties

The veto cuts are treated in the same way as the kinematic cuts. An exclusive acceptance and fractional difference are calculated for each veto. Figure 6.20 shows the amount of errors for each cut.
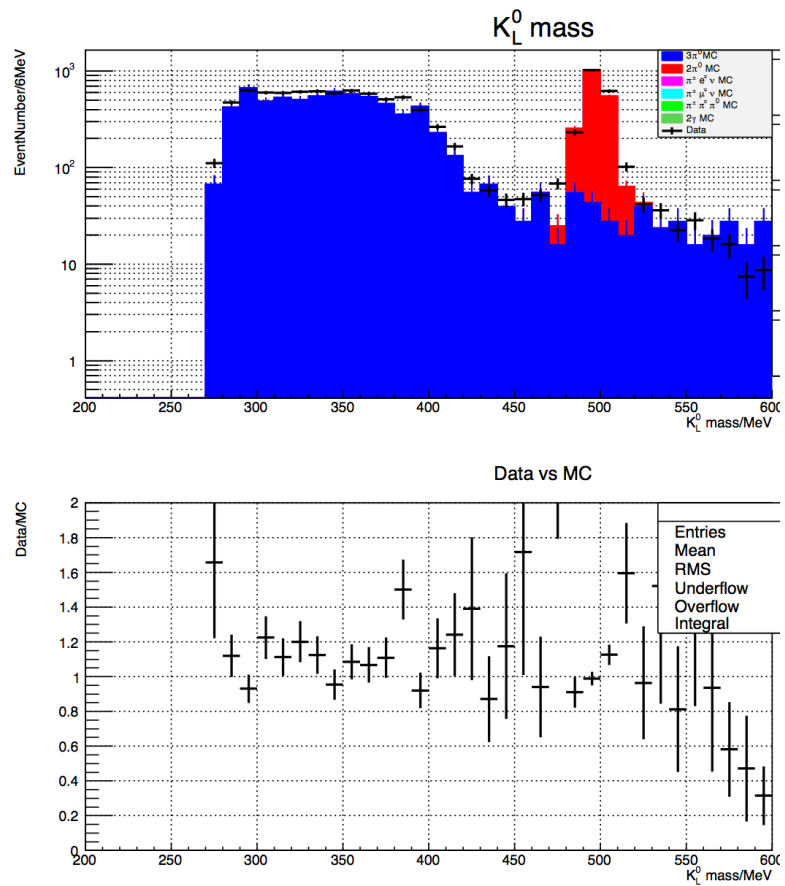
The biggest contributions are the CV (9.9%)(see Figure B.1) due to the fact that the online veto effect is not excluded by the offline cut. The total systematic uncertainty is 14%.

6.3.4 Conclusion

Here concludes the K_L^0 flux calculation from the $K_L^0 \to \pi^0\pi^0$ mode in Table 6.5.

Table 6.5: K_L^0 flux measurement from $K_L^0 \to \pi^0\pi^0$ mode

Trigger Mode	Number of signals	Acceptance	Flux
Minimum biased	206 ± 14	$(1.82\pm0.02)\times 10^{-7}$	$(3.40 \pm 0.24_{stat} \pm 0.10_{sys}) \times 10^{11}$
Normalization	$(1.90\pm0.04)\times 10^3$	$(1.82\pm0.01)\times 10^{-7}$	$(3.13 \pm 0.08_{stat} \pm 0.44_{sys}) \times 10^{11}$

6.4 $K_L^0 \to \gamma\gamma$

6.4.1 Reconstruction Method and Event Selection

$K_L^0 \to \gamma\gamma$ mode is kinematically solvable. Assuming the mass of K_L^0 its PDG value and also the radial positions of K_L^0 to be at origin, we can fully determine the decay position of K_L^0 by using equation 2.17 and 2.18.

Table 6.6 shows the kinematic cut, and the veto cuts are identical to Table 6.4. To make sure that the two γs are back to back in the K_L^0 center-of-mass frame, an
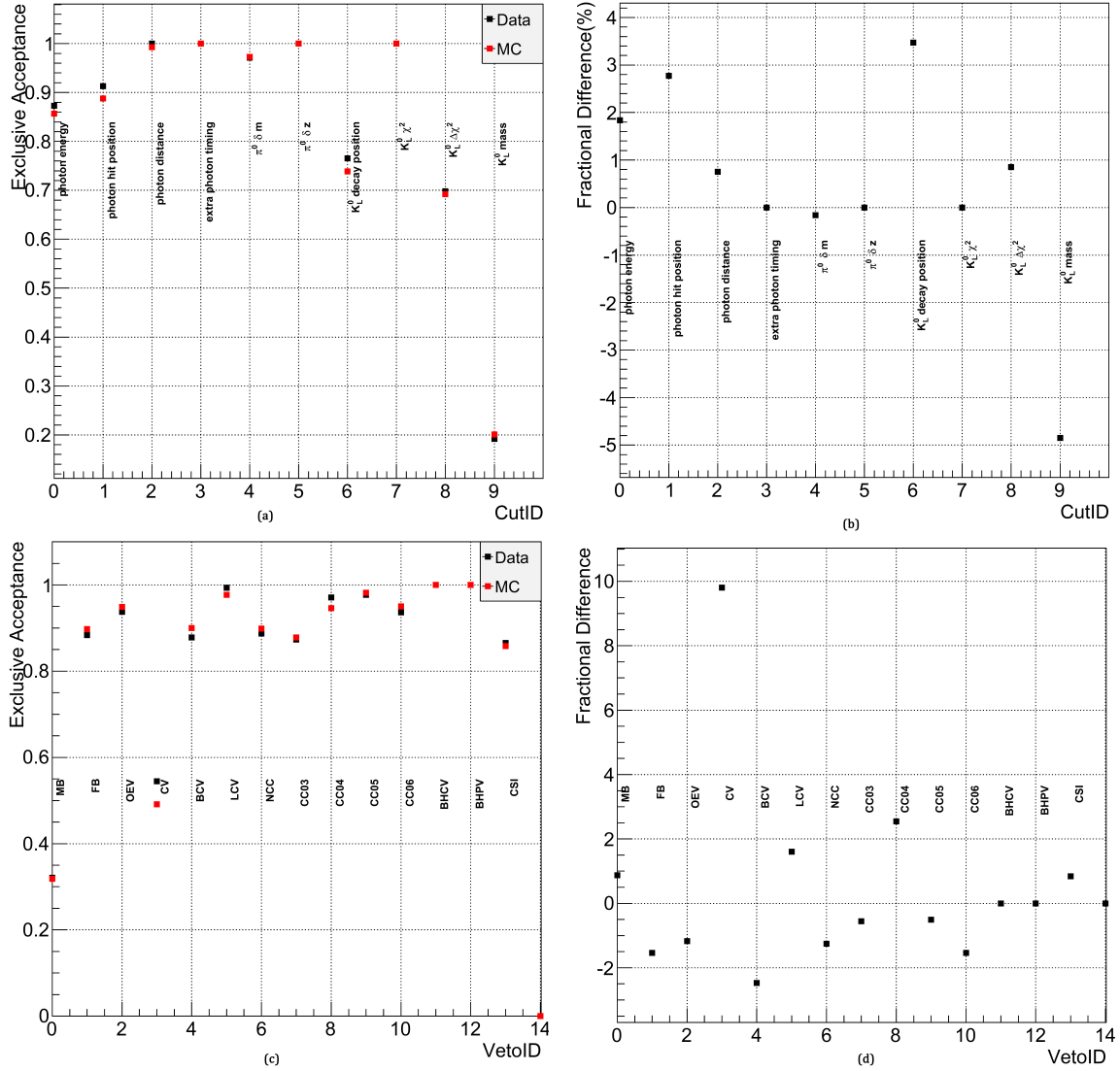
Figure 6.20: The systematic uncertainties for $K_L^0 \to \pi^0\pi^0$ mode (a) The exclusive acceptance of the kinematic cuts. (b) The fractional difference of the kinematic cuts. (c) The exclusive acceptance of the veto cuts. (d) The fractional difference of the veto cuts.
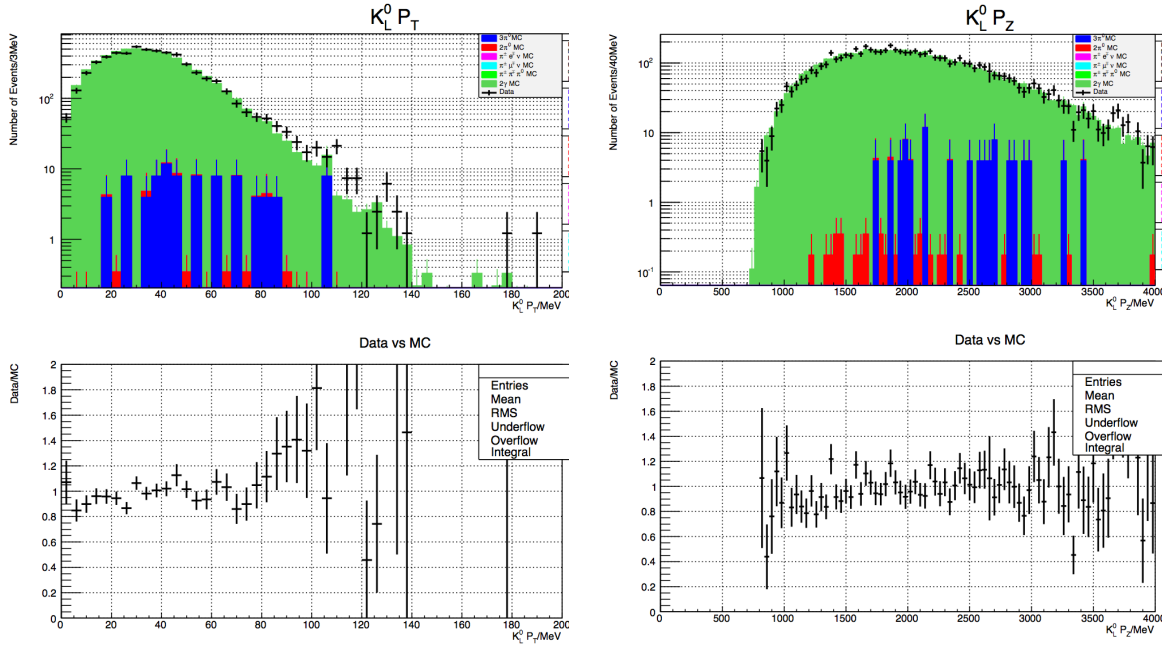
Figure 6.21: The momentum distribution of the reconstructed K_L^0 from $K_L^0 \rightarrow \gamma\gamma$ mode

additional cut of *Projection angle* cut is applied. The projection angle is the angle between the two γ tracks in the lab frame.

All the distributions of the kinematic cuts can be found in Appendix C. And here only the K_L^0 momentum distribution is shown in figure 6.21 with good agreement between MC and data.

Table 6.6: Kinematic cuts of $K_L^0 \to \gamma\gamma$ reconstruction

Cut	Range	Comment
γ energy	[300 MeV, 3 GeV]	Both the two photons' energies lie within this range
γ hit position	[150 mm, 850 mm]	The x and y positions should be larger than the square of 150 mm side, and the radius smaller than 850 mm.
Minimum distance between 2 γs	>150 mm	
δ t for extra photon evens	>3 ns	
Projection angle between the two tracks	>150°	
K_L^0 decay z	[3000, 5000]	

6.4.2 Systematic Uncertainties

The same method is applied as the other two modes. The total systematic uncertainty is 2.3% and the biggest contribution comes from MB (5.85%) where the high energy is not well simulated.

6.4.3 Conclusion

Table 6.7 concludes the K_L^0 flux from $K_L^0 \to \gamma\gamma$ mode.

Table 6.7: K_L^0 flux measurement from $K_L^0 \to \gamma\gamma$ mode

| Trigger Mode	Number of signals	Acceptance	Flux
Minimum biased	636.48±25.23	$(5.87\pm0.03)\times 10^{-7}$	$(3.26 \pm 0.13_{stat} \pm 1.25_{sys}) \times 10^{11}$
Normalization	$(5.87\pm0.08)\times 10^3$	$(5.87\pm0.03)\times 10^{-7}$	$(3.00 \pm 0.04_{stat} \pm 0.07_{sys}) \times 10^{11}$

Figure 6.22: The systematic uncertainty for $K_L^0 \to \gamma\gamma$ mode.(a) The exclusive acceptance of the kinematic cuts. (b) The fractional difference of the kinematic cuts. (c) The exclusive acceptance of the veto cuts. (d) The fractional difference of the veto cuts.
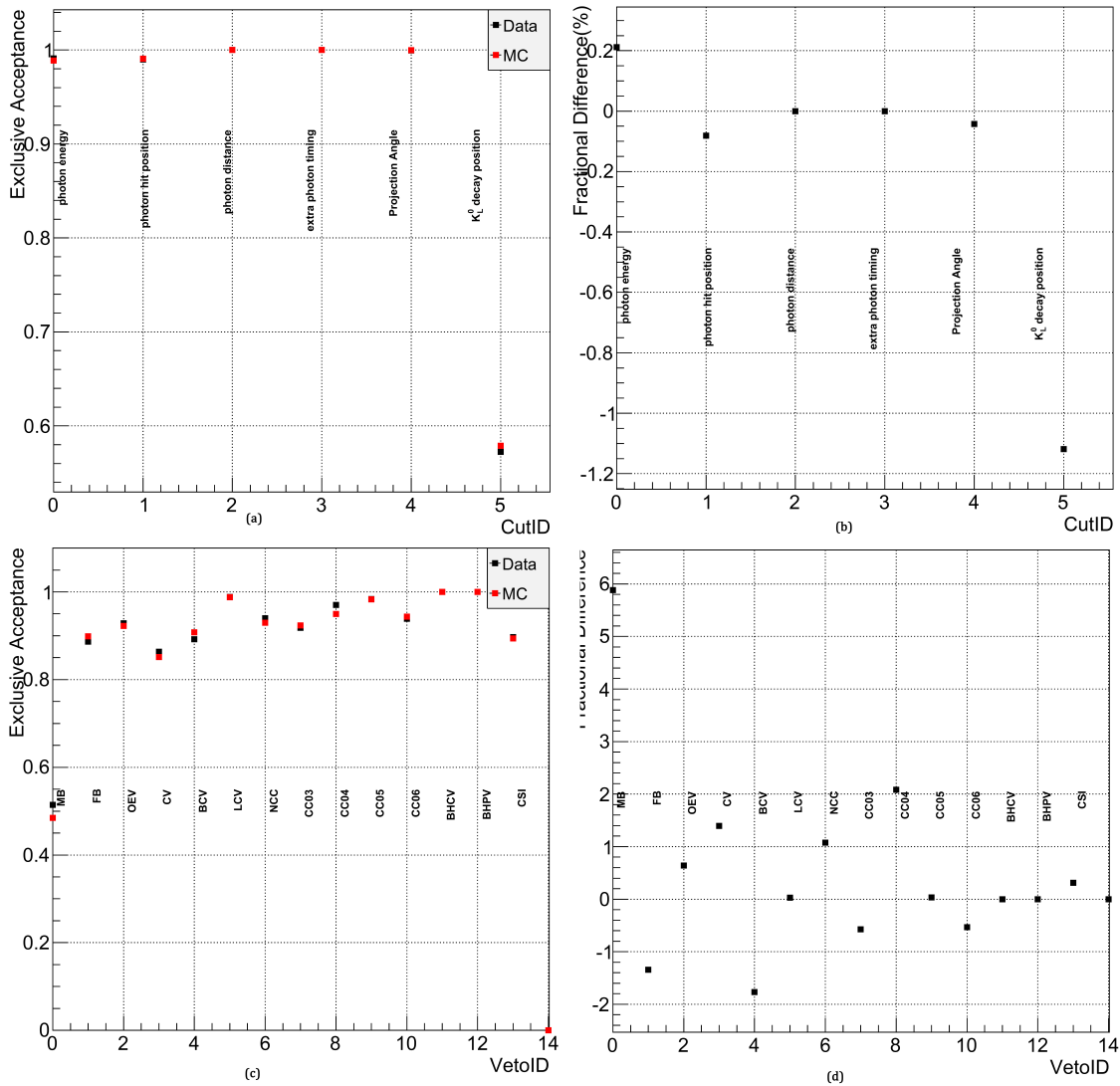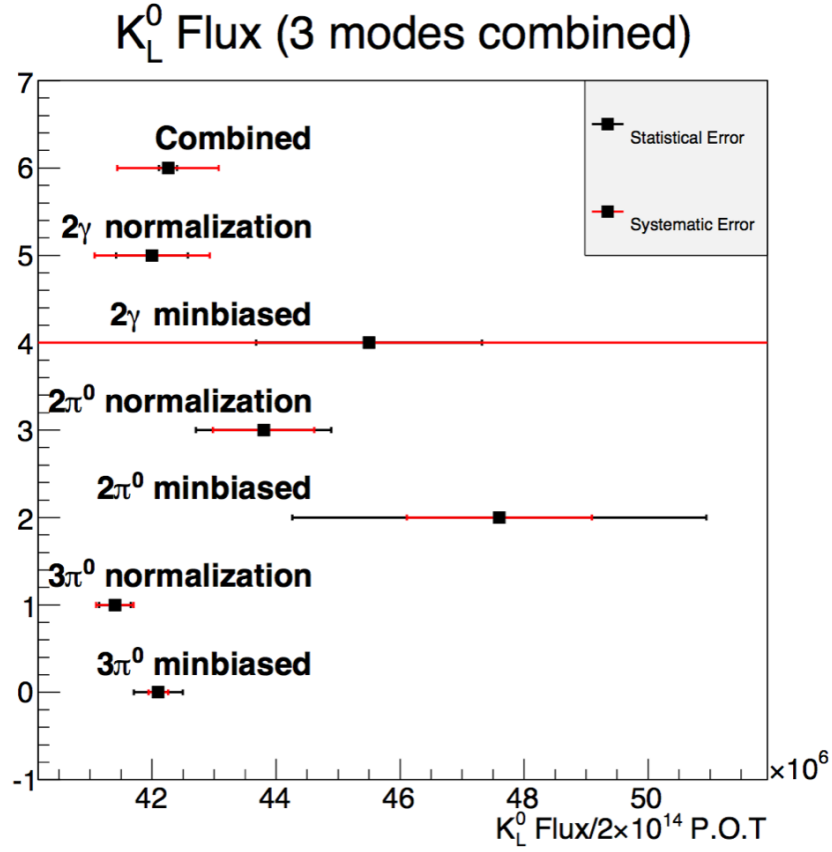
Figure 6.23: The K_L^0 flux measurement with all the three modes and two trigger modes.

6.5 Conclusion

Figure 6.23 concludes the study of this chapter. The K_L^0 yield is computed from 3 normalization modes and from 2 trigger sets. To combine the three modes, the flux is the mean of the 6 independent measurements weighted by their errors. The statistical errors is recalculated from all the data sets, and the systematic uncertainty equals the one used for $K_L^0 \rightarrow \pi^0\pi^0$ normalization modes, because they share the similar energies of the photons. The final number of K_L^0 generated at the target for the whole data set is $(6.02 \pm 0.28_{stat} \pm 0.88_{sys}) \times 10^{11}$.

CHAPTER VII

Event selection and Background

7.1 Blind Analysis

A blind analysis strategy is used to minimize unintentional cut bias. Here the procedures to implement blind analysis is described. In the first step, a signal box is defined according to the signal kinematics. In our case, the signal box is defined as the Kaon decay vertex between 3000mm and 5000mm downstream of FB front face, and transverse momentum of the π^0 between 130 MeV and 250 MeV. Afterwards, the 2-γ analysis is applied to all the data set using a slightly looser cut than the final physics. All events falling inside the signal box are blinded, that is they are removed from further analysis. In step three, we analyze using the blinded data and MC. By comparing the results outside the signal window, we want to fix the cuts, understand the sources of background and get an estimation of background falling inside the box. The final physics cuts are determined in this step. In the final step, we open the signal box, and measure the number of signal events.

7.2 Event Selection

Table 7.1 and 7.2 lists the cut conditions for event selection.

The meaning of photon energy cut, position cut, and distance cut are identical to

Table 7.1: Kinematic cuts for $K_L^0 \to \pi^0 \nu \bar{\nu}$ selection

γ energy	[100 MeV, 2 GeV]
γ position	[150 mm, 850 mm]
γ distance	>300 mm
γ energy ratio	>0.2
2 γ energy sum	>650 MeV
Eθ	>2500 MeV· degree
Cluster shape χ^2	<4.6
projection angle	<150 degree
CoE	>200 mm
cluster size	>4
cluster RMS	>10 mm
π^0 kinematic cut	see text
CsI single crystal veto	see text
minimum distance from dead ch	>53mm
kinematic NN	>0.67
cluster shape NN	>0.8
extra cluster timing	>± 10 ns
vertex time difference	<± 2ns

Table 7.2: Veto cuts for $K_L^0 \to \pi^0 \nu \bar{\nu}$ selection

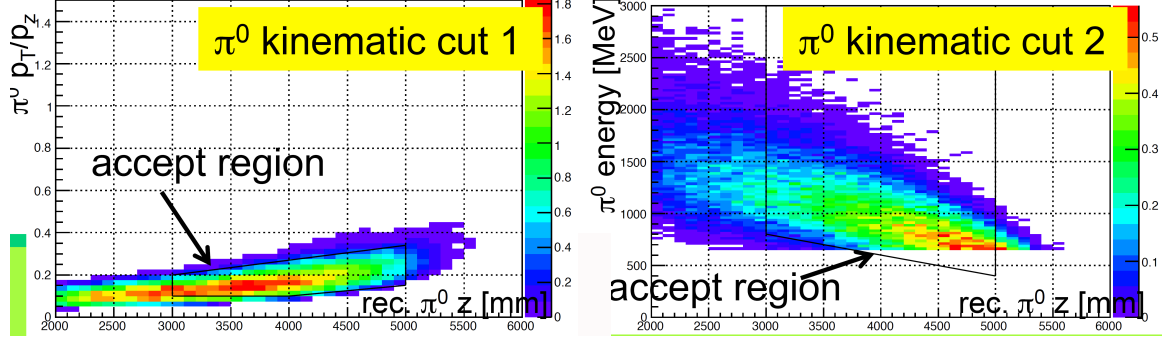| Detector	Veto Energy (MeV)	Veto Time Window (ns)
MB	2	60
FBAR	2	40
OEV	2	20
CV	0.2	80
BCV	1	60
LCV	0.6	30
NCC	2	40
CC03	3	30
CC04 Scintillator	1	30
CC04 CsI	3	30
CC05 (Scintillator)	1	30
CC05 (CsI)	3	30
CC06 (Scintillator)	1	30
CC06 (CsI)	3	30
BHCV	0.3	200
BHPV	3 (Coincident hits)	200

Figure 7.1: The π^0 kinematic cut

the normalization modes.

Eθ cut:

This cut is the production of photon energy and the deflection angle from beam direction (in degrees), which is used to enhance events with big transverse momentum.

Cluster shape χ^2 cut:

A cluster template is generated using MC, and the χ^2 is defined to compared the cluster under study with the template to remove merged clusters.

Cluster RMS cut:

The definition of cluster RMS is $\sqrt{\frac{\sum_i e_i d_i^2}{\sum_i e_i}}$, and e_i is the energy of each crystal and d_i is the distance between the crystal and cluster center. This cut is used to suppress merged clusters.

π^0 kinematic cut:

This cut's definition is plotted in Figure 7.1. This cut is to remove the neutron-CV interaction produced η background.

CsI single crystal veto:

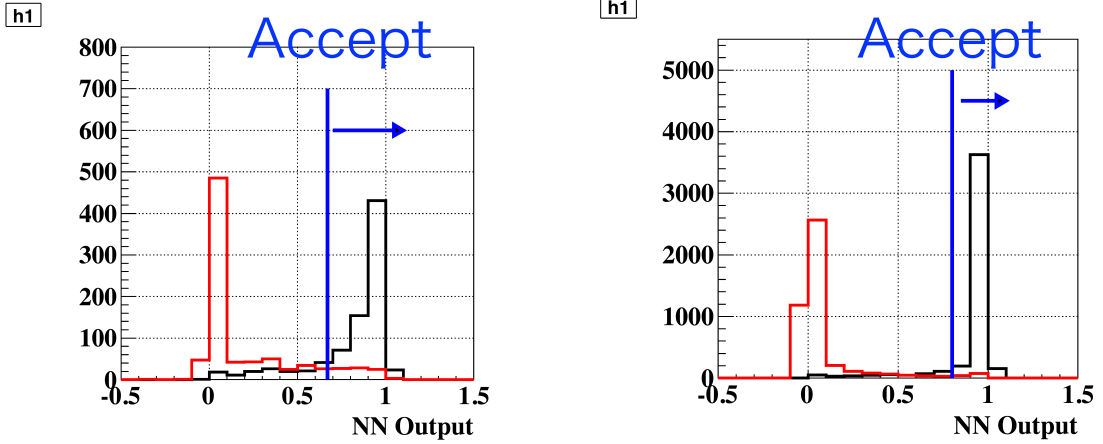This cut is cut on the single crystal energy depending its distance to the closest cluster satisfying

114

Figure 7.2: The output of Neural net trained by kinematic variables (left) and cluster shape variables (right).

$$E_{thre} = exp(3.73 - 0.0075 \times d)$$

$$= 10(E_{thres} > 10)$$

$$= 1.5(E_{thres} < 1.5)$$

Neural Network:

Neural network algorithm is trained to distinguish photon clusters and hadronic clusters. Five kinematic variables (positions,angles, energies,timings) and 12 cluster shape variables are the inputs to train the algorithm. And the background is reduced to 10%.

7.3   Background Sources

Background sources are three-fold: other K_L^0 decays, neutron interaction with detectors and beam line accidentals.
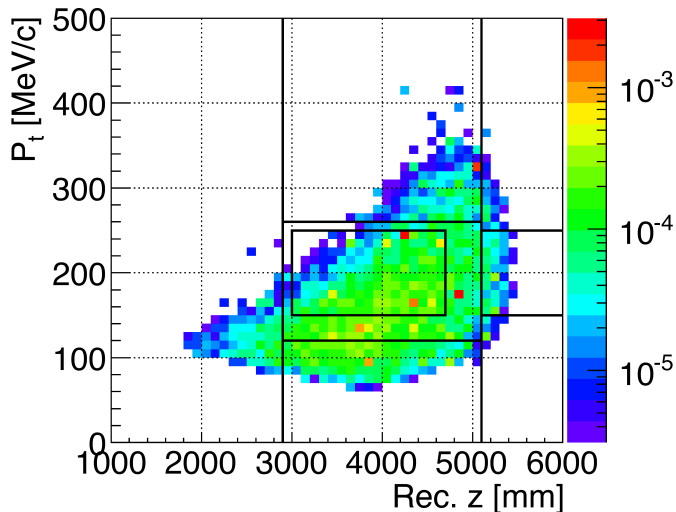
Figure 7.3: $K_L^0 \to \pi^0 \pi^0 \pi^0$ background

7.3.1 K_L Background

$K_L^0 \to \pi^0 \pi^0 \pi^0$: Here is the mechanism. One γ hits the CsI edge region, and is not detected by hitting dead material like the CsI cover support. And the other three γs with very small energy around 10 MeV scale, hit the FBAR or the MB and are not detected. To estimate this background, we rely on MC. A total of 4×10^9 K_L^0s are at beam exit, 10% equivalence of data statistics. 0.022 ± 0.004 events remain.

$K_L^0 \to \pi^0 \pi^0$:

Two of the four γs missed detection due to the MB inefficiency with 0.047 ± 0.033 events remaining in the signal box.

$K_L^0 \to \pi^+ \pi^- \pi^0$:

The mechanism of this background is: the two γs from the π^0 get detected by the CsI. But both charged πs hit the beam pipe and undergo hadronic interaction, therefore missing detection by CC05, CC06 and BHCV. To estimate the background from this source, 3×10^{10} K_L^0 are generated at beam line exit, which is the same statistics as the physics data. This is the main source of low-P_T background since the charged pions carry small P_T. The number of remaining events is 0.0016 ± 0.0016.
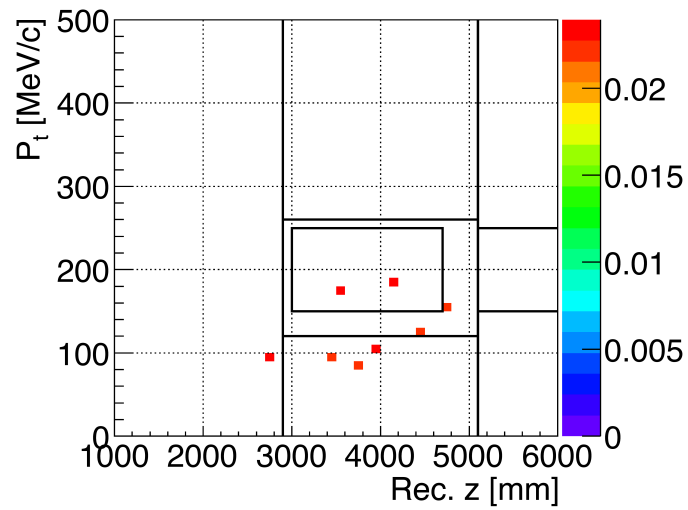
$K_L^0 \to 2\gamma$:

116

Figure 7.4: $K_L^0 \to \pi^0\pi^0$ background
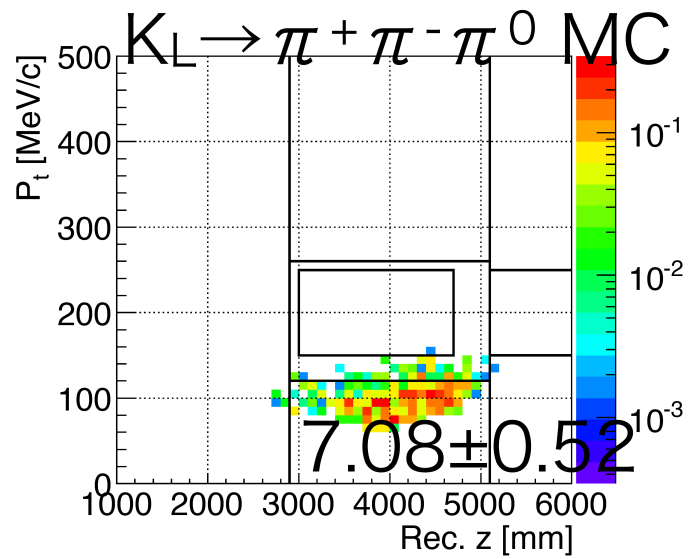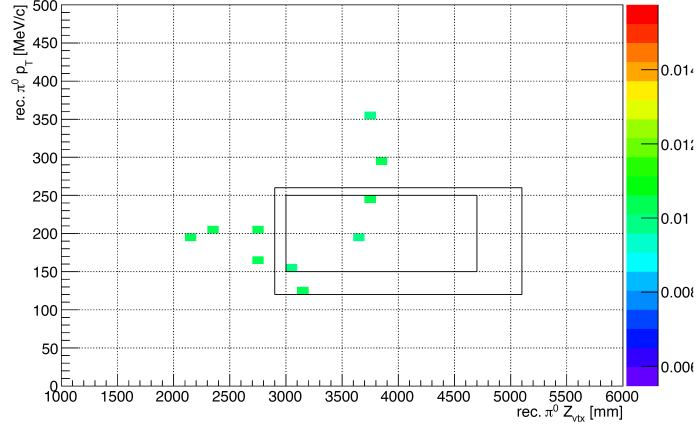

Figure 7.5: $K_L^0 \to \pi^+\pi^-\pi^0$ background

Figure 7.6: $K_L^0 \to \gamma\gamma$ background

The mechanism comes from K_L^0 which gains large P_T by being elastically scattered in the upstream vacuum window. 0.03 ± 0.018 events remain.

The total estimate of background from K_L^0 decays is 0.1476 events

7.3.2 Neutron Background

The halo neutrons in the beam interacts with NCC and contributes to the sideband in the low z region (1800mm-2900mm) as shown in Figure 7.7. The remaining number of events is 0.06 ± 0.06.

The other mechanism is that halo neutrons interact with CsI sequentially and generates two hadronic clusters(Figure 7.8). To remove this backgrond, Al target MC is used to train a set of neural network to separate photon clusters and hadron clusters. 0.18 ± 0.15 events remains and this is the biggest background.

7.3.3 Accidental Background

To minimize the background from beam line accidentals, a waveform analysis is used to be able to accurately determine the timing of detector signals. And beam line activities, whose timing is off, is removed. Timing is determined by fitting the pulse with parabola function.
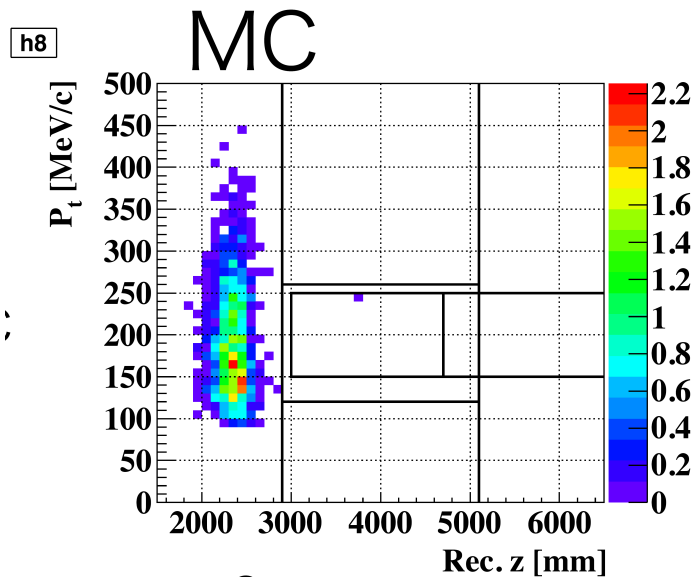
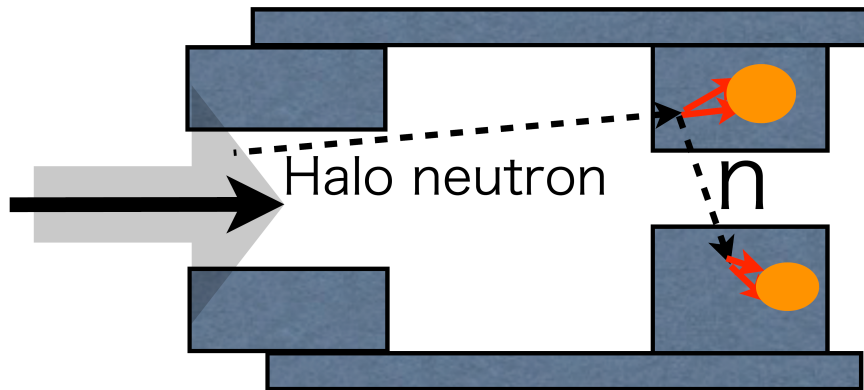Figure 7.7: Neutron background from interaction with NCC

Figure 7.8: The schematic event display of neutron background with interaction with CsI.
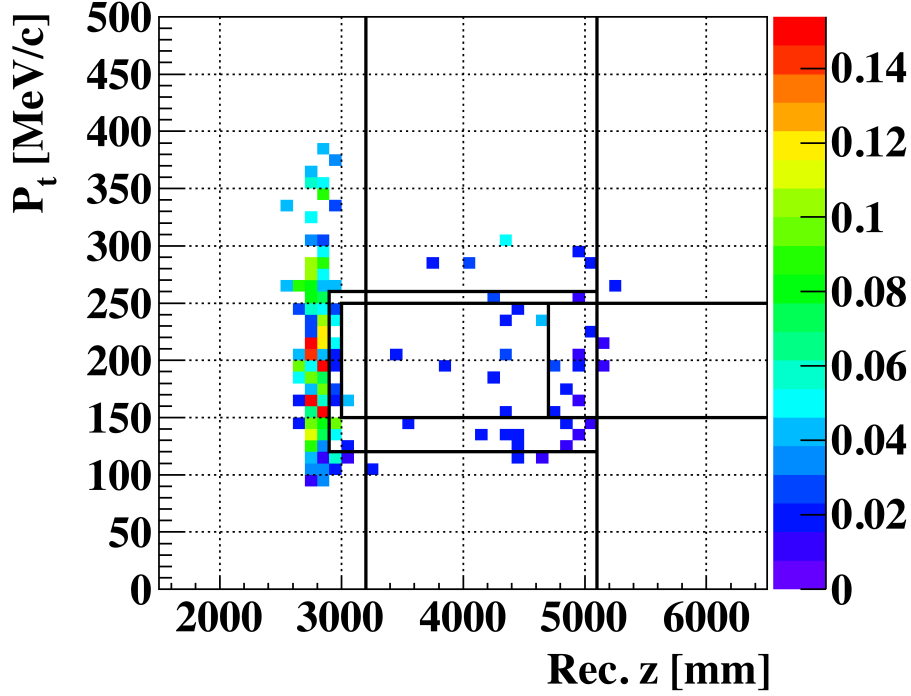
Figure 7.9: Neutron background from interaction with CsI

But there are cases when a big accidental pulse comes very close to the smaller but real pulse from the K_L^0 decay. Parabola function peeks the peak at the timing of the accidental pulse and if outside the timing window, is not vetoed (Figure 7.10). Due to this effect, the remaining events are 0.014 ± 0.014.

7.4 $K_L^0 \rightarrow (\pi^+ \mu^-)_{atom} \nu$

The $K_L^0 \rightarrow (\pi^+ \mu^-)_{atom} \nu$ decay, with the $(\pi^+ \mu^-)_{atom}$ preceding through the decay channel $(\pi^+ \mu^-)_{atom} \rightarrow \pi^0 \nu$, is a possible background source with the same final state and similar kinematics. This section will give a theoretical estimation of the contribution of this background. $K\mu3$ decay with the muon captured by charged pion in the $(\pi^+ \mu^-)_{atom}$ bound state has a branching fraction of 1.05×10^{-7}. The rate of $(\pi^+ \mu^-)_{atom}$ decay through $(\pi^+ \mu^-)_{atom} \rightarrow \pi^0 \nu$ channel is not calculated in literature, which will be the main effort of this section. The total rate of $K_L^0 \rightarrow \pi^0 \nu \bar{\nu}$ $(through (\pi^+ \mu^-)_{atom})$ will be a simple multiplication of the two numbers.
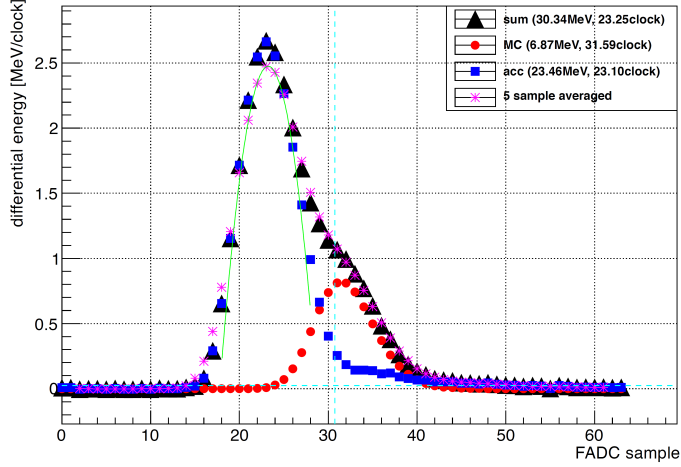
Figure 7.10: The example of the pulse shape of an accidental pulse overlaid with a smaller true pulse whose timing is shifted.

Figure. 7.11 shows the Feynman diagram of $(\pi^+\mu^-)_{atom} \to \pi^0\nu$ through weak tree level diagram. The amplitude of the diagram has the simple V-A form

$$M = \frac{G_F}{\sqrt{2}} V_{ud} [\bar{\nu}(p_4)\gamma_\mu(1-\gamma^5)\mu(p_2)] < \pi^0|j^\mu|\pi^+ > \psi_{\pi\mu}(0) \qquad (7.1)$$

where G_F is the Fermi constant, V_{ud} is the CKM matrix element, and $\psi_{\pi\mu}(0)$ is the wave function of the $(\pi^+\mu^-)_{atom}$ at origin with assumption that the nucleus has small size.

The explicit form of element $< \pi^0|j^\mu|\pi^+ >$ can be expressed as

$$< \pi^0|j^\mu|\pi^+ >= [F_1(q^2)(p_1^\mu + p_3^\mu) + F_2(q^2)(p_3^\mu - p_1^\mu)]e^{-iq\cdot x}[\phi'^\dagger I_3\phi] \qquad (7.2)$$

considering that the only kinematic vectorial variables involved are p_1^μ and p_3^μ. F_1 and F_2 are form factors of π^+ and π^0 to be determined shortly.

Using the conserved vector current hypothesis that $\frac{\partial j^\mu}{\partial x^\mu} = 0$, we have $F_1(q^2)(p_1^2 - p_3^2) + F_2(q^2)(p_3 - p_1)^2 = 0$. The closeness of π^+ and π^0 mass $p_1^2 \approx p_3^2$ enables us to
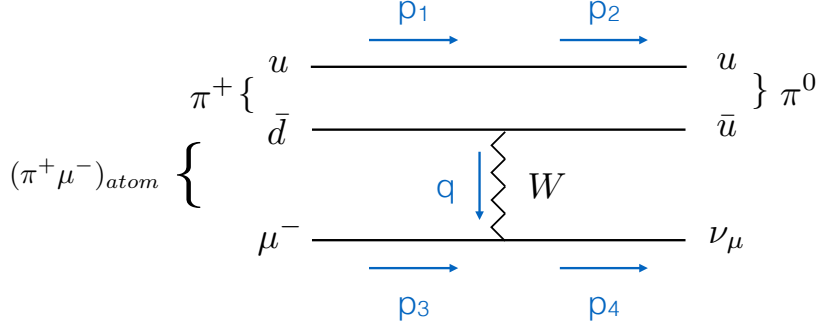
121

Figure 7.11: The tree level Feynman diagram of $(\pi^+\mu^-)_{atom} \to \pi^0\nu$.

safely assure $F_2(p^2) = 0$. Equation. 7.2 then is simplified as

$$< \pi^0|j^\mu|\pi^+ >= F_1(q^2)(p_1^\mu + p_3^\mu)e^{-iq\cdot x}[\phi'^\dagger I_3\phi] \tag{7.3}$$

The next step is to compute the isospin component $\phi'^\dagger I_3\phi$, which is an obvious $\sqrt{2}$, where

$$\phi' \to \pi^0, \phi \to \pi^+, and \ I_3 = \begin{pmatrix} 1 & 0 & 0 \\ 0 & 0 & 0 \\ 0 & 0 & -1 \end{pmatrix}$$

In the limit of $q^2 \to 0$, $F_1 \to 1$, and the matrix element becomes

$$M = G_F V_{ud}\psi_{\pi\mu}(0)[\bar{\nu}(p_4)\gamma_\mu(1 - \gamma^5)\bar{\mu}(p_2)](p_1^\mu + p_3^\mu) \tag{7.4}$$

The detailed calculation of $< |M| >^2$ is performed in Appendix D, and here we

122

just cite the result

$$< |M|^2 > = 8G_F^2 V_{ud}^2 |\psi_{\pi\mu}(0)|^2 m_{\mu^-} |p|(m_{\pi^+} + E_{\pi^0} + |p|)^2 \tag{7.5}$$

Next step is to compute the decay rate using Fermi golden rule.

$$\begin{aligned}
\Gamma &= \frac{1}{8m_a} \int |M|^2 (2\pi)^4 \delta^4(p_1 - p_3 - p_4) \frac{d^3 p_3}{(2\pi)^3 E_3} \frac{d^3 p_4}{(2\pi)^3 E_4} \\
&= \frac{G_F^2 V_{ud}^2 |\psi_{\pi\mu}(0)|^2 m_{\mu^-} (m_a - m_{\pi^+})^2 E_{\pi^0}}{\pi m_a}
\end{aligned} \tag{7.6}$$

where $m_a = m_{\pi^+} + m_{\mu^-}$.

Now it's time to plug in with real numbers: $G_F = 1.166 \times 10^{-5} GeV$, $V_{ud} = 0.97$, $m_{\mu^-} = 105 MeV$, $m_a = 245 MeV$, $E_{\pi^0} = \sqrt{|p|^2 + m_{\pi^0}^2} = 159.7 MeV$. Consider the ground state of $(\pi^+ \mu^-)_{atom}$ wave function:

$$\psi_{\pi\mu}(r) = R_{10} = \frac{2}{a^{3/2}} exp(-\frac{r}{a}) \tag{7.7}$$

where $a = \frac{1}{zm_r\alpha}$ is the Bohr radius. We have $|\psi_{\pi\mu}(0)|^2 = \frac{4}{a} = 4(zm_r\alpha)^3$, where $m_r = \frac{m_{\pi^+} m_{\mu^-}}{m_{\pi^+} + m_{\mu^-}}$ is the reduced mass. Plugging in all the numbers into equation gives $\Gamma = 0.35 s^{-1}$.

So far, we can make the conclusion that the decay rate of $(\pi^+ \mu^-)_{atom} \to \pi^0 \nu$ is 3 orders of magnitude slower than when it can beat the SM branching ratio of $K_L^0 \to \pi^0 \nu \bar{\nu}$ that this background source can be safely neglected.

7.5   Conclusion

Figure 7.12 concludes the side-band of all the combined background sources. The low P_t background comes from $K_L^0 \to \pi^+ \pi^- \pi^0$. The high P_t and downstream background are neutron-CsI hadronic interaction events. The upstream background are mainly from neutron-NCC interaction events. The estimated events inside the sig-
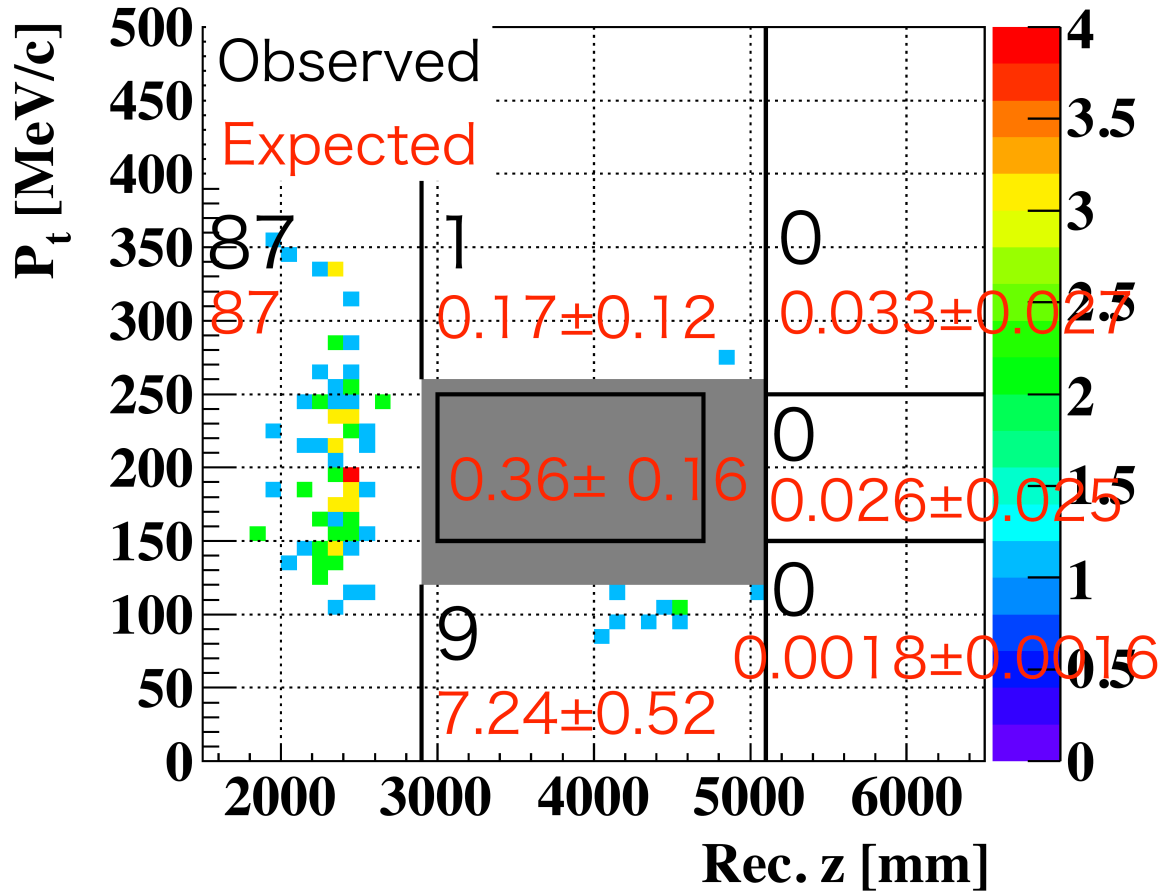
Figure 7.12: The remaining events after all the cuts displayed in the P_t vs z plot.

nal box is 0.36 ± 0.16. Also the new source of background $K_L^0 \rightarrow (\pi^+\mu^-)_{atom}\nu$ is theoretically studied, and can be neglected.

CHAPTER VIII

Conclusion

8.1 Opening the box

The signal box is opened and one event is found inside the box, whereas the expected value from background is 0.36 ± 0.16.

8.2 Single Event Sensitivity

As calculated in chapter 6, the number of K_L^0s generated at the target is $(6.02 \pm 0.28 \pm 0.88) \times 10^{11}$.

From $K_L^0 \to \pi^0 \nu \bar{\nu}$ MC, the acceptance is

$$A_{signal} = (1.28 \pm 0.01_{stat}) \times 10^{-4} \tag{8.1}$$

The single event sensitivity is therefore

$$S.E.S = \frac{1}{N_{K_L^0} \times A_{signal}}$$
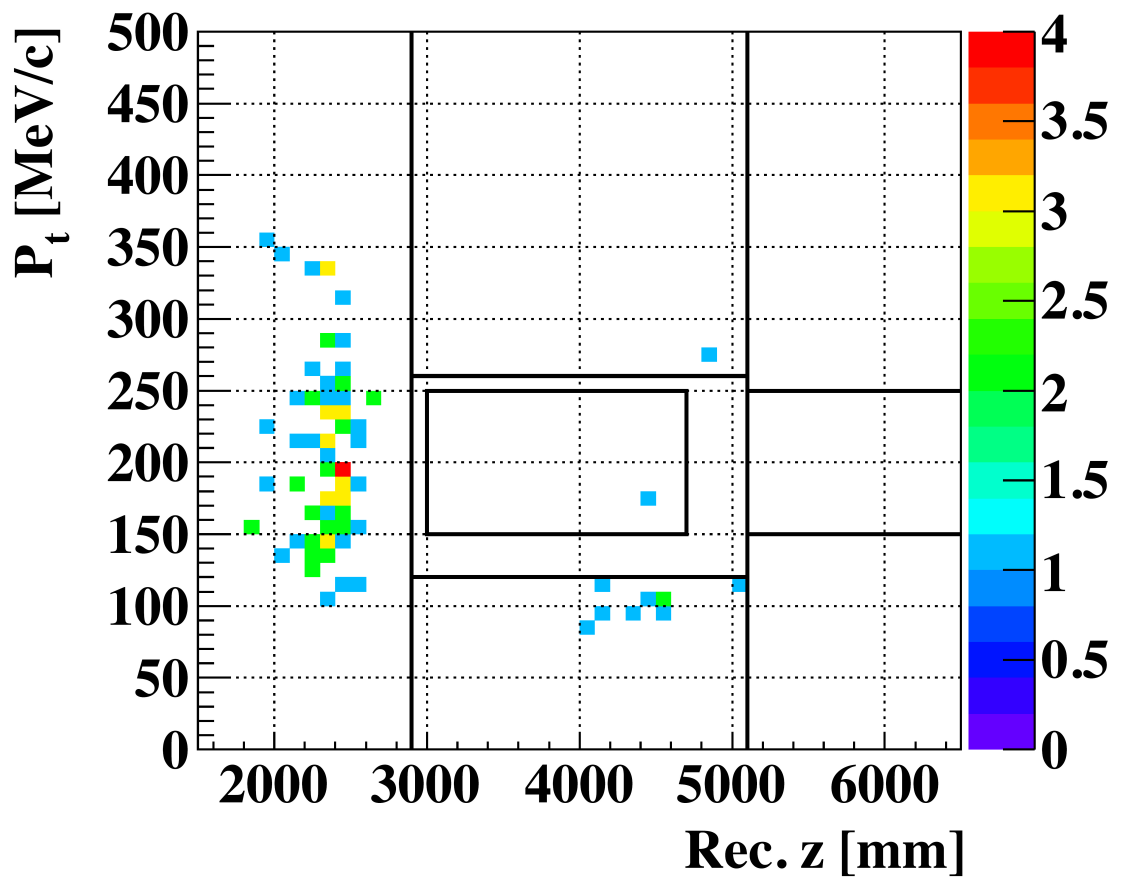$$= (1.29 \pm 0.06_{stat} \pm 0.19_{sys}) \times 10^{-9} \tag{8.2}$$

Figure 8.1: Open signal box.

8.3 Final Result

Assuming the remaining event is background, the upper limit of the branching ratio is 5.03×10^{-8} using Poisson distribution. The E391a result is $< 2.6 \times 10^{-8}$ and 90% C.L.

8.4 Future Improvements of the Experiment

There are several perspective upgrades of the experiment. The MB detector will be upgraded by inserting a new *Inner Barrel* detector with $5X_0$ thickness. The inefficiency is expected to be reduced by a factor of 10 for 100 MeV photons.

More BHPV will be installed to the 25 modules as originally designed to reach the inefficiency of 10^{-3} at 1 GeV.

The BPCV will be redesigned using gas chamber to reduce the amount of the materials in the beam line and thus reduce counting rate.

A beam pipe charge veto is proposed by putting a layer of scintillators around the beam pipe around CC05 and CC06 to suppress $K_L^0 \to \pi^+\pi^-\pi^0$ background.

As to halo neutron suppression, a beam profile monitor is proposed to gaurantee the alignment between the two collimators.

At the same time, the DAQ will be upgraded to handle higher beam power with little dead time.

APPENDICES

APPENDIX A

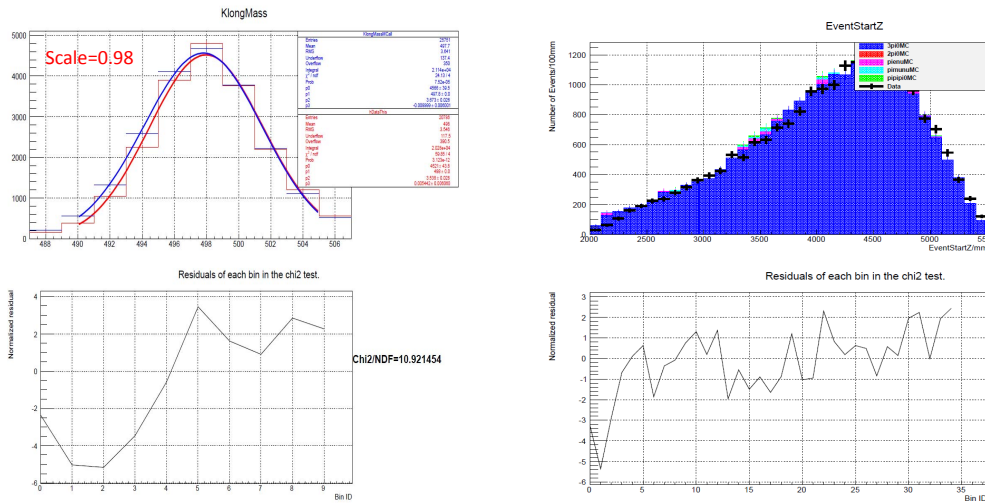# The sensitivity of K_L^0 mass to CsI energy scale

Figure A.1: The K_L^0 mass distribution of data (red) and blue (MC) for energy scale 0.98 (left). The K_L^0 decay z distribution (right). The botton two histograms a residules for each bin.
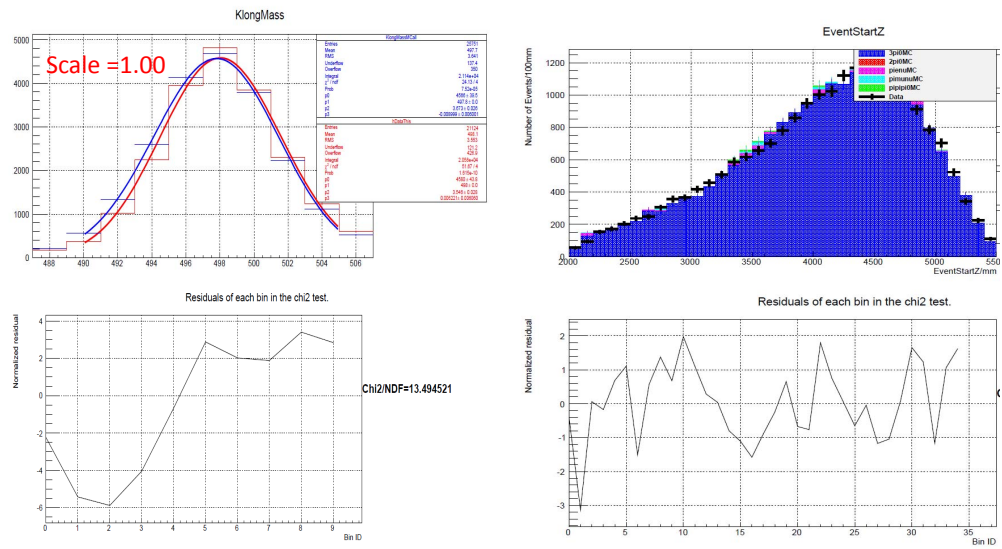
Figure A.2: The K_L^0 mass distribution of data (red) and blue (MC) for energy scale 1 (left). The K_L^0 decay z distribution (right). The botton two histograms a residules for each bin.
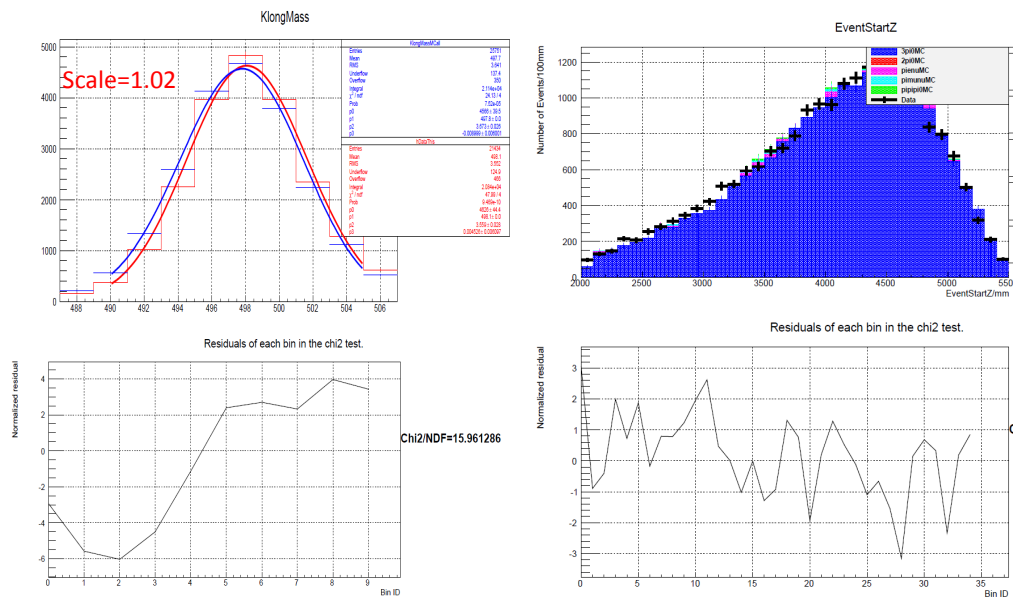
Figure A.3: The K_L^0 mass distribution of data (red) and blue (MC) for energy scale 1.02 (left). The K_L^0 decay z distribution (right). The botton two histograms a residules for each bin.

APPENDIX B

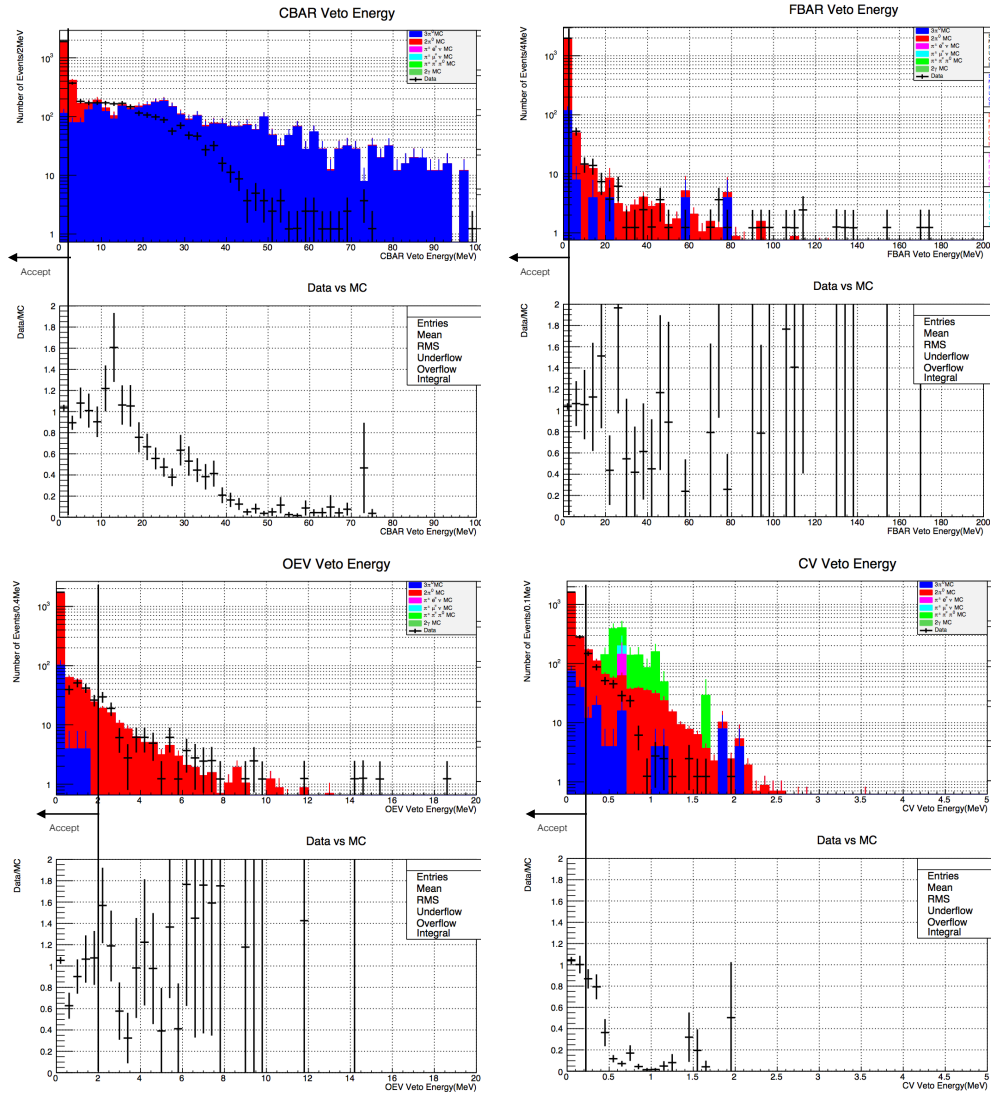# The veto cut distribution for $K_L^0 \to \pi^0\pi^0$ mode

Figure B.1: The energy distribution of the veto detectors. All the kinematic cuts are applied, and all the other veto cuts than the veto under study is applied.
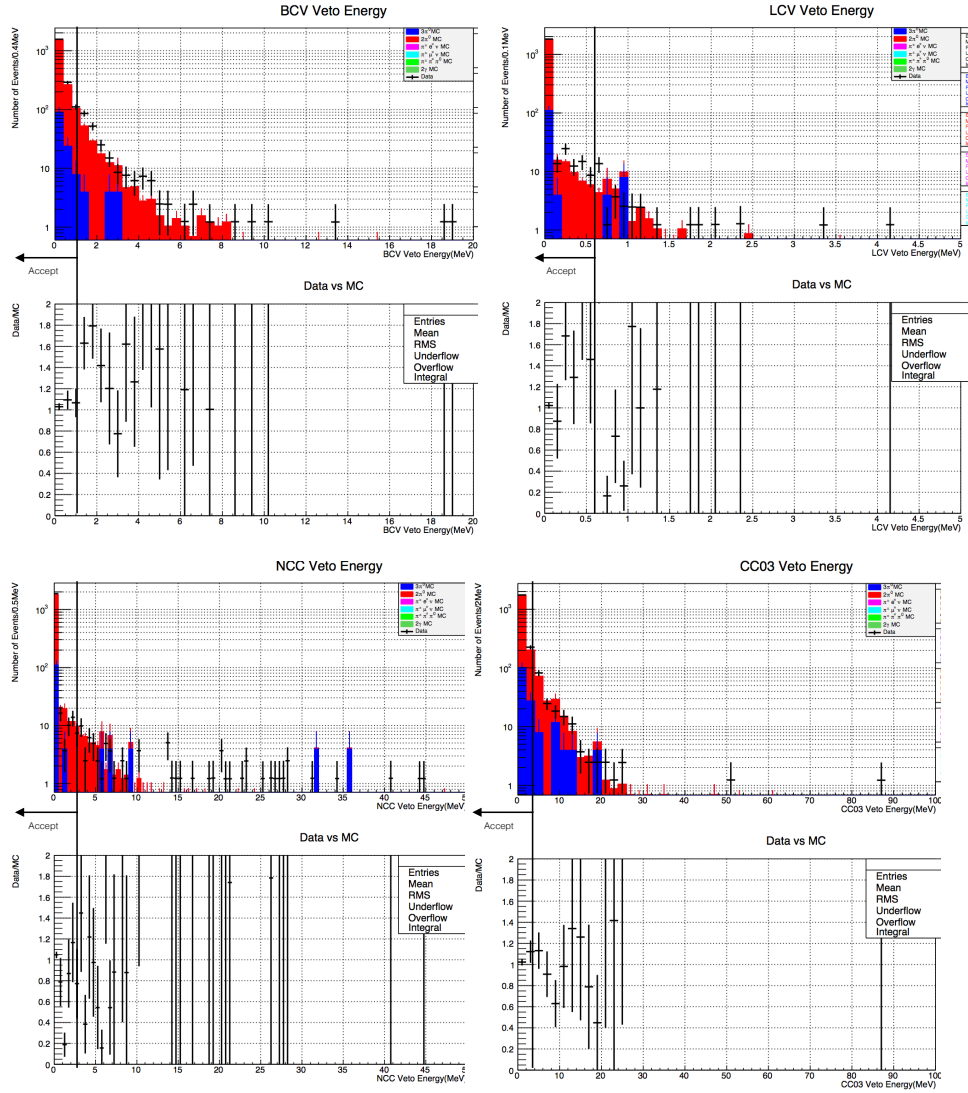
Figure B.2: The energy distribution of the veto detectors. All the kinematic cuts are applied, and all the other veto cuts than the veto under study is applied.

Figure B.3: The energy distribution of the veto detectors. All the kinematic cuts are applied, and all the other veto cuts than the veto under study is applied.
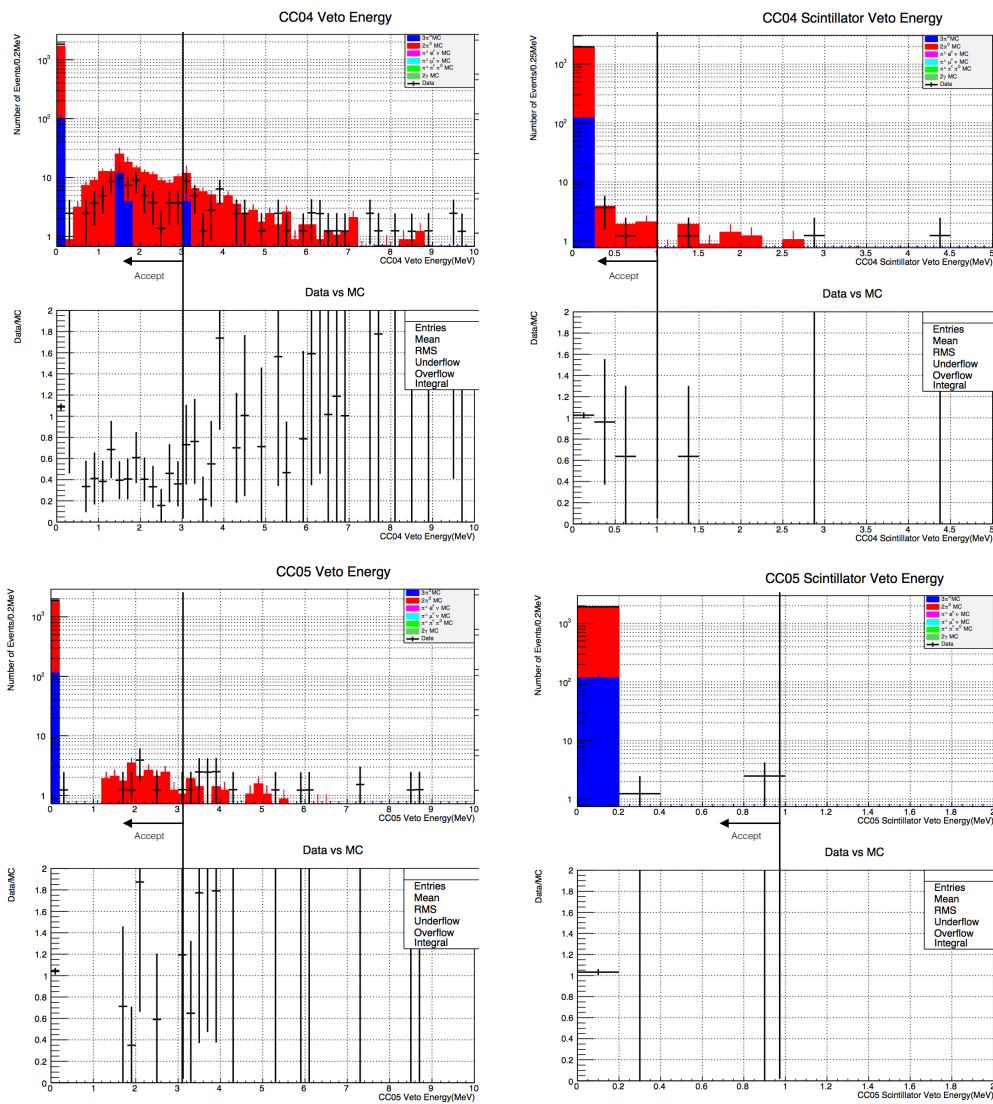
Figure B.4: The energy distribution of the veto detectors. All the kinematic cuts are applied, and all the other veto cuts than the veto under study is applied.

137

APPENDIX C

$K_L^0 \to \gamma\gamma$ analysis for normalization triggers

Figure C.1: The distribution of the kinematic variables. All the veto cuts are applied, and all the other kinematic cuts than the cut under study are applied.
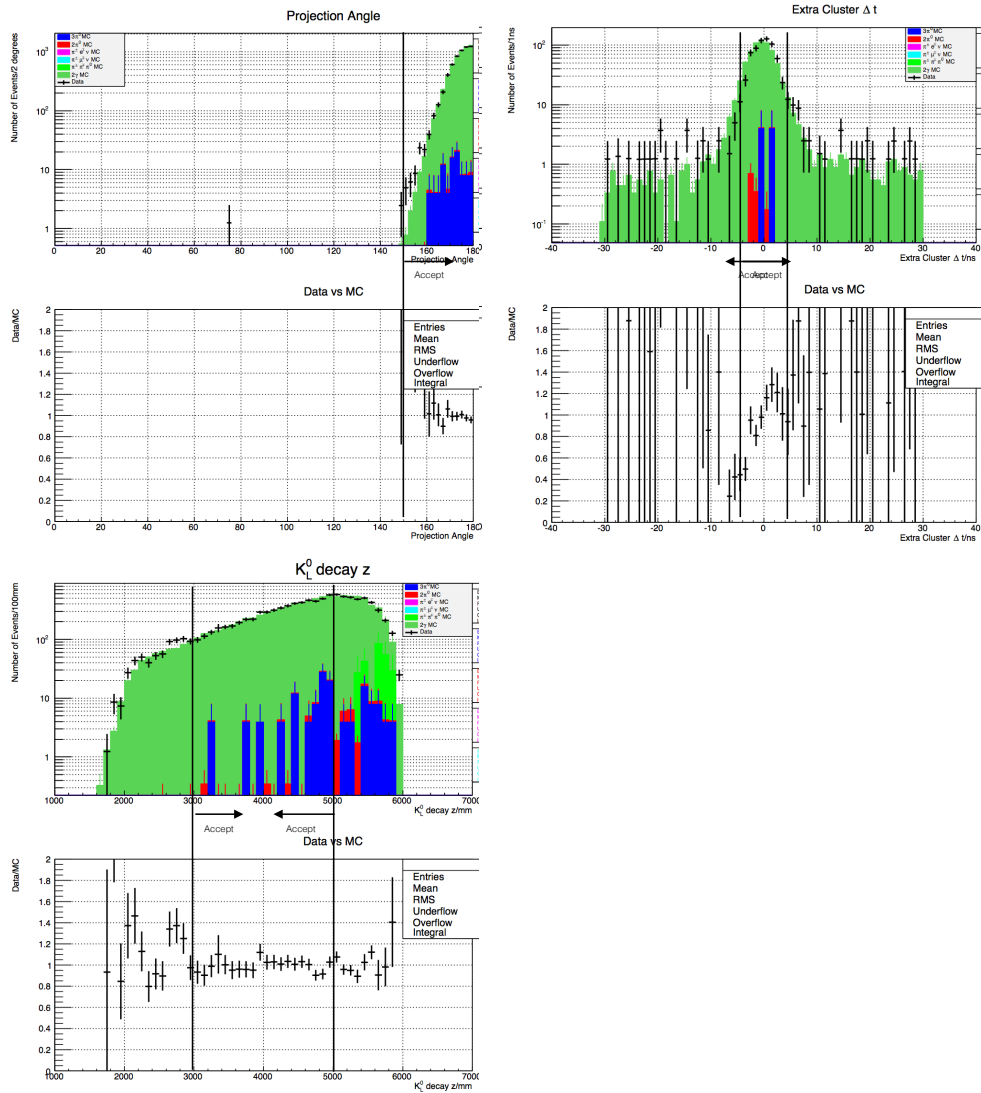
Figure C.2: The distribution of the kinematic variables. All the veto cuts are applied, and all the other kinematic cuts than the cut under study are applied.
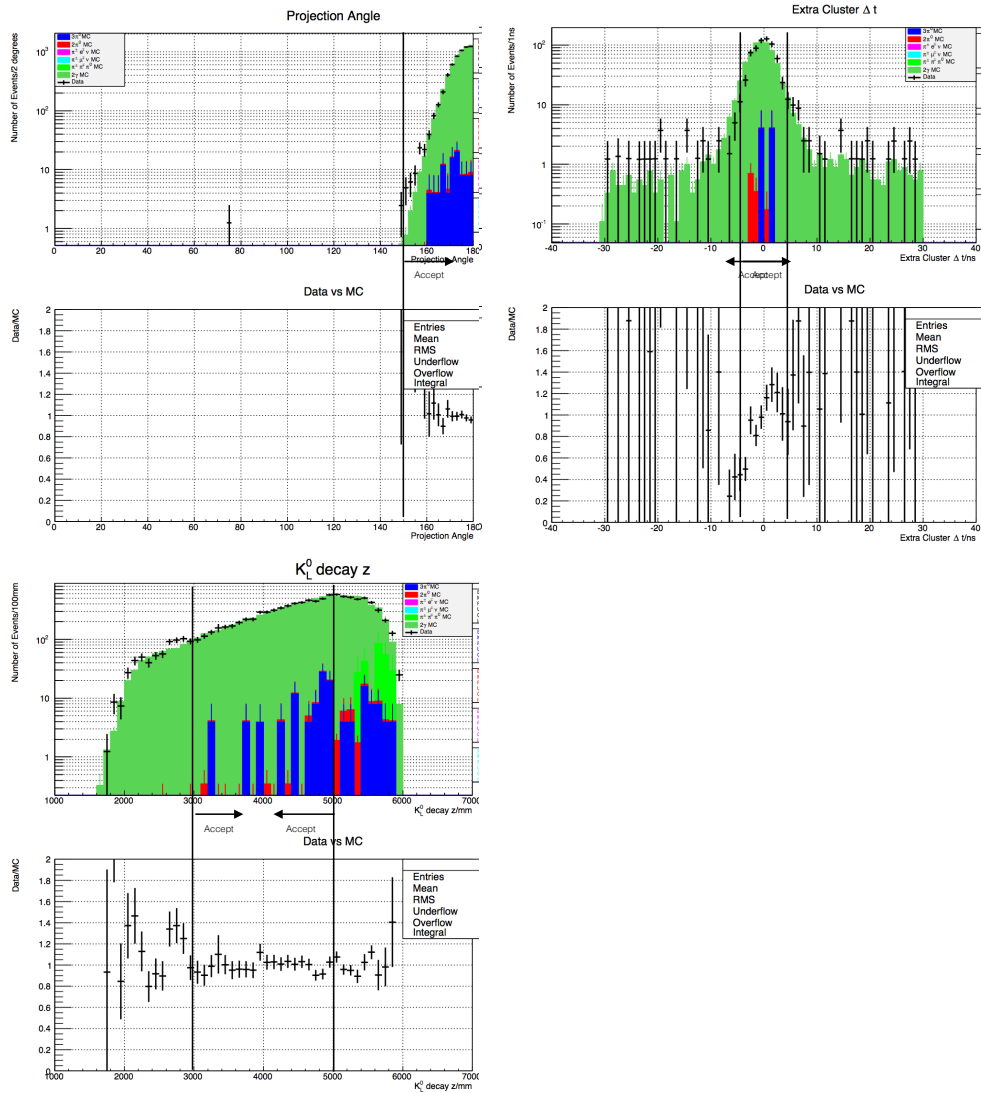
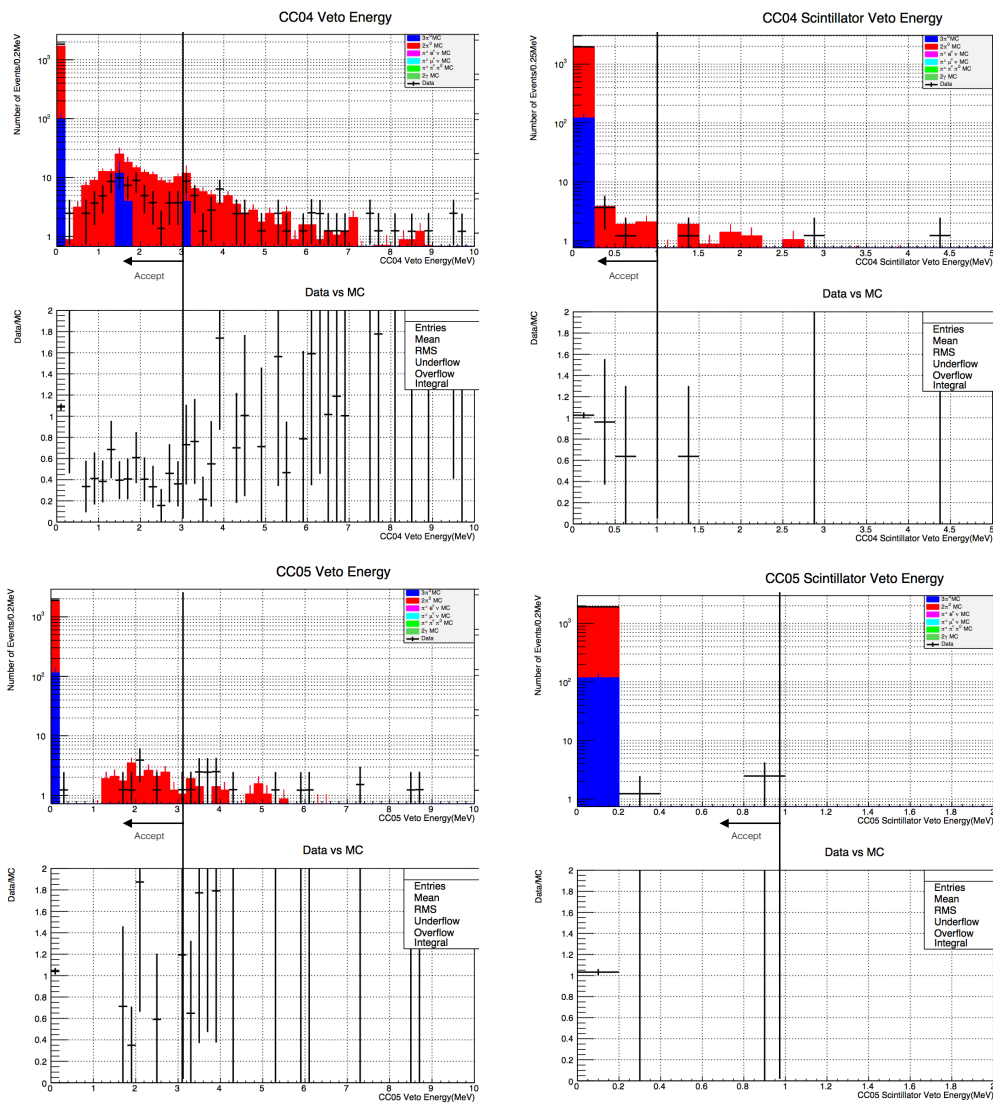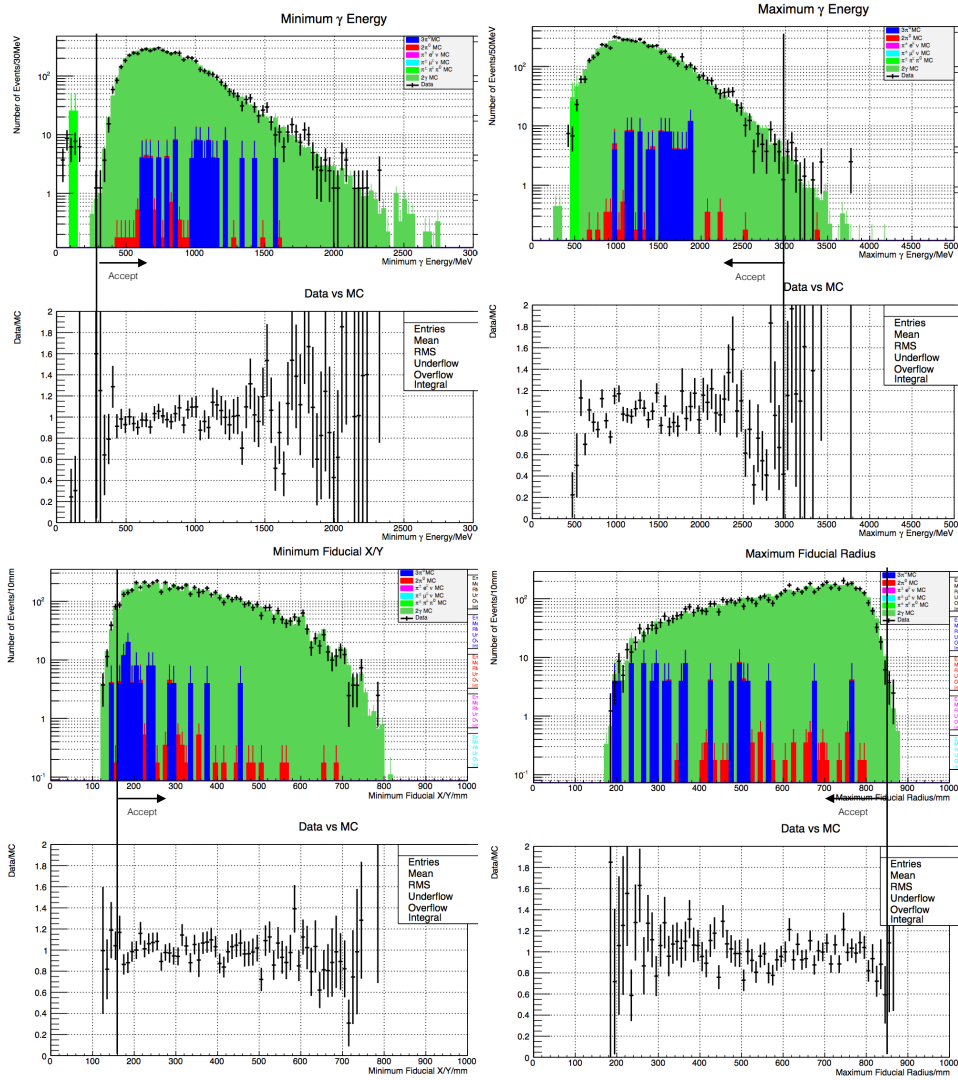Figure C.3: The energy distribution of the veto detectors. All the kinematic cuts are applied, and all the other veto cuts than the veto under study are applied.

Figure C.4: The energy distribution of the veto detectors. All the kinematic cuts are applied, and all the other veto cuts than the veto under study are applied.

Figure C.5: The energy distribution of the veto detectors. All the kinematic cuts are applied, and all the other veto cuts than the veto under study are applied.

Figure C.6: The energy distribution of the veto detectors. All the kinematic cuts are applied, and all the other veto cuts than the veto under study are applied.
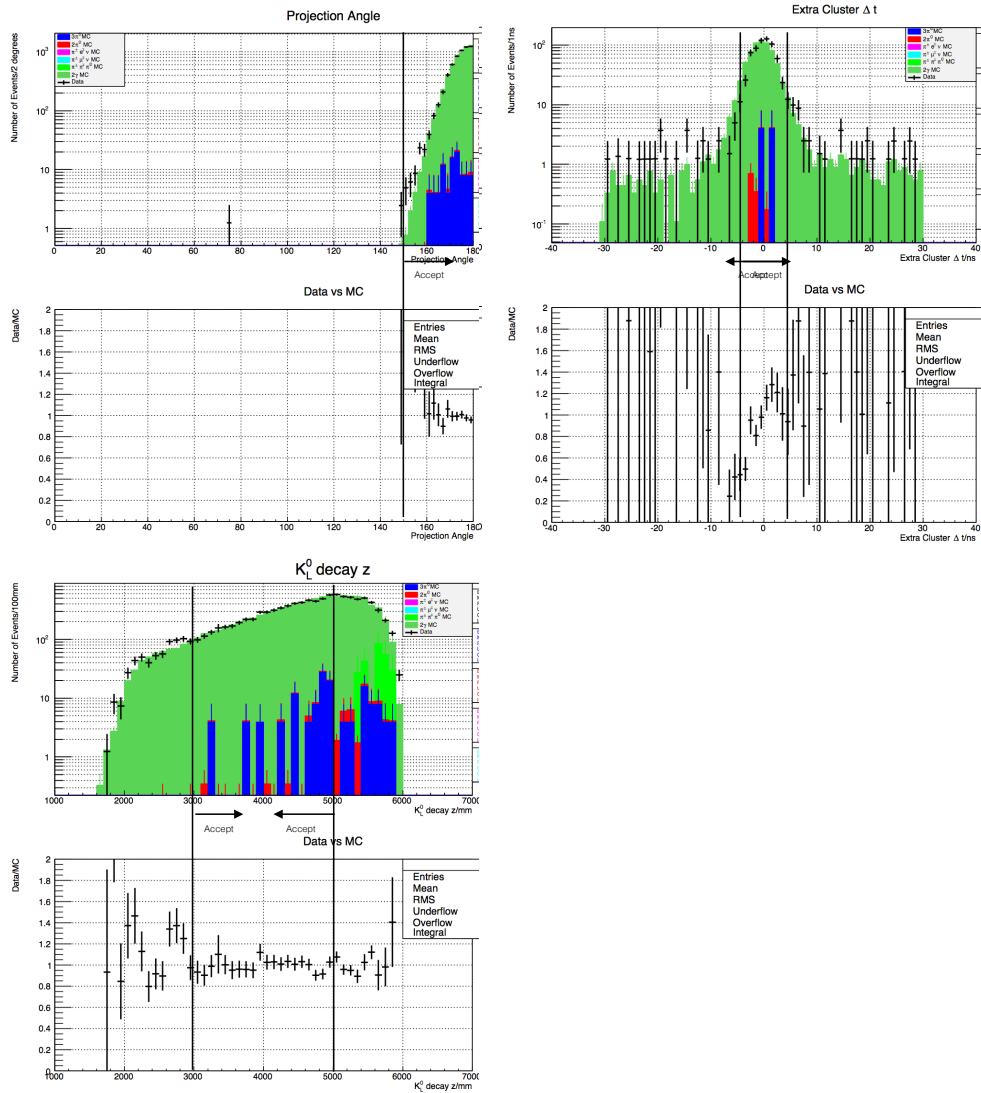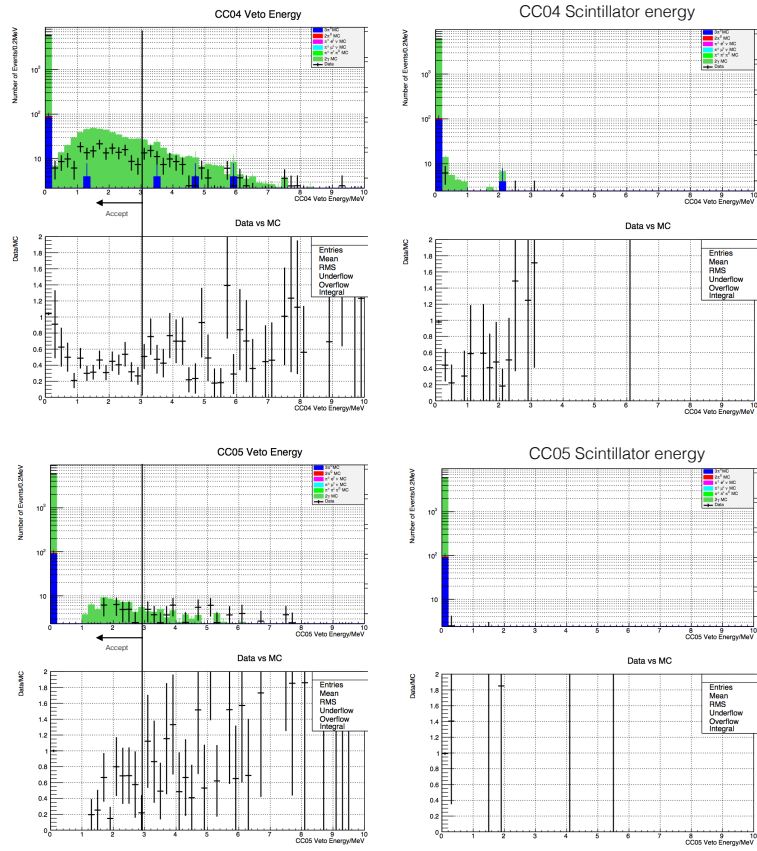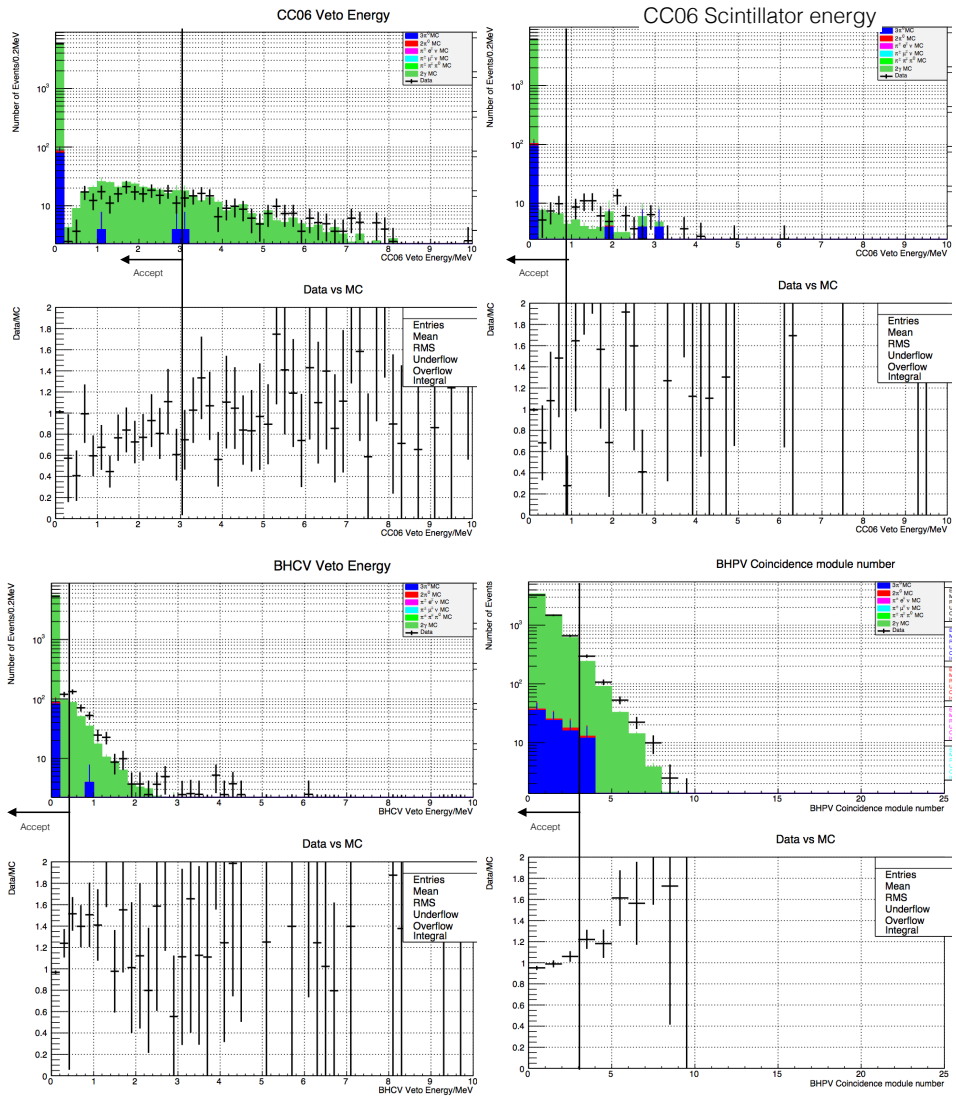
APPENDIX D

Calculation of $< |M|^2 >$ of $(\pi^+\mu^-)_{atom}$ decay rate

This chapter will describe the calculation of $< |M| >^2$ of $(\pi^+\mu^-)_{atom}$ decay in section 7.4. The notations used here can be found therein. As of equation 7.4, the matrix element was expressed as

$$M = G_F V_{ud} \psi_{\pi\mu}(0)[\bar{\nu}(p_4)\gamma_\mu(1 - \gamma^5)\bar{\mu}(p_2)](p_1^\mu + p_3^\mu) \tag{D.1}$$

In the above equation, G_F is the Fermi constant, V_{ud} is the CKM matrix element, and $\psi_{\pi\mu}(0)$ is the wave function at origin.

We begin with simplifying $p_1^\mu + p_3^\mu$. In $(\pi^+\mu^-)_{atom}$ Center-of-Mass (CM) frame, we have the momenta in game expressed as

$$p_1^\mu = (m_{\pi^+}, \vec{0}), \ p_2^\mu = (m_{\mu^-}, \vec{0}) \tag{D.2}$$

$$p_3^\mu = (E_{\pi^0}, \vec{p}), \ p_4^\mu = (|p|, -\vec{p}) \tag{D.3}$$

in which $\vec{p}$ is the only unknown. The conservation of momentum constraint $p_1^\mu + p_2^\mu = p_3^\mu + p_4^\mu$ gives

$$|p| = \frac{m_{(\pi\mu)_{atom}}^2 - m_{\pi^0}^2}{2m_{(\pi\mu)_{atom}}} \tag{D.4}$$

145

where $m_{(\pi\mu)_{atom}} = m_{\pi^+} + m_{\mu^-}$. Therefore,

$$p_1^\mu + p_3^\mu = (m_{\pi^+} + E_{\pi^0}, \vec{p}) \equiv p'^\mu \qquad \text{(D.5)}$$

So,

$$< |M|^2 > = G_F^2 V_{ud}^2 |\psi_{\pi\mu}(0)|^2 p'^\mu p'^\nu Tr[\not{p}_4\gamma_\mu(1-\gamma^5)(\not{p}_2 - m_{\mu^-})\gamma_\nu(1-\gamma^5)] \qquad \text{(D.6)}$$

Recall the γ matrix properties

$$(1 - \gamma^5)\gamma_\mu = \gamma_\mu(1 + \gamma^5) \qquad \text{(D.7)}$$

$$\left(\frac{1 - \gamma^5}{2}\right)^2 = \frac{1 - \gamma^5}{2}, \quad and \qquad \text{(D.8)}$$

$$(1 - \gamma^5)(1 + \gamma^5) = 0 \qquad \text{(D.9)}$$

we have

$$Tr[\not{p}_4\gamma_\mu(1-\gamma^5)(\not{p}_2 - m_{\mu^-})\gamma_\nu(1-\gamma^5)] = 2\{Tr[\not{p}_4\gamma_\mu \not{p}_2\gamma_\nu] - Tr[\not{p}_4\gamma_\mu \not{p}_2\gamma_\nu\gamma^5]\} \qquad \text{(D.10)}$$

where the m_{μ^-} terms are vanished. Note further that

$$Tr[\not{p}_4\gamma_\mu \not{p}_2\gamma_\nu] = p_4^\lambda p_2^\sigma Tr[\gamma_\lambda\gamma_\mu\gamma_\sigma\gamma_\nu]$$

$$= 4p_4^\lambda p_2^\sigma(g^{\lambda\mu}g^{\sigma\nu} - g^{\lambda\sigma}g^{\mu\nu} + g^{\lambda\gamma}g^{\mu\sigma})$$

$$and\ that\ Tr[\not{p}_4\gamma_\mu \not{p}_2\gamma_\nu\gamma^5] = 4ip_4^\lambda p_2^\sigma \epsilon_{\lambda\mu\sigma\nu}$$

$$= 8[p_4^\mu p_2^\nu - g^{\mu\nu}(p_4 \cdot p_2) + p_2^\mu p_4^\nu - ip_4^\lambda p_2^\sigma \epsilon^{\lambda\mu\sigma\nu}]$$

Equation D.6 becomes

$$
\begin{aligned}
<|M|^2> &= 8G_F^2 V_{ud}^2 |\psi_{\pi\mu}(0)|^2 [2(p' \cdot p_4)(p' \cdot p_2) - p'^2(p_4 \cdot p_2)] \\
&= 8G_F^2 V_{ud}^2 |\psi^{\pi\mu}(0)|^2 [2m_{\mu^-}|p|(m_{\pi^+} + E_{\pi^0})(m_{\pi^+} + E_{\pi^0} + |p|) \\
&\quad - \{(m_{\pi^+} + E_{\pi^0})^2 - |p|^2\}m_{\mu^-}|p|] \\
&= 8G_F^2 V_{ud}^2 |\psi_{\pi\mu}(0)|^2 m_{\mu^-}|p|(m_{\pi^+} + E_{\pi^0} + |p|)^2
\end{aligned}
$$

(D.11)

where $E_{\pi^0} = \sqrt{|p|^2 + m_{\pi^0}^2}$.

BIBLIOGRAPHY

BIBLIOGRAPHY

Adler, S., et al. (2008), Measurement of the $K^+ \to \pi^+ \nu\bar{\nu}$ branching ratio, *Phys. Rev. D*, *77*, 052,003, doi:10.1103/PhysRevD.77.052003.

Agostinelli, S., et al. (2003), Geant4a simulation toolkit, *Nuclear Instruments and Methods in Physics Research Section A: Accelerators, Spectrometers, Detectors and Associated Equipment*, *506*(3), 250 – 303, doi:http://dx.doi.org/10.1016/S0168-9002(03)01368-8.

Ahn, J. K., et al. (2010), Experimental study of the decay $K_L^0 \to \pi^0 \nu\bar{\nu}$, *Phys. Rev. D*, *81*, 072,004, doi:10.1103/PhysRevD.81.072004.

Brod, J., M. Gorbahn, and E. Stamou (2011), Two-Loop Electroweak Corrections for the $K \to \pi\nu\bar{\nu}$ Decays, *Phys.Rev.*, *D83*, 034,030, doi:10.1103/PhysRevD.83.034030.

Brun, R., F. Bruyant, M. Maire, A. McPherson, and P. Zanarini (1987), GEANT3.

Buras, A. J. (2013), Towards the Identification of New Physics through Correlations between Flavour Observables.

Buras, A. J., A. Romanino, and L. Silvestrini (1998), K pi neutrino anti-neutrino: A Model independent analysis and supersymmetry, *Nucl.Phys.*, *B520*, 3–30, doi: 10.1016/S0550-3213(98)00169-2.

Buras, A. J., F. Schwab, and S. Uhlig (2008), Waiting for precise measurements of $K^+ \to \pi^+ \nu\bar{\nu}$ and $K_L \to \pi^0 \nu\bar{\nu}$, *Rev.Mod.Phys.*, *80*, 965–1007, doi: 10.1103/RevModPhys.80.965.

Bhlen, T., et al. (2014), The fluka code: Developments and challenges for high energy and medical applications, *Nuclear Data Sheets*.

Carruth, C. (2013), *Monte Carlo study of Level II Trigger Cut for the K0TO Experiment.* Bachelor's thesis, Department of physics, University of Michigan, MI.

Christenson, J., J. Cronin, V. Fitch, and R. Turlay (1964), Evidence for the 2 pi Decay of the k(2)0 Meson, *Phys.Rev.Lett.*, *13*, 138–140, doi:10.1103/PhysRevLett.13.138.

Ferrari, A., P. Sala, and A. J. R. Fasso (2005), Fluka: a multi-particle transport code.

Grossman, Y., and Y. Nir (1997), $K_L \to \pi^0$ neutrino anti-neutrino beyond the standard model, *Phys.Lett.*, *B398*, 163–168, doi:10.1016/S0370-2693(97)00210-4.

Isidori, G., and P. Paradisi (2006), Higgs-mediated K → pi nu anti-nu in the MSSM at large tan(beta), *Phys.Rev.*, *D73*, 055,017, doi:10.1103/PhysRevD.73.055017.

Iwai, E. (2012), Csi calorimeter for the j-parc koto experiment, Ph.D. thesis.

Koji, S. (2012), Measurement of k_l flux at the j-parc neutral-kaon beam line for the k_l→pinunu experiment, Ph.D. thesis.

Maeda, Y. (2014), Neutron-INsensitive Gamma-Ray Detector with Aerogel for Rare Neutral-Kaon Decay Experiment, *PoS*.

Marciano, W., and Z. Parsa (1996), Rare kaon decays with 'missing energy', *Phys.Rev.*, *D53*, 1–5, doi:10.1103/PhysRevD.53.R1.

Masuda, T. (2013), KOTO Detector Status, *PoS*, *KAON13*, 033.

Murayama, H. (2000), Supersymmetry phenomenology, pp. 296–335.

Naito, D. (2014), Evaluation of the inefficiency of a charged particle detector for the koto experiment.

Sato, K. (2007), Csi calorimeter cluster shape background , Masters thesis, Osaka University.

Shiomi, K., K. Baek, J. Comfort, E. Iwai, N. Kawasaki, et al. (2012), Measurement of K(0)L flux at the J-PARC neutral-kaon beam line, *Nucl.Instrum.Meth.*, *A664*, 264–271, doi:10.1016/j.nima.2011.11.010.

Sumida, T. (2008), Search for the decay $K_L^0 \to \pi^0 \nu \bar{\nu}$, Ph.D. thesis.

Takahiko, M. (2014), Development and experimental study of the koto detector system using three kl neutral decay modes, Ph.D. thesis.

Wolfenstein, L. (1983), Parametrization of the Kobayashi-Maskawa Matrix, *Phys.Rev.Lett.*, *51*, 1945, doi:10.1103/PhysRevLett.51.1945.